SCUOLA DOTTORALE IN FISICA

XXII CICLO

A simplified 1D model for the chemo-mechanical coupling in sarcomere dynamics

Lena Rebecca Zastrow

A.A. 2010/2011

Tutor: Prof. Antonio Di Carlo

Coordinatore: Prof. Guido Altarelli

Introduction

Muscle tissue is a biological actuator whose performance is controlled by a biochemical activation. This tissue is able to generate force when stimulated either electrically (intact muscle cells and larger sample) or by tuning the concentration of calcium ions in the surrounding fluid (skinned cells and smaller samples). The underlying regulatory mechanisms are still poorly understood. The coupling between chemical activation and mechanical contraction is an open problem of great interest to cardiologists and the biomedical profession in general, since muscle diseases like cardiac arrhythmias and muscular dystrophy involve dysfunctions of the regulatory mechanisms.

In the last twenty years, experimental techniques have been developed to test biological tissues on very fine length scales, down to nanometers and beyond. Micromanipulation experiments are done with optical tweezers or microneedles on huge protein complexes, measuring nanometer displacement and piconewton forces. These experiments provide a powerful tool to study the response of active tissue at this length scale. Theoretical models are required to help understanding the experimental data so obtained. On the nanometer scale, muscle contraction is generated by molecular motors, namely, myosin II interacting with F–actin. Collective systems of motors form the basic units of muscle cells at the micrometer scale, the sarcomeres. An useful research tool to bridge the gap between the nano– and the micro–scale would be a virtual laboratory making it possible to simulate the effects produced at the sarcomere scale by different hypothetical mechanisms assumed at the single–motor scale. For example, different assumptions on the activation–contraction coupling could be easily put to test.

Simplified models are of major interest in this endeavour. Such models, not accounting for the molecular details of the contraction mechanism, may be char-

acterized by a relatively small number of parameters, that can be calibrated by comparing the model dynamics with available experimental results. Moreover, the use of simplified models makes it possible to compute the long–time evolution of large collective systems, thus bridging the gap between the single molecular motor and the sarcomere.

In this thesis I put forth a simplified 1D two–state model of a single molecular motor, which I then scale up to a collective system representing a half–sarcomere. My focus is mostly on skeletal muscle, since this tissue is hierarchically organized in a very orderly way from the nanoscale to the microscale and beyond. My model is a Brownian ratchet model, inspired by that proposed by Jülicher et al [1], who employed it successfully to describe some properties of processive motors active in the cytoskeleton. The model is extended to allow for partial activation levels and time–varying stimuli. To this end a switch–like approach is adopted. The extended model is implemented in C–language.

The basic physiology of skeletal muscle, including an account of the present–day knowledge on the underlying regulatory mechanisms, is introduced in Chapter 1, together with an outlook on current experimental techniques and relevant experiments results. In Chapter 2, the 1D two–state model is introduced, a stochastic Langevin equation of motion is given for each state, and the chemical transitions between the two states are modelled and discussed. In Chapter 3, two important experiments of micromanipulation via optical tweezers are reported: one involving a single myosin motor on a single actin filament, the other involving an array of filaments. The experimental setups are mimicked by tuning parameter values and boundary conditions. Numerical results are finally compared with published experimental data. Chapter 4 extends the model to allow for a tunable and time–varying muscle contraction. Partial activation protocols are tested on a single filament and on a (decimated) half–sarcomere. Finally, the response of the half–sarcomere to a single twitch is simulated.

Acknowledgement

Contents

Chapter 1

The skeletal muscle tissue

Studies on muscle tissue have a long history. Experiments on single muscle fascicles have been realized since 1850 and even before [2–6]. Advances in muscle research are strongly connected to the development of experimental techniques. Today, sophisticated experimental techniques are available to allow for manipulating single proteins of the tissue [7–9].

The aim of this work is to develop a simplified model for the dynamics of the striated skeletal muscle from the nano to the microscale. In this chapter the physiology of the skeletal muscle tissue is introduced and the basic concepts of the contraction dynamics are discussed. In the first section, I review the structure of muscle tissue from the whole muscle down to the nanoscale. In the second section I present the studies done on whole muscles at the beginning of the 20th century by Hill and Fenn; they introduced the idea that muscle tissue operates as a machine that consumes energy to produce work. In the third section, I examine the mechanism of contraction from the micron scale down to the level of single proteins (10 nm) forming the muscle tissue. The fifth section is a brief account of experimental techniques used to study biological systems at very small length scales (1-100 nm).
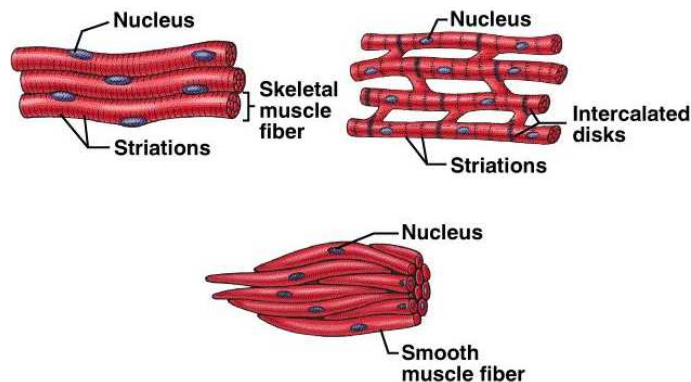
Figure 1.1: Three different kinds of muscles are found in vertebrate animals: smooth, cardiac and skeletal muscle.

1.1 The structure of skeletal muscles

Muscles are hierarchically structured, extremely sophisticated biochemical actuators [10, 11]. Three different kinds of muscles are found in vertebrate animals: smooth, cardiac and skeletal muscle. Smooth muscles are situated in organs, arteries and veins, while the striated cardiac muscle drives the heart beat; these muscles are governed by the autonomic nervous system. Skeletal muscles are responsible for the body motion and are governed by the somatic nervous system.

Skeletal and cardiac muscle are called striated muscle; this name is due to their striated appearance on the cell scale that is observed with microscopy. These striations are generated by the organized arrangement of protein filaments inside the muscle cell. A schematic representation of the structure of skeletal muscle is shown in Fig. 1.2.

The **skeletal muscle fascicle** is a bundle of cells held together by connective tissue, through which blood vessels and nerves. run These cells are called *muscle fibers* or *myofibers*. They mostly extend all the way, from one tendon to the opposite. In the human skeletal muscle the myofibers reach lengths up to tens of centimeters. They have a cylindrical shape with a diameter of $\sim 50\mu$m. A muscle may comprise thousands of cylindrical myofibers.

The **myofiber** is a multi–nucleated cell. Its plasma membrane is called the sarcolemma, while the cytoplasm is known as the sarcoplasm. A large number (~ 1000) of *myofibrils* are situated within the sarcolemma. Myofibrils extend to
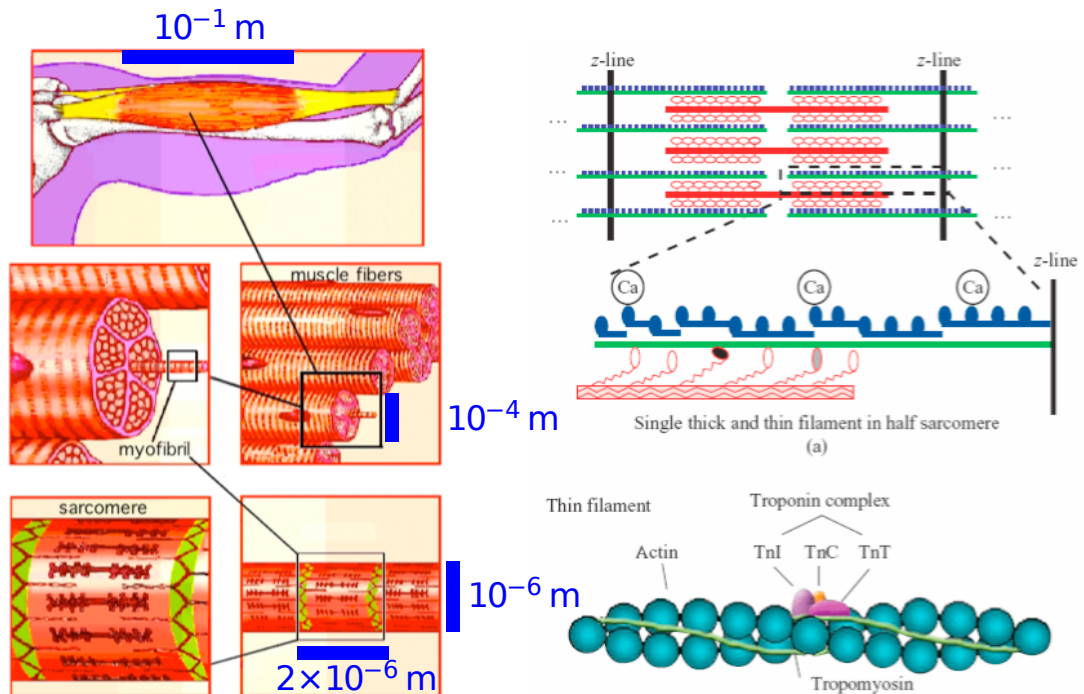
Figure 1.2: Schematic representation of a human biceps at various length scales.

the same length of the myofiber, while being only about 1 micron in diameter. The nuclei are flattened and pressed against the inside of the sarcolemma. Other organelles like the *mitochondria* that are responsible for the aerobic respiration, are surrounded by the myofibrils(see Fig. 1.3).

Each **myofibril** is a chain of *sarcomeres*, the basic functional unit of muscle cells. The sarcomere has the same diameter of the myofibril ($\sim 1\mu$m) and extends over 2-4 μm. It is delimited by the *Z–disks* at its two ends. The sarcomere has a symmetric structure and its middle–line is called *M–line*. A myofibril from a human biceps may contain 100,000 sarcomeres.

Inside the sarcomere protein filaments are arranged in arrays. These filaments are collectively called *myofilaments*: *thick* and *thin filaments* and *titin*.

The **thin filaments** have a diameter of about 5 nm. They are composed chiefly
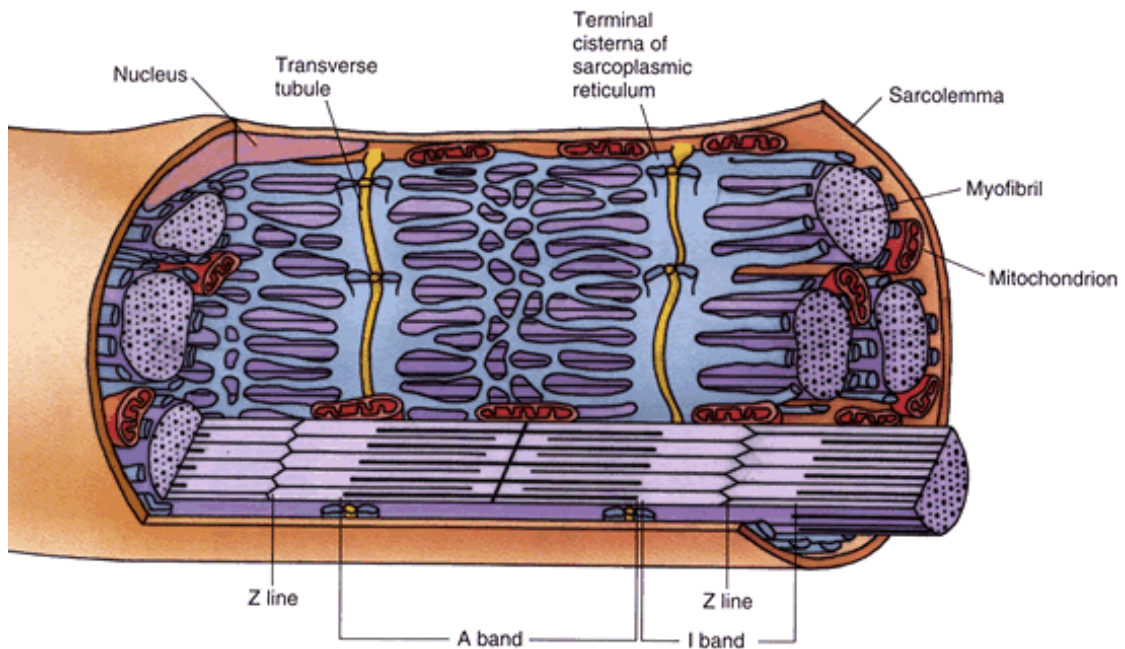
Figure 1.3: A section of a multinucleated muscle cell.

of the protein *actin* along with smaller amounts of two other proteins, *troponin* and *tropomyosin*. The actin filament (*F–actin*) is formed by polymerized G–actin units; it has a double helix conformation. The troponin is attached periodically on the actin filament. The tropomyosin, a protein of the length of one F–actin period, lies on the F–actin and is attached to the troponin (see Fig. 1.4). Troponin and tropomyosin are responsible for the regulation of activation (see Section 1.5). Two arrays of thin filaments are found in the sarcomere, one on each side of the M–line. The array of thin filaments is linked at one outer end to the corresponding Z–disk.

The thick filaments have a diameter of about 15 nm, and are composed of *myosin II* protein (see Fig. 1.4). They are situated centrally in the sarcomere; at their center the filaments are connected together and form the M–line. Each thick filament is linked to the Z–disks by titin. Titin is one of the longest proteins known. Under normal conditions of contraction (sarcomere length up to 3.6 μm) it is slack and it tightens when the sarcomere length reaches its maximum extension. It is largely suggested that the main function of titin is to restrain the sarcomere from breaking off when overstretched.
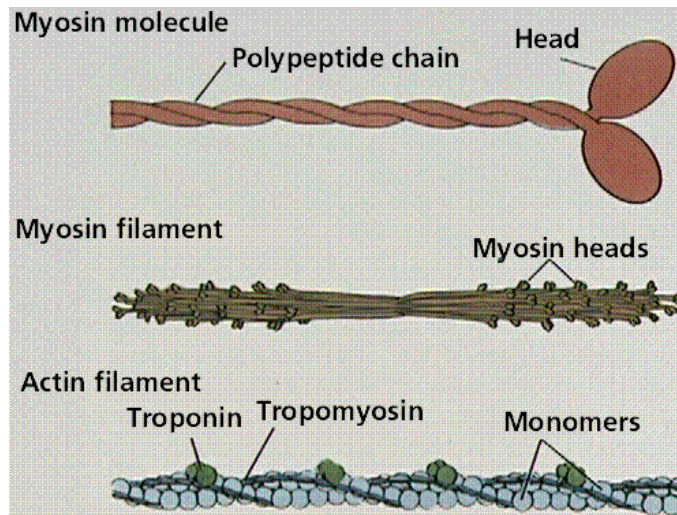
Figure 1.4: Scheme of the thin and thick filaments.

The myosin II protein has three different domains: the heavy mero–myosin chain (HMM) also called *myosin head*, the light chain or *neck domain* and the tail (see Fig. 1.5). A myosin II motor unit is composed of two myosin proteins whose tails are interwind to form a single tail. The filament is obtained by many motor units whose tails twist to form a backbone; the myosin heads protrude from this backbone (see Fig. 1.4).

This arrangement of thin and thick filaments in the inner sarcomere is responsible for the striation of the muscle tissue observed with microscopy. In fact the dark band is due to the dense array of thick filaments, while the adjacent pale band corresponds to the array of thin filaments on each side of the Z–disk (see Fig. 1.2).

1.2 The muscle as an active tissue

The modern idea of how muscles operate was introduced in physiology by Helmholtz in 1848 [12]. He suggested that muscle dynamics is driven by the metabolism, i.e. chemical energy is consumed to perform mechanical work in much the same way as manmade machines do. Helmholtz's purpose was to demonstrate the general validity of the law of conservation of energy. To prove his thesis, he performed
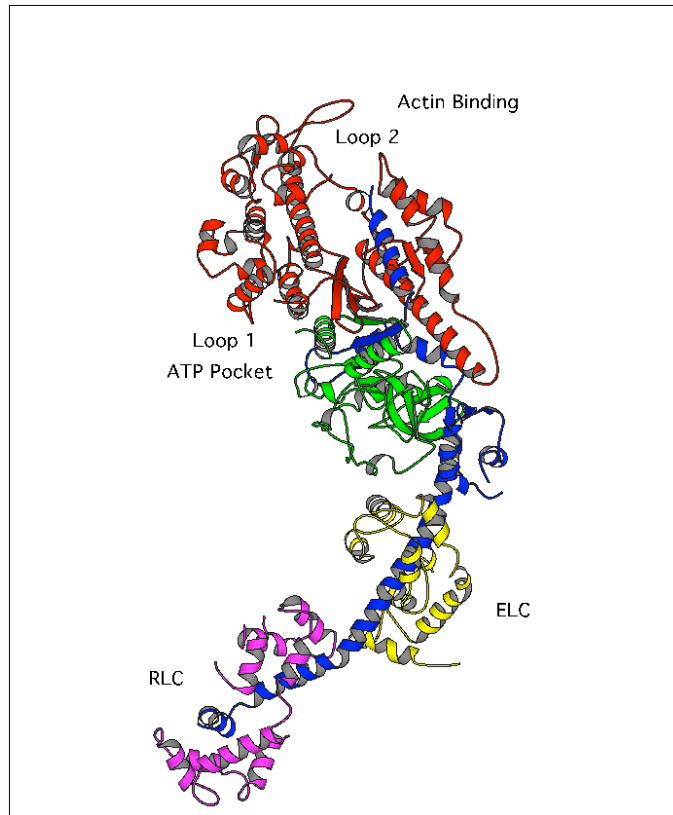
Figure 1.5: Schematic representation of the myosin II motor.

experiments on muscles of dead animals measuring the heat production during electrically stimulated contraction.

Helmholtz was followed by Heidenhain and Fick [2, 3], who made experiments on isolated frog muscles, mostly the sartorius, to investigate the heat–work relationship in muscle contraction. Nevertheless, a satisfactory experimental basis of their hypothesis was furnished only by Hill and Fenn in the early 20th century [4,5].

These experiments were done on constantly activated muscle fascicle, i.e. under *tetanus* conditions. To obtain a tetanus, the muscle tissue was stimulated by an periodic electric signal. When stimulated, the muscle contracts and relaxes after a characteristic time. If the stimulation is repeated periodically the tension developed by the muscle is given by the sum of single responses. When the muscle is stimulated with an electric signal of frequency higher than a threshold (~ 50 s^{-1}), the muscle reaches constant activation (see Fig. 1.6).
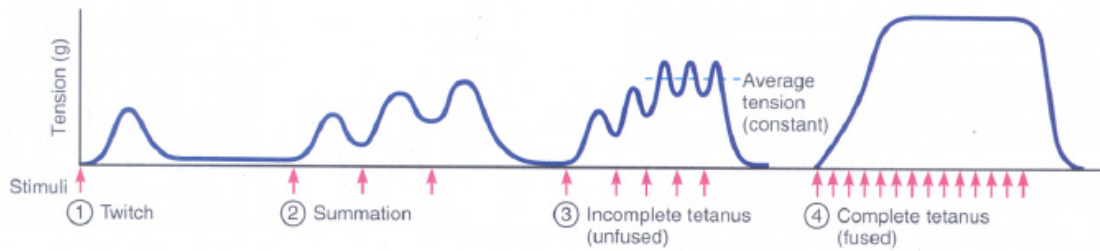
Figure 1.6: Tension developed by muscle in response to electrical stimulation as a function of time. The different shapes correspond to stimulation with different frequencies. From left to right: at low frequency single twitches are measured; for increasing frequency a summation of tension is observed; even higher frequency produces an unfused tetanus, i.e. the muscle oscillates with constant mean value; finally, for frequencies beyond the threshold, the muscle reaches constant activation (fused tetanus).

Fenn realized a series of experiments to study the dynamics of isolated sartorius frog muscle. He found that the shortening heat, produced by the muscle during contraction, is roughly proportional to the work done, i.e. to the product of the length of shortening and the weight lifted. These observations were in contrast with the idea of muscle dynamics based on viscoelastic mechanisms, widely accepted at that time: the muscle was thought of as a pre–charged viscoelastic tissue. Fenn realized his experiments with the aim to disprove this current idea.

Today accurate experiments can be realized to measure the shortening heat and the relation between shortening heat and work was observed to depend on the particular type of muscle under exam (see [13] for a review).

1.2.1 Hill's force–velocity relationship

Hill developed an experimental technique providing for a better time resolution in heat measures during muscle dynamics in tetanus conditions [4]. This technique allowed him to realize a systematic study of the temperature as a function of time during the contraction at constant activation and under isotonic conditions, i.e. with constant load attached to the muscle fascicle. Usually frog sartorius was used in these experiments. He did the following observations:

1. The muscle temperature does not depend on the work done.

2. The temperature depend linearly on the amount of shortening.

3. The velocity of shortening and therefore the rate of heat absorbed depends on the weight muscle lifted by the muscle.

Hill deduced his famous force–velocity relationship from these results.

$$(P + a) \cdot (v + b) = (P_0 + a) \cdot b = \text{const}, \tag{1.1}$$

where P is the weight, v the velocity of shortening, P_0 is the maximum load (i.e. a tetanus loaded with P_0 will nor contract neither elongate), a is the rate of heat produced during shortening a/P_0 is a constant, b is a constant with the dimensions of velocity. Although the force–velocity relationship was deduced by observations involving heat measures, the relationship itself does not depend on temperature and can be verified independently.
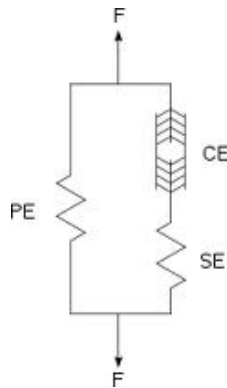
Figure 1.7: Schematics of the three–element model proposed by Hill.

Hill also proposed a model that represents an active muscle as composed of three elements. Two elements are arranged in series: a contractile element (CE) which at rest is freely extensible, but when activated is capable of shortening; and an elastic element (SE). To account for the elasticity of muscle at rest an elastic element (PE) was arranged in parallel to these serial structure (see Fig. 1.7) [14]. For the activated muscle the contractile element obeys the characteristic equation 1.1. The three–element model inspired various approaches on continuum muscle models [15, 16].

17

1.3 The mechanism of contraction

1.3.1 The sliding filament model
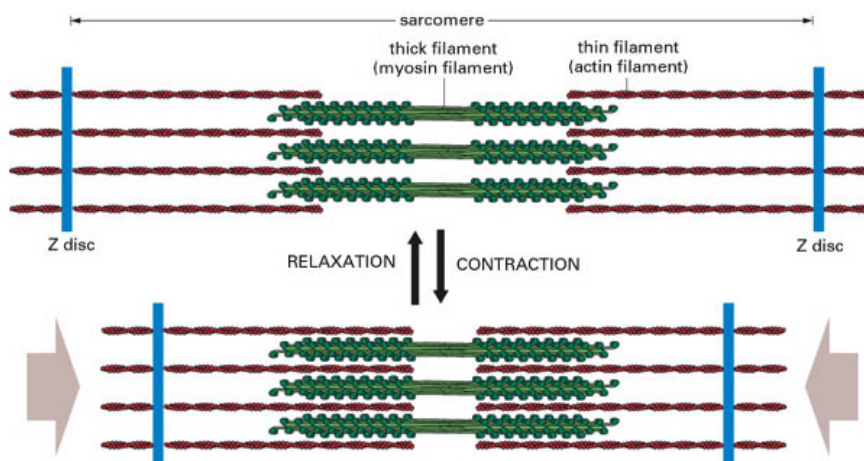
Figure 1.8: In the sliding filament model muscle contraction is generated at the sarcomere scale by the sliding of the thin filament with respect to the thick one toward the M–line.

An important interpretation of the microscope images of muscle tissue was given simultaneously and independently by Hanson and H.E. Huxley [17] and A.F. Huxley and Niedergerke [18]. In these two papers, published back–to–back in Nature, the observation of constant filament length during muscle contraction was discussed. Both groups presented the hypothesis of sliding filaments. In the sliding filament model, it is assumed that the shortening of muscle at the sarcomere scale is generated by the sliding of the thin filaments with respect to the thick ones (see Fig. 1.8); the intrinsic length of each filament will not change during contraction.

In particular, A.F. Huxley and Niedergerke supposed point–wise interactions between the two contractile filaments. They proved that the isometric tetanus tension decreases with lengthening of the sarcomere and argued that the tension is produced proportionally to the overlap of the two filaments, actin and myosin.

In later works the relationship between sarcomere length and tension development was investigated [19–21] and the sarcomere–length relationship was established (see Fig. 1.9). This relationship can be well explained on the base of the
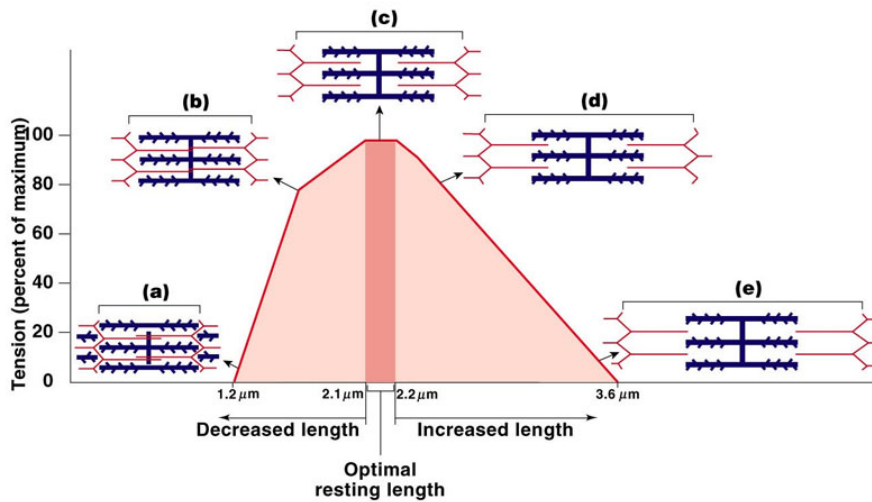
Figure 1.9: The sarcomere–length force relationship. The slope variates with qualitative different arrangements of the filament couple of thick and thin filament inside the sarcomere.

sliding filament along with the point–wise interactions between the thick and the thin filament.

The sarcomere–length force relationship is piecewise affine, exhibiting four different linear regimes that can be related to different overlap arrangements.

1.3.2 The Huxley cross–bridge model

A.F. Huxley published a very detailed review of experimental observations [6]. On this background, Huxley exposed a mathematical model to describe the sliding filament dynamics generated by point–wise interactions. In the original model, these interactions are described by two different states, each state involving forces generated by a harmonic potential, the dynamics being characterized by the transitions between these two states.

Huxley compared the results obtained from his model with those measured by Hill, i.e. force–velocity relationship and heat measurements produced as function of the contraction, finding an excellent agreement. The point–wise interactions between the two filaments were called cross–bridges and the model took the name of the cross–bridge model.

Schematic representation of the cross–bridge model
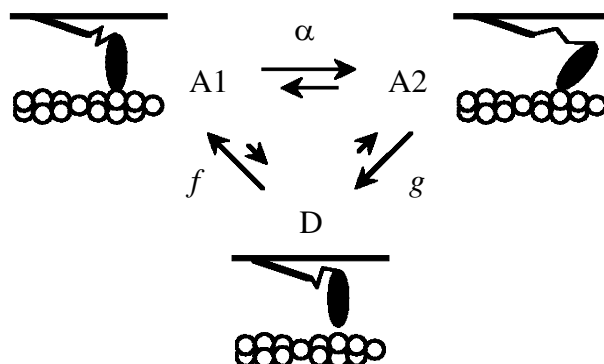
Figure 1.10: The state A1 and A2 represent respectively the pre– and afterstroka, while D indicates the state of weak interaction. the transition rates between the three states are called f (D → A1), α(A1 → A2) and g (A2 → D). The interaction occurs cyclically.

The model was then extended to a three state model, today known as Huxley's cross-bridge model [22]; the three states are the prestroke, aftersroke and the sate of weak interaction (see Fig. 1.10). This mathematical model inspired the the swinging lever arm model, a detailed model of the myosin dynamics at the nano–scale.

1.3.3 The swinging lever arm model

In the swinging lever arm model, the force transmitted through cross–bridge interactions is assumed to be generated by a conformational change of the light chain in the myosin protein (neck domain). The head domain is thought to exert a force on actin by the rotation of the myosin head, the neck domain having the role of lever arm (see Fig. 1.11). The chemical energy used by the myosin head to generate this force is obtained hydrolyzing AdenosineTriPhosphate (ATP) into AdenosineDiPhosphate (ADP) and Phosphor (P). The hydrolysis reaction occurs cyclically and the motor domain plays an enzymatic role in this reaction. The enzymatic reaction occurs when ATP adheres to the head domain of the myosin II protein.
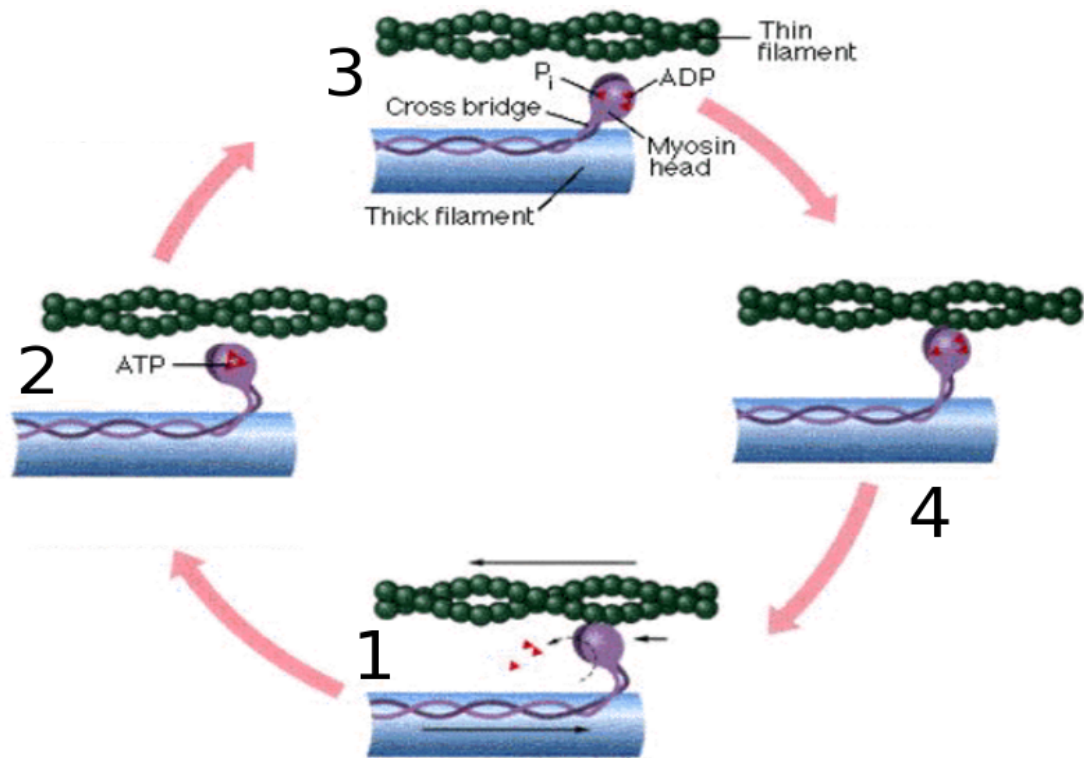
Figure 1.11: Step 1: myosin attached to actin in its ground state. Step 2: ATP adheres to myosin, there is no more interaction between actin and myosin. Step 3: hydrolysis of ATP occurs, myosin absorbs the released chemical energy and acquires its excited, extended configuration. Step 4: myosin in its excited state reattaches to actin. Back to step 1: the excited state decays with the release of ADP and P from the head domain; myosin turns into the *rigor* state. During this conformational change it exerts a force on actin, causing filament to slide.

A simplified model of the ATP cycle is shown in Fig. 1.11. The cycle starts with an initial state 1 in which the ATP binding site on the myosin head is empty and myosin is strongly bound to actin. In muscle this state correspond to *rigor mortis*. When muscles are depleted of ATP, just after death, they become stiff and rigid, because without ATP, myosin heads stay firmly attached to thin filaments.

The ATP adheres to the myosin in the *rigor* configuration and myosin detaches from the actin filament. In this state there is no more interaction between actin and myosin. The head domain operates as an enzyme in the hydrolysis reaction ($ATD \rightarrow ADP + P$) and it absorbs the energy released during the hydrolysis.

Consequently, in step 3 of Fig. 1.11, the myosin head is in an excited state. In this state the neck domain forms a large angle with the filament, it is in an extended configuration. Myosin is now able to interact with actin. The next step occurs when myosin is bound to actin. Myosin is still in its excited state with extended configuration. The excited state decays when ADP and P are released from the head domain, myosin turns in its ground state at the low–angle configuration. During this conformational change myosin exerts a force on actin generating the sliding of the actin towards the center of the sarcomere (see Fig. 1.8).

The swinging lever arm model is a powerful tool to explain the contractile behavior of muscle tissue, since it predicts correctly numerous experimental observations. However, there are experimental observation which cannot be explained within this framework [23, 24].

1.4   Experimental techniques on the nanoscale

Experiments are of great importance in muscle research and with the development of experimental techniques we get more and more details about the contraction mechanism.

In biology, experiments are classified as *in vivo*, *in situ* or *in vitro*. An *in vivo* experiment is realized on a part of a living organism without extracting it from the organism nor using invasive measurement techniques. *In situ* experiments are realized on systems which are situated in their natural environment, but, different to the *in vivo* experiments, *in situ* experiments are realized using invasive techniques, for example by mechanically manipulate the system under exam. Almost physiological conditions are guaranteed in this experiments. Finally, in *in vitro* experiments the system under exam is extracted from its physiological context and studied in an artificial environment controlled by the experimentalist.

The experiments on muscle mentioned in the previous sections of this chapter were all *in vitro* experiments. In this section, we introduce experimental techniques developed in the last 25 years to study biological systems at the nanoscale. Single molecule experiments are based on two key technologies: single molecule imaging and single molecule nano–manipulation. The difficulties in realizing experiments on systems at very small length scales are due also to the need of extracting minute

components of the muscle tissue without damaging them. Chemistry did a lot of progress on this issue, but it is beyond our scope to discuss that.

1.4.1 Single–molecule imaging

The imaging on very small length scale can be done by electron microscopy and X-ray diffractions. Both techniques are usually applied to solid materials. They are used to study crystallized single bio-molecules and small collective systems [25–27]. These techniques damage considerably the material under exam. In an interesting experiment the contraction dynamics of frog sartorius muscles tissue was visualized using X-ray diffraction [28, 29]. The authors were able to measure the fraction of attached cross-bridges in a small ensemble of myofibrils

Another technique to observe kinetic behavior at the nano scale is realized using fluorescence. FRET stands for *Förster resonance energy transfer* or *fluorescence resonance energy transfer*. This technique is used to measure the kinetics of single macromolecules of the nanometer size, such as large protein complexes. It takes advantage from the property of fluorescent molecules that absorb radiation of a given frequency ν and reemits radiation with frequency $\nu' < \nu$. The technique involves two fluorescent molecules, a donor and an acceptor which were fixed on characteristic sites of the macromolecule under exam. The preparation of the protein is a challenge of molecular engineering.

The two fluorescent molecules, donor and acceptor, are chosen in such a way that the emission frequency ν'_D of the donor overlaps with the absorption frequency ν_A of the acceptor. When emitting, the donor stimulates a nearby acceptor.

FRET is used to study configurational changes of the biomolecule by measuring the changes of the distance between donor and acceptor; it does not provide precise measurements of the distance between the marked zones on the macromolecule. The technique allows to measure spontaneous kinetics without the application of any force.

1.4.2 Micro–manipulation techniques

The single–molecule systems can be studied also using manipulation techniques. The dynamic response of biopolymers to external forces may shed light on intrin-

sic properties of the polymers itself. There are various techniques to manipulate biopolymers; mainly optical tweezers and the manipulation via microneedles is used to examine the piconewton forces exerted by molecular motors. A detailed description of two experiments realized with the optical tweezer is given in Chapter 3, where the experimental results are compared to computation; in Section 3.1 is described a single motor assay, while in Section 3.4is studied the response due to the interactions of a filament pair (actin and myosin).

By manipulating isolated bio-systems, the dynamics of single motors can be examined [7, 8, 30]. Advances in molecular engineering allowed to realize an experiment on myosin proteins with a modified length of their neck domain [31]. The response in displacement and force were measured for molecules with different neck size; the aim of the experiment was to proof the lever arm hypothesis in detail.

Filament systems constitute the level between single motors and sarcomeres. A pioneering experimental setup to test collective behavior was realized fixing a large number of myosin heads onto a glass plate and making an actin filament slide on them [9, 32, 33]. The actin filament is examined in different conditions, e.g. it drags a weight, or it is trapped by an optical tweezer. The kinetics of the filament can be measured and in the second case it can be measured the force that the filament exerts on the trap.

1.5 The mechanism of calcium control

The mechanism of regulation is of particular interest in studies of the cardiac muscle, as malfunction of the regulation in the heart muscle leads to death. Most physiological studies aiming at understanding the regulatory mechanisms are done on the cardiac muscle tissue. However, on the sarcomere level, cardiac and skeletal muscles are quite similar. As a consequence, I may give a description of the elementary molecular mechanism of Ca^{2+}-regulation based on studies of both types of sarcomeres. Some known important differences between the two kinds of tissues are briefly discussed in Section 1.6.3.

Let us first introduce the main features of the regulatory structure on the thin filament [26, 34, 35]. The principal proteins involved in the regulation process are actin filament, troponin and tropomyosin (see Fig. 1.12). Actin monomers
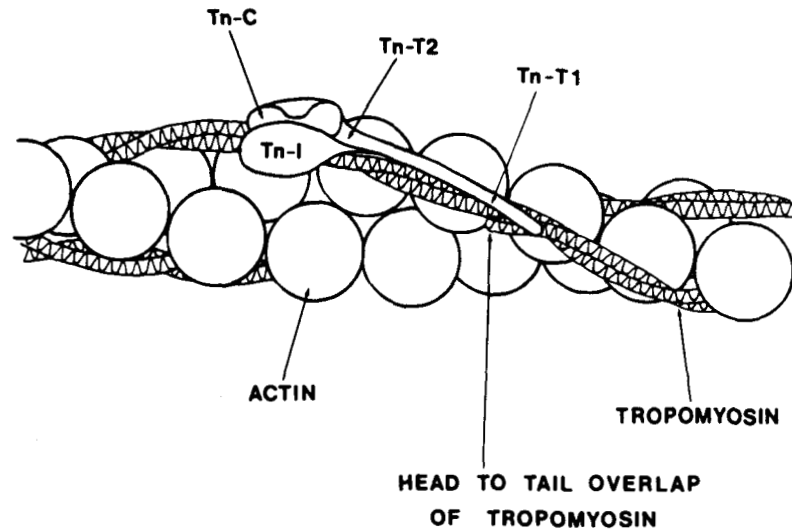
Figure 1.12: Schematic representation of the thin filament regulatory unit. The troponin complex is composed of three subunits: troponin C, troponin I and troponin. The tropomyosin is made of monomers; two alpha-helix tropomyosin monomers dimerize to form a coiled structure that overlaps partially with the neighboring tropomyosin dimers to form a continuous tropomyosin strand. This strand lies in the two grooves of the F-actin double helix. Each tropomyosin dimer is bound on a troponin complex; the tail region of the troponin complex extends to the tropomyosin molecule at its overlap region with the neighboring dimer. Reproduced from [34]

(globular actin) are polymerized into a double helical structure to form filamentous actin, the F-actin (see section 1.1). F-actin together with two tropomyosin strands, each binding a troponin complex, forms the thin filament. Tropomyosin and the troponin complex regulate the affinity of F-actin towards the myosin domains, i.e. they allow or inhibit the interaction between actin and myosin.One tropomyosin covers seven actin molecules, i.e. half the period of the actin helix. This entity is the regulatory unit of the thin filament.

Calcium ions adhere to the troponin complex and induce a structural change in troponin itself, which causes a relocation of the tropomyosin along the entire regulatory unit. Tropomyosin moves from its inhibitory position in the groove to a more peripheral position on the F-actin. In this way, the actin docking sites

are exposed to allow for interaction with the myosin domains [26]. There are very few single–motor assays performed on thin filament complete with their regulatory structure [36]. For this kind of experiment to be possible, the regulatory thin filament has to be reconstructed after the extraction of single proteins from the muscle tissue; this involves sophisticated chemical processes, difficult to realize.

1.5.1 The nervous stimulation in skeletal muscles

It is beyond the scope of this work to discuss extensively the whole mechanism of regulation from the muscle–fascicle scale down to a molecular motor. Nevertheless it is useful to have a general idea of muscle activation.

The skeletal muscle is stimulated by the somatic motor neurons. A neuron is composed the soma with the nucleus, dendrites and axons. The dendrites receive the nervous stimulus from other neurons forming a network while the axon connects the soma and the muscle cells. The extremes of the axon adhere to the muscle cell forming the synapse. The ensemble of cells (myofibers) activated by the same neuron forms what is called a motor unit. In the skeletal muscle, one motor unit confines to the next. At this border zone, the muscle cells of one motor unit are interspersed with cells from the confining motor unit. In this way, motor units take advantage of the contact forces to synchronize with neighboring units (see Fig.1.13).

The transport of the stimulus from the cell membrane to the interior of the cell is facilitated by the so-called T-tubules (see Fig.1.14). T-tubules form a dense network in the muscle cell: each sarcomere is surrounded by two T-tubules. The interior of the tubules is connected to the extracellular matrix; in other words, it is an extracellular space lined with a membrane. The activation potential generated by nervous stimulation is propagated across the surface membrane and down the T-tubules; this occurs mainly through currents of K^+ and Na^+ ions. Consequently, the voltage-mediated signal is transmitted to ryanodine receptors and induces the opening of calcium ion channels. These channels permit calcium to be released from the sarcoplasmic reticulum into the cytoplasm. Calcium ions are stored in the sarcolemma and when activation ends, they are pumped back there after a characteristic time.
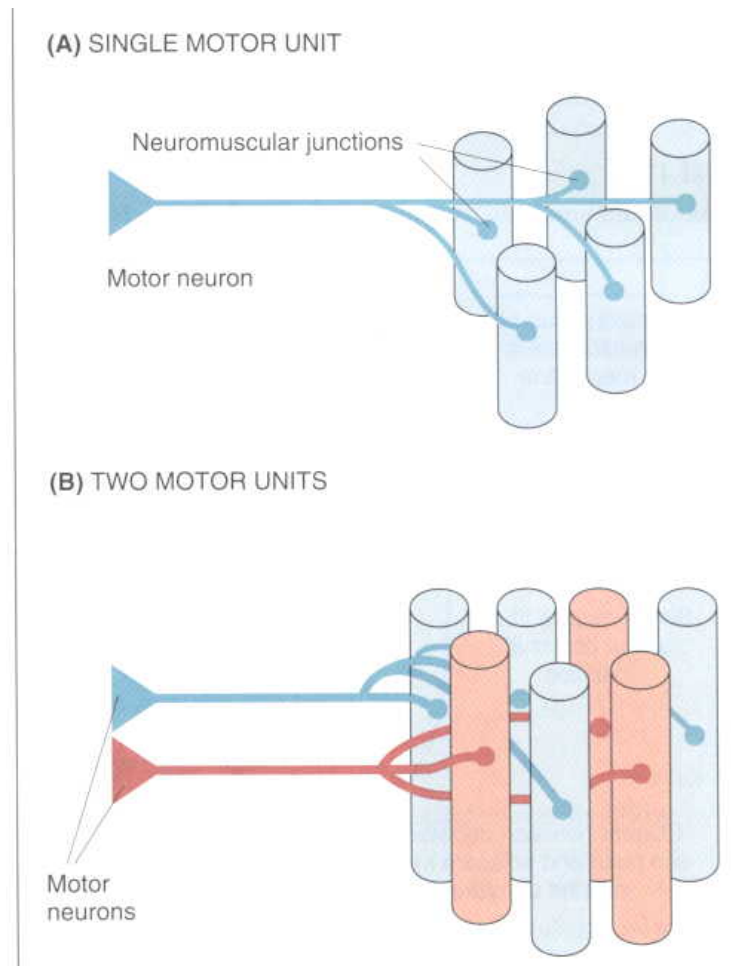
Figure 1.13: Top: schematic representation of a single motor unit; the muscle cells are represented by cylinders and the axons by the lines connecting the cells. Bottom: schematic representation of the interspersed structure of the cells of two adjacent motor units.
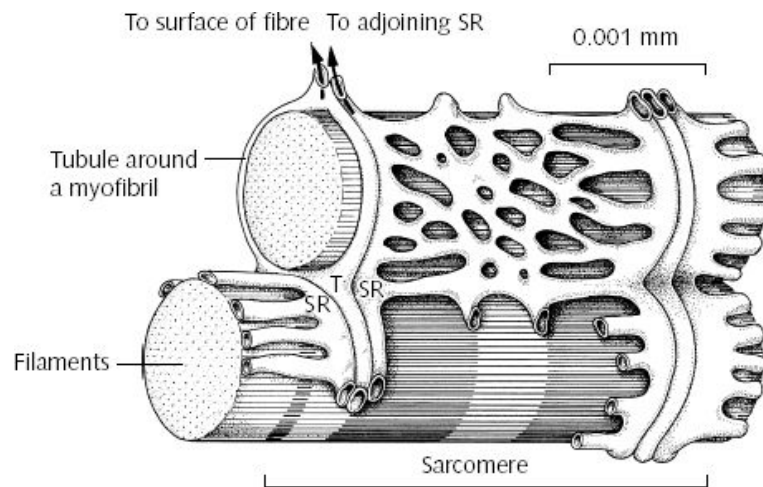
Figure 1.14: Schematic representation of a couple of myofibril segments along with the sarcolemma and the structure of T-tubules. The T-tubules form a narrow network of channels in the muscle cell; geometrically the inside of the channels are connected to the extracellular matrix. T-tubules are important of the propagation of the nervous stimulus inside the muscle cell.

This propagation of the nervous stimulation requires an intact sarcoplasmatic reticulum, with T-tubules included. Therefore, stimulus activation can only be realized experimentally with intact muscle cells, not fortheir smaller parts. And infact, myofibrils need to be activated in a solution with a suitable concentration of Ca^{2+}.

1.6 Recent experiments and open questions

This section focusses attention on experimental research in muscle activation. This is a very broad field of research and an exhaustive discussion is beyond the scope of this work. I concentrate on three issues: the tetanization process, the phenomenon of force depression and force enhancement and the problem of myofibril length dependent activation.

1.6.1   The tetanization process

Tetanization is the process by which is obtained an intact muscle cell or a muscle fascicle in a constant activated state (see Section 1.2, Fig. 1.6). The tissue is stimulated by electric twitches of fixed constant frequency. This technique is well known and largely tested, as it is used since the end of the 19th century [2–5, 12]. If the twitch frequency is larger than a threshold frequency the muscle approaches constant tension exponentially in time [37].

Studies on the early stages of the tetanization process, the response to single twitches and the dependence of the contraction on the frequency of twitches provide insights of the muscle response to electric stimulation [38–41].

Moss [40] compared the response of intact muscle fibers excited to tetanus by twitches with the behavior of skinned fibers activated in a solution with a given calcium concentration. In particular, he compared chemically and mechanically skinned fibers. He found that the dynamics of the three differently treated fibers are indistinguishable, i.e. the response of the tissue was not influenced by the preparation of the fiber and the two ways of stimulation are equivalent.

Smaller units, like myofibrils, can only be activated by calcium ions in solution. Under the assumption that the extraction of a myofibril from muscle tissue does not alter qualitatively its behavior, experiments on myofibrils can reasonably be considered to give insights to the mechanism of activation on the nanoscale.

1.6.2   Force depression — force enhancement

The interest in activation studies increased with the progressive understanding of the contraction mechanism. In fact, as we saw in Section 1.1, Hill's model and A.F. Huxley's model give a description of the contractile behavior under constant activation and stationary force. To describe the response of the muscle tissue to a time-varying stimulus a mechano-electric feedback relation is required. The idea of a feedback relation was mentioned by Julian [20]. To shed light on this coupling various sophisticated experimental setups were designed which examines the length-dependent activation [29, 42–46].

This paragraph discusses the force depression assays. It was observed by several groups that the steady-state isometric force following shortening of an activated

muscle is smaller than the corresponding steady-state force obtained for a purely isometric contraction at the corresponding length [47–49]. This phenomenon is referred to as force depression.
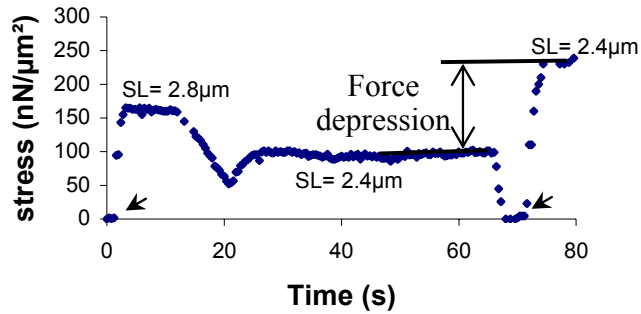
Figure 1.15: Myofibril response in tension during activation at an average sarcomere length (SL) of 2.8μm. The fibril is shortened to an average SL of 2.4μm. After more than 60s the fibril is deactivated and reactivated under constant SL (2.4μm). Reproduced from [50]

Joumaa and Herzog performed an experiment to test force depression in myofibrils of rabbit psoas muscle [50]. Isolated myofibrils from rabbit psoas muscle were fixed to a glass needle on a motor at one end and to a nanolever at the other end, allowing for length changes and force measurements, respectively. The myofibril is activated through the concentration of calcium ions in the flow cell. The activation is held constant and the length is modified, from 2.8μm to 2.4μm average sarcomere length (see Fig. 1.15). During this process of shortening the stress decreases. After tens of seconds in which the stress of the myofibril remain constant, the tissue is deactivated and then reactivated after a few seconds. The stress developed after the reactivation is bigger than the initially developed stress at 2.8μm average sarcomere length. The difference of the stresses at 2.4μm, i.e. the difference of the stress obtained respectively before and after the de- and reactivation, measures the amount of force depression (see Fig. 1.15).

In particular Herzog's group studied this phenomena at various length-scales; force depression was observed from the single myofibril up to the entire muscle fascicle [50, 51].

Analogously to force depression, also force enhancement was observed when the

muscle was stretched under constant activation [52]. It was suggested that the mechanisms on the molecular scale generating force enhancement is similar to that generating force depression. The origin of both phenomena is still unclear. One of the hypotheses proposed to explain force depression is sarcomere length non-uniformity. According to this hypothesis, during shortening on the descending limb of the force-length relationship, sarcomeres are assumed to shorten by different amounts because of instability. Some sarcomeres do nearly not shorten, whereas others shorten more than average; these sarcomeres may shorten to a degree that places them on the ascending limb of the force-length relationship. This behavior leads to a situation in which the tension produced is smaller than that produced at the corresponding length during an isometric contraction in which sarcomere lengths are assumed to be relatively uniform. Another hypothesis is set forth by Herzog's group. They suggest that force depression is due to history dependence of contraction, i.e. the behavior of the muscle tissue depends on its initial mechanical and electrical state [44, 53].

1.6.3 Length–dependent activation

Calcium regulation of muscle tissue is observed to depend on the sarcomere length [35, 45, 54]. The conjecture that Ca^{2+} sensitivity is due to changes in the spacing between the thick and thin filaments is responsible for this dependence was largely accepted [55]. It was supposed that the sarcomere maintains constant volume during contraction and therefore, it was expected that the spacing between the thin and thick filaments decreases with lengthening of the sarcomere. On the molecular level this conjecture is explained as follows: when getting closer to actin myosin heads may have an increased probability of strong cross-bridge formation. Sophisticated experimental techniques were improved, in which myofibrils are compressed via the osmotic pressure that is obtained by adding dextran to the flow-cell solution. Several experiments have provided some support to this theory [56, 57].

A more recent experiment on cardiac myofibrils, realized by de Tombe et al. [58], discredited this hypothesis bringing forward the idea that activation depends on the tension of myofilaments. The authors realized a comprehensive series of experiments, concluding that the decrease of inter–filament distance might not be

31

the primary mechanism generating length–dependent activation. Moreover, the authors suggest that the molecular mechanisms that underlie this phenomenon are governed by structural and functional modulation of the sarcomere proteins which depends directly on the sarcomere length. Many different underlying mechanisms — some of them involving titin — could produce this result and I am not going to discuss them all here. The one I am interested in is related to calcium. The length–dependent activation might be governed by cooperative binding of calcium along the thin filaments, sensitive to the filament tension itself and hence to the sarcomere length. A possibility to model this cooperative binding is to introduce a sarcomere length dependent correlation length for calcium binding along the actin filament. Further experimental work has to be done to shed light on this issue.

The phenomenon outlined in this section is of great interest in cardiac muscle research although it is observed also in skeletal muscle [59]. A brief description of similarities and differences between skeletal and cardiac muscle tissue is given in the following.

In skeletal muscle, individual myocytes are fully activated via motor nerve activity. Thus, muscle force is mainly tuned via motor unit recruitment. In contrast, the cardiac muscle is activated by *calcium–induced calcium release* mechanism: the electrical stimulation readily spreads via low resistance gap junctions. All striated muscle, skeletal and cardiac, are fundamentally the same, i.e. the same type of proteins make up the sarcomere, but they differ in terms of the specific isoforms expression of these proteins. This may explain the greater myofilament length-dependent activation observed in cardiac muscle with respect to skeletal muscle.

1.6.4   ADP–regulated activation

It is worth noting that activation is observed even in absence of calcium ions. In this case, activation is generated by an ADP concentration in the flow-cell solution [60,61]. In recent years, experiments on ADP activation where put forward and particular interest was given to the spontaneous oscillations (SPOC) observed [62]. SPOC were first observed in calcium activated muscle [63]. It was even realized a single–motor experiment in which ADP-induced activation was tested [36]. An

intact thin filament was reproduced by combining the F-actin with the regulatory proteins, troponin and tropomyosin. In this work, the following conjecture was made to explain the mechanism of ADP-induce activation at the molecular level. It was suggested that fluctuations of the tropomyosin strand occur due to Brownian motion. These spatial fluctuations are responsible for partial exposition of the docking site on the actin filament. Therefore, rare events are possible in which the myosin domain can bind actin, even when troponin is not activated. A high ADP concentration induces strong binding between actin and myosin, so that these rare events have a greater probability to occur. Once the actin-myosin binding has occurred, tropomyosin is moved to a peripheral location by the attached myosin domain. All the docking sites belonging to this regulatory unit become exposed to interaction with myosin and strong bonds are favored by the high ADP concentration. In conclusion, activation has taken place.

This scenario on the nanoscale is in agreement with the model dynamics I consider here. Under the above assumptions on the molecular mechanisms, ADP regulation goes along with the exposition of the docking sites just like the effect of the activation through calcium ions. We may imagine that ADP-activation will not reach the tetanus level, but maybe low activation. Indeed, SPOC were first observed in myofibrils for activation through low calcium concentration [45,63].This conjecture is also in agreement with the experimental observation of SPOC for activation by low calcium concentrations. In conclusion, we may say that ADP-activation is roughly equivalent to activation through low concentrations of calcium ions.

Chapter 2

Modeling muscle contraction at the nanoscale

2.1 Classification of molecular motors

On the nanoscale the mechanism of muscle contraction is driven by the Myosin II molecular motor. Many different kinds of molecular motors exist with different roles. They are important for the functioning of cells and different approaches were developed to study them. In this section, I give an overview on molecular motors, mainly to characterize the muscle motor.

Definition of molecular motors Molecular motors are biological molecular machines that convert the chemical energy derived from the hydrolysis of ATP into mechanical work. In the ATP-hydrolysis reaction they have an enzymatic role, they induce the hydrolysis reaction without changing their own chemistry. Molecular motors operate in the thermal bath, an environment where fluctuation due to thermal noise are significant.

Transverse and rotatory motors Many different kind of motors exist in nature. Motors can be distinguished in transverse and rotatory with respect of the kind of motion they generate. Rotatory motors are found to manage the selective permeability of the cell membrane via channels and ion pumps for example. Transverse motors are responsible for the transport, muscle contraction, and deformation of the cell. Three different families of transverse motors are known: kinesin, dynein,

myosin; kinesin and dynein move along tubuli, while myosin acts on the F-actin.

Porters and rowers   Transverse molecular motors have two active domains, they can be classified in porters and rowers [64]. Porters are called the motors that never get completely unbound from the supporting protein, respectively the microtubules or the actin. The motor protein has two active domains and at least one of them is attached to the support. Porters move stepwise along the partner protein. Contrary, rowers may be completely unattached from the supporting protein, even if they have two active domains. The myosin II motor in the muscle is a rower.

2.2   Modeling molecular motors

Molecular motors are of the dimension of ~ 10 nm, their dynamics cannot be observed directly. Micromanipulation experiments allow for the measurements of displacement and force generated by a single motor or collective motor system (see Sections 3.1 and 3.4). Modeling molecular motors is a tool to interpret and inspire the indirect measurements of motor behavior. To this end, models were designed on various length scales. To choose between them the modeler has to evaluate which model better correspond to the aim of his or her work.

Detailed models may describe more directly the biophysical states during hydrolysis. This kind of models have the advantage to consider a big number of information about the fine mechanism and they may work for a lot of different situations. On the other hand these models are characterized by a large number of parameters, which are not easy to fix, because experimental data does not yet exist to well constrain the rate constants and parameters.

Contrary, simplified, coarse models are based on very few parameters to be set. This is a great advantage, because they are less arbitrary and parameters can be better constrained with experiment. These models will lack of generality because they do not go into the details of the mechanism, the simplicity may preclude versatility and extensibility to other applications.

The best compromise is given by the model that requires the minimum mechanistic detail needed to recapitulate the phenomena of interest. In the following

some examples are given for different approaches.

Molecular motors move in biological systems where they are surrounded by a thermic bath. It is widely assumed that the thermal energy has a crucial role in motor dynamics. In a coarse model, the motor can be described as a Brownian particle.

The theory of Brownian motion was formalized by Einstein and Langevin at the beginning of the 19th century [65–68], it describes a particle suspended in an isothermal solution. The motor protein is some order of magnitude bigger than the molecules in solution (~ 0.1 nm), therefore the hypothesis of scale division required to observe Brownian motion is verified. The motion of the Brownian particle is described by the Langevin equation.

The motor consumes energy to generate force, this is modeled by introducing an interaction potential between the motor and the supporting protein in the Langevin equation. The potential energy is characterized by at least two different states; the transition between the two states is designed to furnish the system with chemical energy (ATP-hydrolysis-cycle).

2.2.1   Coarse cross–bridge models

There are mainly two different approaches to model the energy transfer, the cross–bridge model and the Brownian ratchet. In the cross–bridge model at least three states are distinguished, two states with strong interaction (pre and after–stroke) and one weakly bound state (see Section 1.3.2, Fig. 1.10). The weakly bound state represents the free state, in which actin and myosin do not interact, while the attached state before the power stroke and after the power stroke correspond to the strongly bound pre and after–stroke states. In every state the potential energy is given by a harmonic function, the stiffness of the strong bound states are greater than the stiffness characterizing the weakly bound state. The equilibrium position changes from the pre–stroke to the after–stroke state; the power stroke is modeled by the transition between these two states. The transition between the states is determined by the transition rates which generally depend on the motor position.

This model was employed by Duke [69] to implement a collective serial system

of molecular motors, representing a filament. He supposed strain dependence of the transition rates and a suitable compliance to allow for the interaction of many motors contemporarily. Duke confronted the response of a system of 50 filaments linked in series with the experimental results of velocity as a function of load, the results were in excellent agreement. Hence, the coarse model reproduces successfully experimental results obtained for tetanized myofibrils directly from the filament setup, without considering the parallel system of filaments in the sarcomere. Further, averaging the dynamics of many filaments dragging a certain load, Duke found stepwise movement for loads near to the isometric load. In this latter numerical experiment the filaments are supposed to be independent from each other.

Other approaches were setting forth, e.g. the discrete master equation is used to implement the cross–bridge model [70], a review can be found in [71].

2.2.2 Brownian ratchet models

The model of the thermal ratchet was first introduced by Feynman [72]. The model is characterized by a sawtooth potential and under the condition of a thermal gradient the ratchet produces force. In isothermal conditions, the ratchet is not able to produce force; energy has to be pumped in the system. The model was extended to allow for energy supply through chemical reactions, at least two different chemical states are necessary: an interactive state and a free state or even two well chosen interactive states. Muscle motors can be modeled considering an interactive and a free state, they represent respectively the attached and the unattached state of the motor domain. The cyclic transition between these states represent the ATP-hydrolysis. This modified ratchet is called Brownian ratchet, for review see [73–78].

The Brownian ratchet is studied for an unbounded number of motors which are characterized by a distribution function. Shimowaka et al. [79] calculated analytically the Gibbs free energy and the net displacement as a function of transition rates for an unbounded ensemble of motors under stationary transition conditions. The authors used a three state Brownian ratchet whose states were chosen similar to the three states of the cross–bridge.

Also an analytical approach to bounded ensembles of motors was set forward by Gaveau et al. [80]. Another contribution to the characterization of Brownian ratchet models was given by Jülicher et al. [1, 81]. The behavior of unbounded ensembles of motors was characterized in the stationary state. Non–trivial behavior was found for a two–state Brownian ratchet, e. g. spontaneous oscillations were observed in certain ranges of the transition rates, and further, spiral motion was found in two dimensions. These characteristics seem to be appropriate to describe the oscillations in insect flight muscles or the movement of actin in the cytoskeleton respectively.

The two–state Brownian ratchet was also integrated numerically. In this case, the system comprises a bounded number of linked motors moving on the same support [82]. The response was studied comparing an asymmetric potential shape with a symmetric one. For the symmetric sawtooth potential and under load the system shows bidirectional motion, i.e. it inverts velocity unexpectedly. The same behavior was not found for the asymmetric sawtooth potential. This phenomenon is observed experimentally for collective systems of transverse porter–like motors, e.g. kinesin.

2.2.3   Towards detailed models

To understand the fine mechanism of motor activity more detailed models are designed. Obviously there is no clear cut between coarse and detailed models. Here, I consider a detailed model, the model which does not focus only on the very fundamental dynamic functions of the motor but aim to comprehend for molecular or chemical details. This model is always a coarse model with respect to the atomistic length–scale.

Recent work is done on models combining coarse models with molecular simulation [83–85]. The attempt is to overcome the lack of parameters determined by experiment by ab initio simulation and the aim is to shed light on the molecular mechanism of motor mechanics. Another approach is to model details of the chemical transitions during the hydrolysis cycle. To this end, the cross–bridge model is used and further internal states are introduced in the system to describe the APT-hydrolysis. [86–88].

2.3 The 1D two state model

In this thesis, we are interested to investigate the role of active proteins in the activation process of muscle tissue. The tissue is intended to be a macroscopic portion at least at the micro-scale, i.e. the sarcomere scale. The sarcomere is composed of thousands of thin and thick filament pairs, each filament pair has hundreds of motors on the thick filament. To model a huge collective system a Brownian ratchet coarse model is chosen.

I suggest that the filament setup (serial motors) and the sarcomere setup (parallel filaments) is important to the dynamics under partial activation. Hence, the single motor system will be extended to these two types of collective systems. The simplicity of the model allows for a good control on the model parameters; nearly all model parameters have a direct physical interpretation.

Further my aim is to extend the model to allow for varying activation. The simplest mechanism of activation is a switch–like mechanism that can be conceptually easily introduced in the ratchet model (see Section 4.1).

2.3.1 Interaction potential and equations of motion

The 1D model, I set forth in this work, describes the dynamics of the myosin II motor on actin and is based on the two state ratchet model [1]. One molecular motor is composed of two bodies, respectively the myosin head and the actin filament. The myosin head is regarded as a point-like particle, while the actin filament is represented by a massless rigid rod. The interaction potential between the two bodies describes the interaction due to the activated docking sites on the actin filament.

The system is described by the positions of myosin (x) and actin (y) and its internal chemical state s. The internal state can take two values, corresponding to two different chemical states of the myosin domain during the hydrolysis cycle: (1) interacting, and (2) non-interacting with the F-actin.

The interacting state represents myosin in its ground state (state 1 in Fig. (2.1)), attached to the actin filament, in this state the myosin exerts mechanical force on actin. The latter, non-interacting state is given by the excited myosin head along with ADP and P (step 4 in Fig.(2.1)), here, myosin do not interact
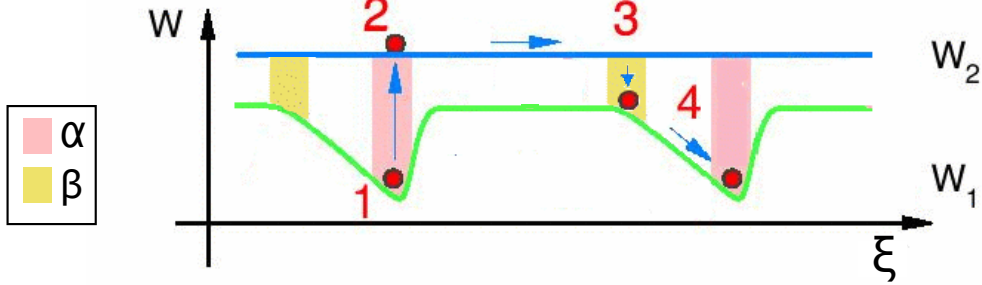
Figure 2.1: The two states of the model are distinguished by the interaction potential. The constant potential function W_2 represents the non-interactive state when myosin is in its excited state, while the sawtooth potential W_1 characterizes the actin-myosin interaction in myosin's ground state. The model dynamics for one hydrolysis cycle is traced in 4 steps (adapted from [1]).

with actin. States 1 and 2 differ in the interaction potential: $W_1 \neq W_2$. The interaction potential depends on the relative position between actin and myosin $(x - q)$. W_1 is a periodic function in the relative position $(x - q)$. In a period there is an asymmetric potential hole (see Fig. (2.2)). The movement of the interactive complex towards the potential minimum represents the power stroke.

$$
W_1(\xi) = \begin{cases}
P(\xi) & 0 < \xi < L \\[2mm]
W_{max} & L < \xi < T \\[2mm]
\text{with} \quad \xi = (x - y) \mod T,
\end{cases}
\tag{2.1}
$$

Where $P(\xi)$ is a polynomial expression. Since state 2 is non-interacting, the potential W_2 is flat.

Within each state $(s = 1, 2)$, positions (x, y) evolve according to the Langevin equations; molecular masses are very small so that in biological systems the equations of motion are well described by the Langevin equation (2.2) in the overdamped regime:

$$
\gamma \dot{x} = -W_s'(\xi) - V_M'(x) + \eta_M \,,
\tag{2.2}
$$

Interaction potential W_1
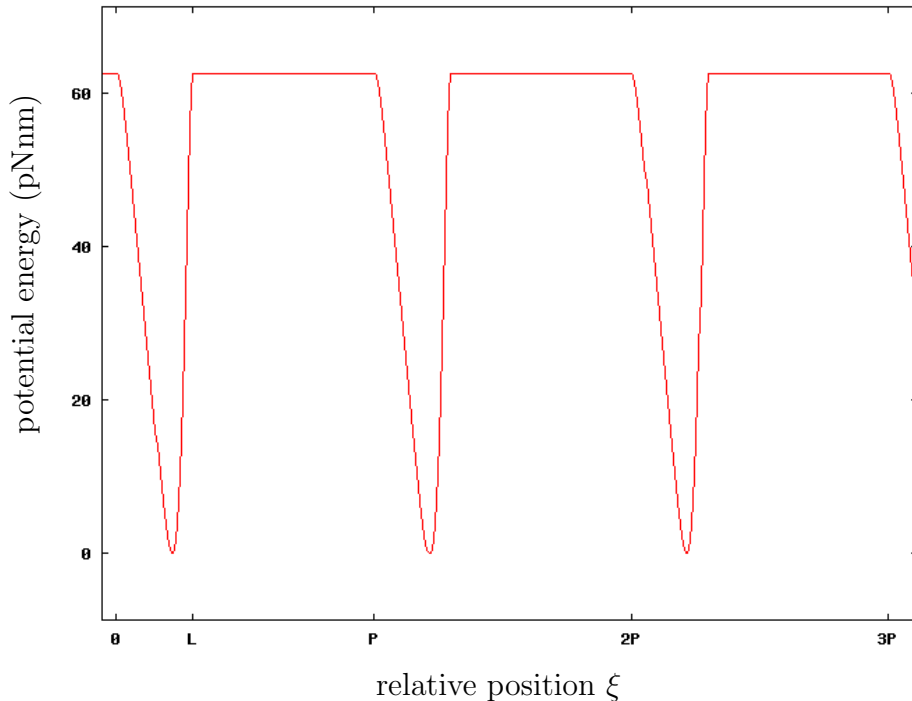
Figure 2.2: Interaction potential vs. F-actin position. T is the period of this periodic potential, while L is the extension of the potential hole. The hole is asymmetric. Here it is assumed $x_{eq} = 0$.

$$\gamma \dot{y} = +W_s'(\xi) - V_A'(y) + \eta_A \,, \quad \text{with} \quad \xi = x - y \tag{2.3}$$

where γ is the Stokes friction coefficient, V is the external potential function, m the mass of polystyrene beads and η the gaussian white noise due to solution:

$$\langle \eta(t)\eta(t+\tau) \rangle = 2k_B T \gamma \delta(\tau). \tag{2.4}$$

η satisfy the fluctuation-dissipation theorem. The tags M and A refer to myosin and actin respectively. The interaction potential depends on the relative position between actin and myosin ($\xi = x - y$), therefore we have $d/d\xi\, W_s(\xi) = d/dx\, W_s(\xi) = -d/dy\, W_s(\xi)$.

2.4 Transition dynamics

The ratchet does not produce net motion if there is no energy transfer to the system. In the motor dynamics chemical energy is pumped into the system during the ATP hydrolysis. The two state model can be interpreted as a simplified representation of the ATP-hydrolysis cycle. The chemical energy is transferred to the system during the transition between the states.
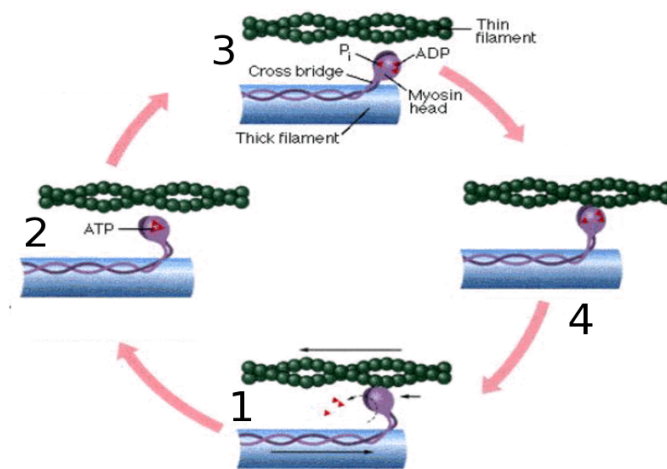
Figure 2.3: Step 1: myosin attached to actin in its ground state. Step 2: ATP adheres to myosin, there is no more interaction between actin and myosin. Step 3: hydrolysis of ATP occurs, myosin has absorbed the released chemical energy and is in its excited state at exoended configuration. Step 4: myosin reattaches to actin in its excited state. Turning to step 1: the excited state decays with the release of ADP and P from the head domain. Myosin turns in the *rigor* state, during this conformational chenge it exerts a force on acting generating the filament to slide.

A scheme of the hydrolysis cycle is shown in Fig. 2.3. The two different dynamical states of the system correspond to the following two chemical states in the cycle:

1. $A \cdot M + ATP + ADP + P$

   (see step 1 in Fig. 2.3: the myosin domain (M) is in its ground state attached to the actin filament (A); ATP, ADP and phosphor are present in the solution)

2. $M^{\star} \cdot ADP \cdot P$

(see step 3 in Fig. 2.3: myosin domain in the excited state (M*) ADP and P adhere to the head)

The transitions between the two dynamical states are given by:

$(1 \rightarrow 2)$: A·M and ATP in solution $\rightarrow$ M* along with ADP and P,

$(2 \rightarrow 1)$: M* along with ADP and P $\rightarrow$ AM*, ADP and P in solution,

where M represent the myosin head in its ground state and M* is the head in its excited state; A is the actin filament and '·' indicate a chemical binding.

Each transition represents a series of chemical reactions. The transition $(1 \rightarrow 2)$ involve at least the following three intermediate states (step 1 to 3 in Fig. 2.3):

- A·M+ATP→M·ATP   ATP adheres to the myosin head

- M·ATP→M·ADP·P   hydrolysis occurs

- M→M* head absorbs released chemical energy

Likewise, the transition $(2 \rightarrow 1)$ resume the following processes (step 3 to 4 in Fig. 2.3):

- M*·ADP−P→M*·ADP+P   P   unbinds

- M*·ADP→M*+ADP   ADP unbinds

- A·M* →M* the excited myosin attaches to the actin filament

The return of the myosin head into its ground state (A·M* →A·M) is modeled by the motion towards the potential minimum (step 4 to 1 in Fig. 2.3).

In conclusion, the model dynamics of the ATP-hydrolysis-cycle can be described in 4 steps (see Fig. 2.1). Initially, myosin is in , state (1), its ground state next to the potential minimum. After a characteristic time, the transition $(1 \rightarrow 2)$ occurs. The system evolves in state (2) until it reaches the yellow transition zone. Once it turns to state (1) the motion towards the potential minimum represents the power stroke dynamic. After reaching the minimum (AM* $\rightarrow$ AM), the initial state is restored.

2.4.1 Modeling chemical reactions

The hypothesis on the basis of our model are:

1. each transition is localized in space, with respect to the relative position of actin and myosin ($\xi = x - y$).

2. we suppose the transition to be well described by their transition times, the mean transition times are $\tau = \exp\left(E_a/k_B T\right)$, where E_a is the reaction activation energy [89, 90].

3. transitions are allowed only in one direction.

The transition $(1 \rightarrow 2)$ from the ground state to the excited state is localized near the local potential minimum, marked as pink zone in Figure 2.1. Within this zone, the myosin head is trapped in the potential minimum, i.e. it is in its ground state. This localization of transition reflects the assumption that the adhesion of ATP to the myosin head is only possible when the myosin head is in its ground state, attached to the actin filament.

The inverse transition $(2 \rightarrow 1)$ is localized at the beginning of the smooth tract of the potential hole, represented by the yellow zone in Figure 2.1).

I suppose that the mechanism of transitions between the two states can be represented as an ordinary chemical reaction. The kinematics of the chemical reaction can approximately be described by the Arrhenius reaction rate:

$$\kappa = K_0 \exp\left(-\frac{E_a}{k_B T}\right), \tag{2.5}$$

where K_0 is a generic constant in temperature, E_a is the activation energy of the chemical reaction process and $k_B T$ is the thermic energy. The transition times from one state to another are given by the inverse of the transition rate [89]. The mean transition times are given by:

$$\tau = \kappa^{-1} = C_0 \exp\left(\frac{E_a}{k_B T}\right). \tag{2.6}$$

The times are distributed with a Poisson distribution. In the model, the transitions are characterized by their corresponding mean transition time, τ_α and τ_β. I suppose

that the chemical reactions occur only in one direction. The transition rates of the single reactions during the hydrolysis cycle are found in literature [11]. In each series of transition it is found that at least one reaction is well approximated by a unidirectional reaction. Therefore it is reasonable to approximate the transitions between the two representative states by unidirectional reactions. This choice differs from literature, where the reactions were mostly described by equilibrium reactions [1, 79, 80].

2.4.2   Fluxes between the two states

The representation of the transition dynamics in terms of the Fokker–Planck equation can be useful to understand the fluxes of the myosin head population between the two states. The transition dynamics can be represented by the Fokker-Planck equation of the myosin head distribution function P_s in each state $s = 1, 2$:

$$\begin{cases} \delta_t P_1 + \delta_x J_1 = \omega_{21} P_2 - \omega_{12} P_1 \\ \\ \delta_t P_2 + \delta_x J_2 = \omega_{12} P_1 - \omega_{21} P_2, \end{cases} \tag{2.7}$$

where J_s is the probability current respectively:

$$J_s(x, y) = \gamma_M^{-1} \left(-k_B T \, \delta_x P_s(x) - P_s(x) \, W_s(x, y) + P_s \, f_{ext} \right), \tag{2.8}$$

γ_M is the friction coefficient for the myosin head, $k_B T$ the thermal energy, $W_s(x, y)$ is the interaction potential function in state $s = 1, 2$ respectivley and $f_{ext} = -\delta_x V_M(x)$ is the force due to the external potential. In Eq. (2.7), the two terms on the left represent the source and sink of population in the corresponding state. The transition dynamics is described by three different Fokker-Planck equations corresponding to the two transition zones $(x \in \alpha, x \in \beta)$ and the zone without transition $(x \notin \alpha, \beta)$:

$$x \in \alpha \begin{cases} \delta_t P_1 + \delta_x J_1 = -\omega_{12} P_1 \\ \\ \delta_t P_2 + \delta_x J_2 = \omega_{12} P_1 \end{cases} \tag{2.9}$$

$$x \in \beta \begin{cases} \delta_t P_1 + \delta_x J_1 = \omega_{21} P_2 \\ \\ \delta_t P_2 + \delta_x J_2 = -\omega_{21} P_2 \end{cases} \qquad (2.10)$$

$$x \notin \alpha, \beta \begin{cases} \delta_t P_1 + \delta_x J_1 = 0 \\ \\ \delta_t P_2 + \delta_x J_2 = 0 \end{cases} \qquad (2.11)$$

The transitions are unidirectional, i.e. that the source and sink terms in each state (see Eq. (2.7)) do not coexist in space ($\nexists \ x \ : \omega_{12}(x) \neq 0, \omega_{21}(x) \neq 0$). The Fokker-Planck equations for the transition zones (Eq. 2.9 and Eq. (2.10)) are characterized or by the source or by the sink term, while in the not–transition zone there is nor a source neither a sink term (Eq. (2.11)).

2.5 Numerical integration

The numerical integration of the two state model is discussed. I first expose the dynamics in the interactive state 1, without taking into account the chemical transitions. Chemical transitions are then introduced and the dynamics is studied for different values of transition times. The choice of the model parameters is discussed in detail in the last paragraph of this section (2.5.4).

2.5.1 Interactive state (1)

Scheme of the single–motor model
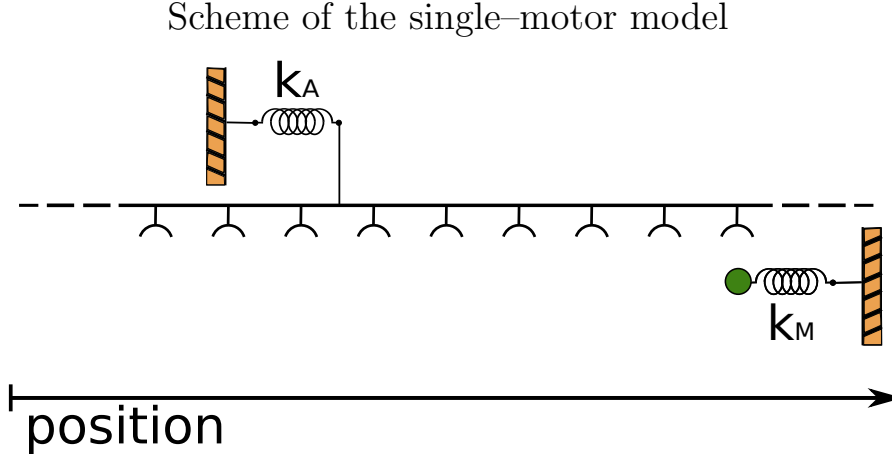
Figure 2.4: The myosin head is represented by a bead (in green), it is linked harmonically to a wall with stiffness k_M; the position of the myosin head is described by x. The actin filament is represented as an unbounded rigid rod with docking sites at equal distances. The F-actin has an external harmonic bond with stiffness k_A, its position (y) is taken according to the link.

I study the dynamics proposed in equations Eq. (2.2) and Eq. (2.3). The external potentials are assumed to be harmonic functions:

$$V_M(x) = k_M(x - x_{eq})^2 \quad \text{and} \quad V_A(y) = k_A\, y^2, \tag{2.12}$$

where k_M and x_{eq} are the stiffness and the equilibrium position of the harmonic bond of the myosin head, while k_A is the stiffness of the harmonic bond on the F-actin, the equilibrium position is taken equal to zero $(y_{eq} = 0)$. A schematic representation of this system is shown in Figure 2.4. In the chemical state 1, the interactive state, the Langevin equations are given by:

$$\gamma_M\, \dot{x} = -W_1'(\xi) - k_M(x - x_{eq}) + \eta_M\,,$$

$$\tag{2.13}$$

$$\gamma_A\, \dot{y} = W_1'(\xi) - k_A\, y + \eta_A \qquad \text{with} \quad \xi = x - y,$$

where x is the position of the myosin head and y the position of the actin filament. γ is the Stokes friction coefficient, and W_1 is the interaction potential energy (Eq. (2.1)). The term η represents the gaussian white noise, η is delta-correlated and

satisfies the flucutation-dissipation theorem (Eq. (2.4)). If the position of the myosin head is fixed in space, the total potential energy of the actin is given by the sum of the interaction potential W_1 and the potential energy due to the harmonic bond V_A (see Fig. 2.5).

| $k_B T$ (pNnm)	γ_A (pg/μs)	γ_M (pg/μs)
4.0	5.0	0.1

Table 2.1: Parameters characterizing the thermic bath and the solvent via the Stokes' friction coefficient of myosin and actin. It is supposed that actin is attached to a polysyterne bead of 1μm diameter; the Brownian motion and the friction of the polystyrene bead is much bigger than that of myosin.

The Langevin equations Eq.(2.13) are integrated by a second-order stochastic Runge-Kutta algorithm [91, 92]. A single integration is called a numerical experiment. Every experiment is integrated over a total time of 5 seconds with a time step of 1 ns.

The amplitude of oscillation is related to the stiffness of the The total potential energy of the actin has local minima (see Fig. 2.5), i.e. metastable states. The transition between this metastable states can be induced by thermal activation. The ratio, $\frac{\Delta W_1}{k_B T}$, characterizes these transitions. The probability of transition between the states depends exponentially $\frac{\Delta W_1}{k_B T}$ (see section 2.4.1, Eq. (2.5) and Eq. (2.6)). The mean life time of the metastable state and the transition rate from this state to another are related as shown in Eq. (2.6)), the activation energy is given by the barrier in potential energy ΔW_1:

$$\tau_{\text{mean lifetime}} = \kappa^{-1} = \exp \Delta W_1 / k_B T. \tag{2.14}$$

In Figure 2.6 the dynamics of the F-actin in the interactive state is traced for three different values of $\frac{\Delta W_1}{k_B T}$. The F-actin is a Brownian particle constrained by the interaction energy with myosin, its external bond. The dynamics is characterized by stochastic oscillations whose amplitude A is related to the variance of the

Potential energy for F-actin with fixed myosin head
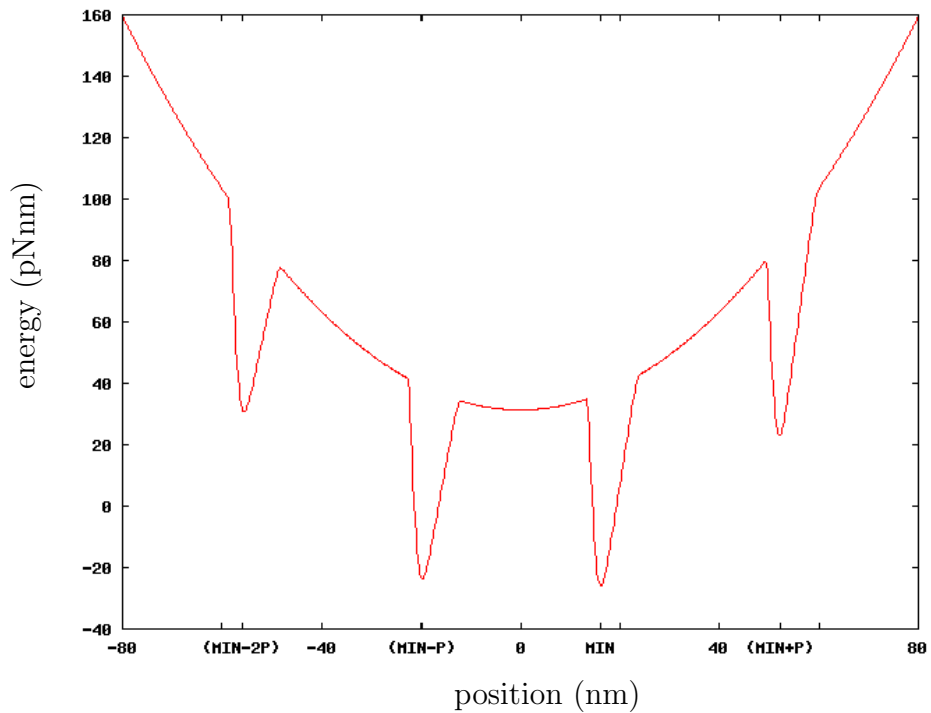
Figure 2.5: The total potential energy of the F-actin at fixed myosin head ($x = x_0$)is given by the sum of the potential energy due to the harmonic bond and the interaction potential W_1. The metastable states correspond to the minima of the interaction potential W_1 which is a function of the relative position of the actin with respect to the fixed myosin position ($x_0 - y$). In the figure the position of the myosin head is fixed so that $x_0 - y_{eq} = 24$ nm. The period of W_1 is equal to 36 nm.

F-actin position in time for different $\Delta W_1/k_B T$
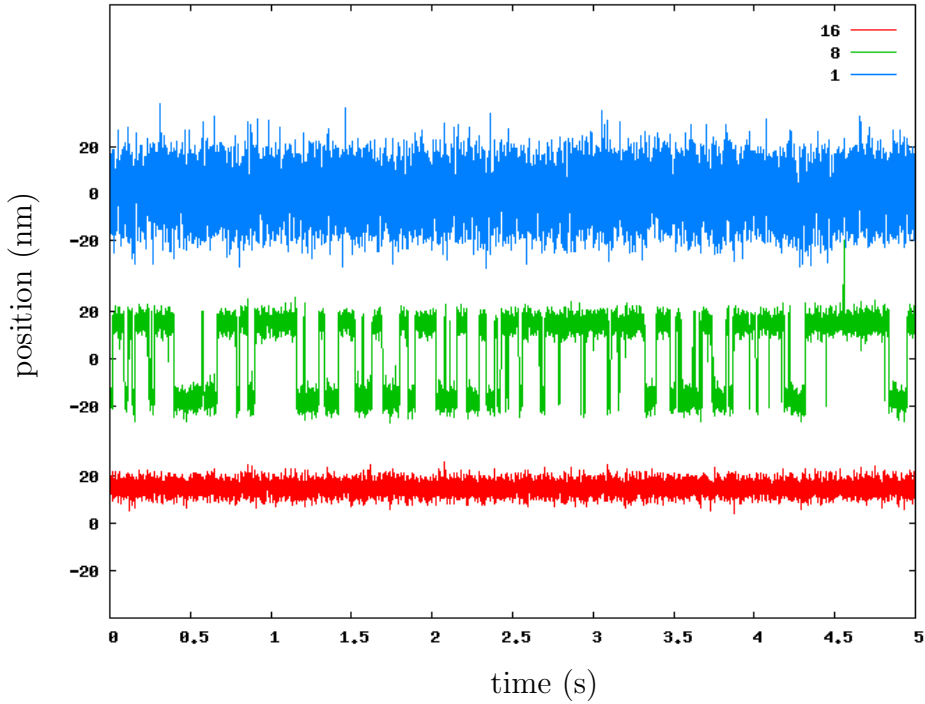
Figure 2.6: Dynamics of the F-actin in the interactive state (1) for different values of $\Delta W_1/k_B T$ (key in figure). For $\Delta W_1/k_B T = 1$ the F-actin oscillates about its the equilibrium position of its external link ($y_{eq} = 0$). For $\Delta W_1/k_B T = 8$ the system is trapped in the metastable states near y_{eq}; in the metastable state the system oscillates about the corresponding local minimum of the interaction potential W_1; the time of escape is small enough to observe hopping between the metastable states. The time of escape from this metastable state increases exponentially with $\Delta W_1/k_B T$ and for $\Delta W_1/k_B T = 16$ the system is trapped in one metastable state during the entire dynamics.

distribution function, i.e. the histogram, $A = 2 \left[D\gamma/k \right]^{\frac{1}{2}} = 2 \left[k_B T/k \right]^{\frac{1}{2}}$, where D is the Einstein diffusion coefficient $D = k_B T/\gamma$ [67].

The amplitude of oscillation varies in the three cases: for $\frac{\Delta W_1}{k_B T} = 16$, the oscillation has an amplitude of ~ 30 nm about zero, the equilibrium position of the harmonic bond ($y_{eq} = 0$ (see Fig. 2.7). In this case, sufficient thermal energy is present not to be trapped in a metastable state, the external bond dominates the dynamics $k_B T$ and the stiffness can be approximated by $k = k_A$ ($2 \left[k_B T/k_A \right]^{\frac{1}{2}} \simeq 28$ nm).

For a lower ratio, $\frac{\Delta W_1}{k_B T} = 8$, the actin position visit mainly two metastable states, corresponding to the minima of the potential W_1 next to the equilibrium position $y_{eq} = 0$ (see Fig. 2.5 and Fig. 2.7). The oscillations of F-actin are constrained by the metastable state whose stiffness can be estimated by $W_1''(\xi_{\min})$ (myosin is supposed fixed in its equilibrium position) and the amplitude of oscillations of the myosin head itself. A rough estimation of the effective oscillations of actin is given by: $2 \left[(k_B T/W_1''(\xi_{\min}) + k_B T/W_1(\xi_{\min})) \right]^{\frac{1}{2}}$. Transitions between two metastable states can be observed.

When $\frac{\Delta W_1}{k_B T} = 1$, the actin position remains trapped in a metastable state for the entire dynamics. The thermal energy is not enough to cause a transition to another metastable state in the time of integration. The amplitude of oscillation is the same as in the previous case, there are no transitions.

I varied the depth of the potential hole in W_1 to obtain different values of the ratio $\frac{\Delta W_1}{k_B T}$, the thermal energy is constant in the three cases, $k_B T = 4$ pNnm; the values of stiffness are $k_A = 0.02$ pN/nm, $k_M = 0.5$ pN/nm and $W_1''(\xi_{\min}) \simeq 1$ pN/nm (see Tab. 2.1 and Section 2.5.4 for model parameters).

Thermally induced transitions between two states obeys detailed balance and at thermal equilibrium they cannot induce net displacement nor generate work.

2.5.2   Stiffness of the neck domain

In this section, the dynamics is investigated for different values of k_M. The free energy of the F-actin is compared to its potential energy calculated for the myosin head fixed in its equilibrium value ($x_{eq} = 24$ nm).

The free energy of the F-actin or myosin head respectively is a function of the
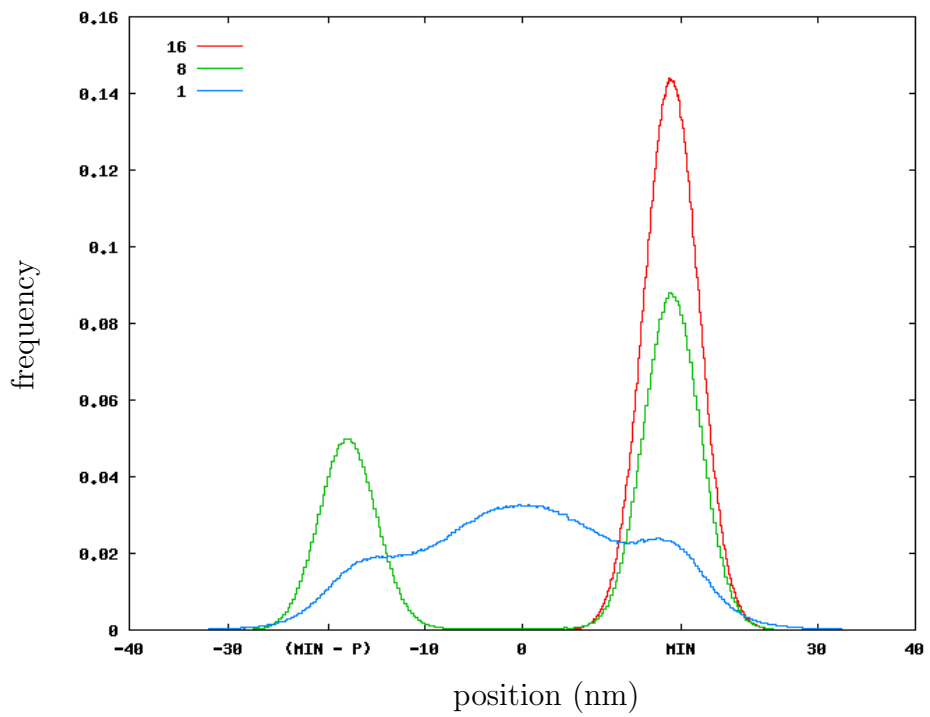
Figure 2.7: Histogram of the F-actin position shown in Fig.2.6; the values of $\Delta W_1/k_BT$ are indicated in the figure.

temperature and the respective position histogram:

$$F(x) = -k_B T \, \log(p(x)), \qquad (2.15)$$

where $k_B T$ is the thermal energy and p is the histogram of the position of the system under exam.

Histogram of F-actin position for different k_M/k_A
($k_A = 0.02$ pN/nm)
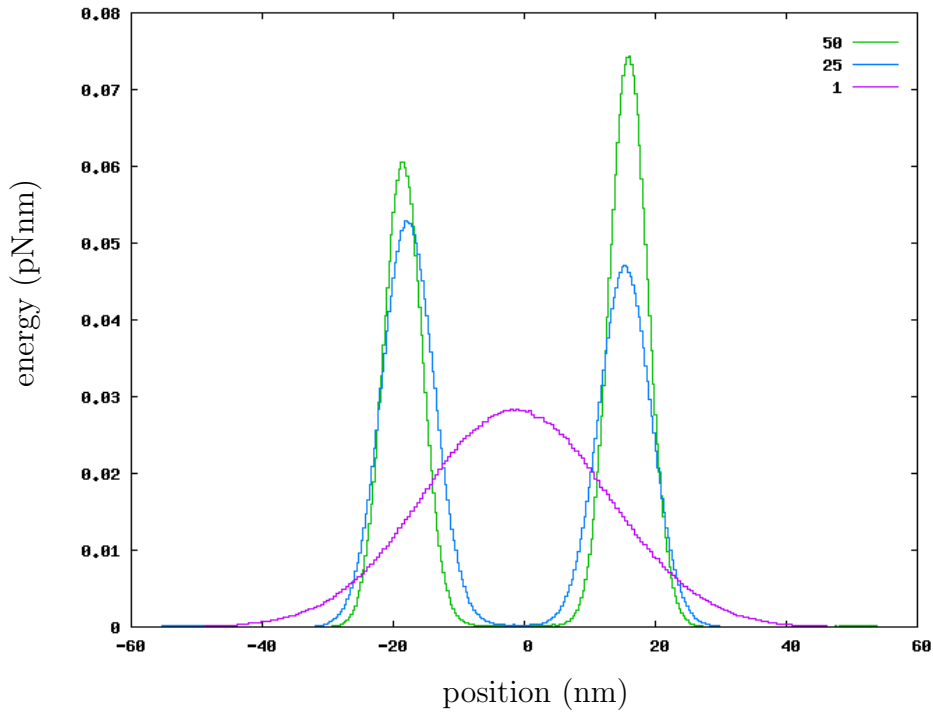
Figure 2.8: The histogram of the F-actin position is traced for different values of k_M/k_A (key in figure) and $k_A = 0.02$ pN/nm. The interaction potential is chosen $\Delta W_1/k_B T = 8$, hence transition between different metastable states can be observed if exist.

In Fig. 2.9 the free energy of the F-actin is shown for different values of the stiffness $k_M = 1.0, 0.5, 0.02$ pN/nm. The stiffness of the harmonic bond of the F-actin is assumed to be $k_A = 0.02$ pN/nm. The interaction potential W_1 is fixed with $\Delta W_1 \simeq 64$ pNnm. The thermal energy is chosen big enough to allow for transitions between the metastable states $k_B T = 8$ pNnm ($\Delta W_1/k_B T = 8$). In

Figure 2.9: Free energy of the F-actin calculated for different values of k_M/k_A. The free energy is compared to the total potential calculated for the position of the myosin head fixed in its equilibrium position ($x = x_{eq} = 24$ nm). For decreasing values the stiffness k_M, the local minima become smoother and disappear completely for $k_M \leq k_A$, while for $k_M \rightarrow \infty$ the free energy function converges to the total interaction potential function.

this way the free energy landscape can be calculated for actin position $\in [-60; 60]$ nm.

The interaction potential W_1 depends on the relative position of both bodies, myosin and actin. In the limit for infinite stiffness k_M, i.e. for myosin fixed in space, the free energy landscape of the F-actin is equal to the internal energy of the system, i.e. to the effective potential energy (see Fig. 2.5 and Fig. 2.9). The free energy landscape of the F-actin varies with the stiffness of the myosin neck domain, k_M. The local minima of the free energy landscape become smoother with decreasing k_M and they disappear for $k_M \leq k_A$.

The myosin dynamics is determined by the same way by the inverse ratio k_A/k_M. To model the muscle motor in an experimental setup, I set $k_M = 0.5$ pN/nm and $k_A = 0.02$ pN/nm, i.e. $k_M \gg k_A$ (see Section 2.5.4 and Chapter 3). In this case, the myosin dynamics is dominated by its harmonic bond to a fixed point.

2.5.3 Chemical transition

Chemical transitions are now introduced in the dynamics. The analysis of the model dynamics in the interactive state (1) showed that transition between the metastable states can be induced by thermal energy. Here, $k_B T / \Delta W_1 \ll 1$ is chosen to reduce the number of thermal transitions. Consequently, the transition between metastable states is generated mainly by the chemical transitions.

Chemical transitions are implemented through the extraction of Poisson-distributed random transition times. Each transition is characterized by its mean transition times τ_α and τ_β. Transition is allowed within the respective transition zones (see Fig. 2.1 in section 2.3): the transition from the interactive state (1) to the non-interactive state (2) occurs in a narrow zone about the local minima of the interactive potential W_1; the inverse transition, from state 2 to state 1, is localized at one side of each potential hole (W_1).

The mean transition time τ_α characterizes the transition from the interactive state (1) to the non-interactive state (2). For increasing values of τ_α, the corresponding transition becomes slower and the system will stay for longer times in the interactive state. Vice versa, when τ_α decreases the permanence in the interactive

F-actin position in time, $\tau_\beta = 90$ ns
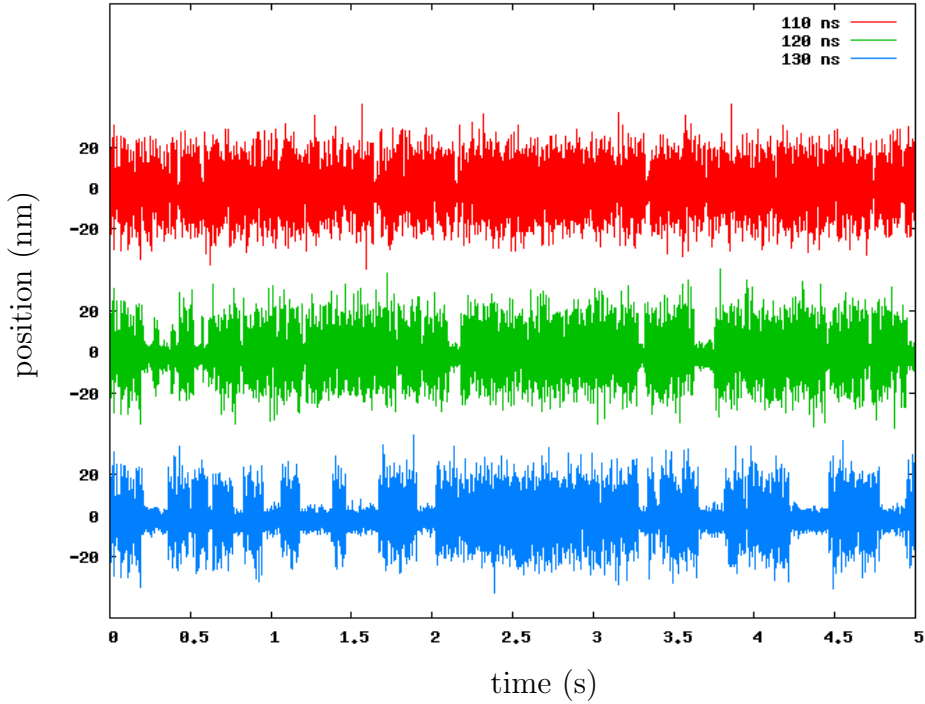
Figure 2.10: Dynamics of the F-actin in the two state model. The three cases show the behavior of the F-actin for three different values of the mean transition time τ_α. This time determines the transition from the interacting state to the non-interacting state. When interacting occurs the F-actin is trapped in a metastable state; this leads to a reduction of the amplitude of stochastic oscillations. For increasing values of τ_α the permanence in the interactive state increases. The mean transition time, τ_β, is the same in the three cases ($\tau_\beta = 90$ ns).

state decreases as well. As a consequence, the number of the inverse transitions increases slightly .

The mean transition time τ_β determines the transition dynamics from state (2) to state (1). The consequences of the choice of τ_β for the dynamics are shown in Fig. 2.11. For big values of τ_β, long times are needed to transit from the non-interactive state to the interactive state. Consequently, the occurrence of the interactive state is low. If τ_β decreases, even the mean life time of state (2) decreases and the number of transition occurrence increases. In the histogram (see Fig. 2.12), the information about permanence and occurrence is lost, it does not account for all

F-actin position in time, $\tau_\alpha = 120$ ns
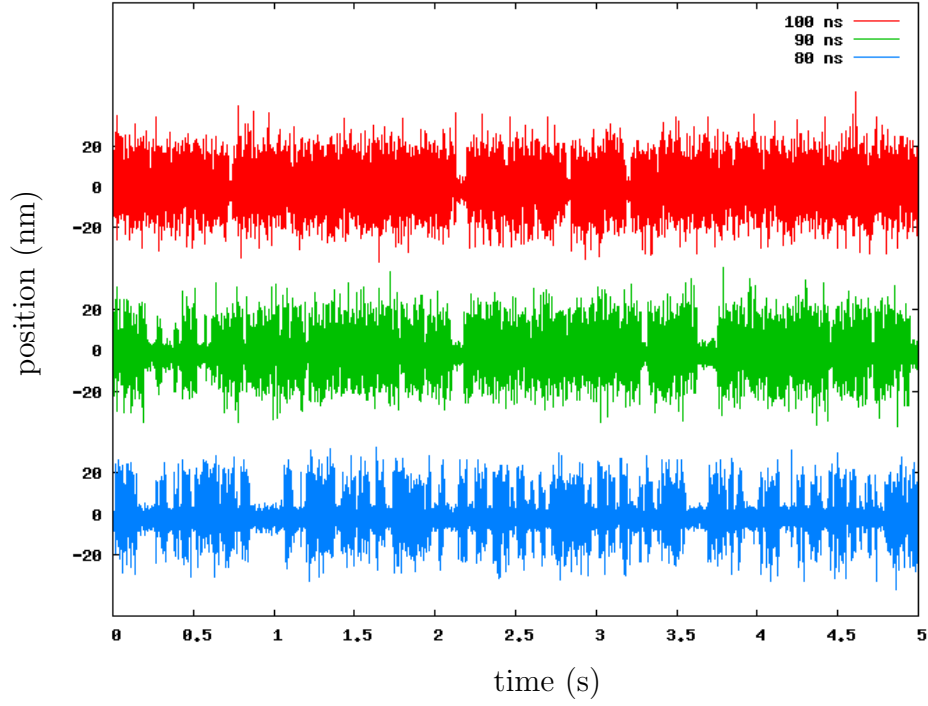
Figure 2.11: The dynamics of the F-actin in the two state model is represented for three different values of the transition times τ_β. With the increasing mean value, τ_β, the time needed to transit from the non-interactive state to the interactive state increases. Consequently, the occurrence of the interactive state decreases. The mean transition time, τ_α, is the same in all cases ($\tau_\beta = 90$ ns).

details of the dynamics.

The two transition times, τ_α and τ_β, can be determined independently from each other. This allows to control permanence as well as occurrence of the interactive state. In particular the transition times can be chosen to represent the times of chemical transitions in physiological conditions: The characteristic time of a hydrolysis cycle is $\sim$ 1ms and during one cycle the actin-myosin interactive state has a duration of $10 - 100\mu$s [11]. The mean lifetime of the attached state and the occurrence of this state are controlled by the mean transition times.

Histogram of the F-actin position

$(\tau_\alpha = 90$ ns$)$ $\qquad\qquad\qquad (\tau_\alpha = 120$ ns$)$
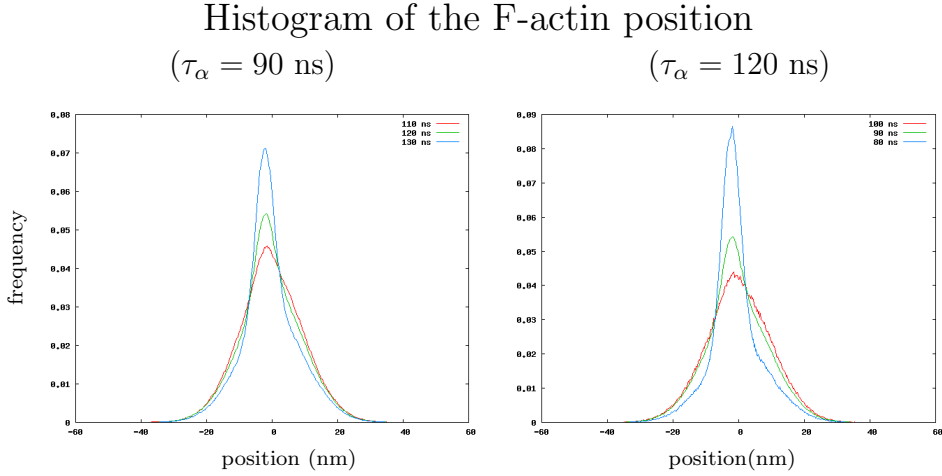
Figure 2.12: The histogram are shown corresponding to the dynamics traced in Fig. 2.10 (left) and Fig 2.11 (right). The key in the figure indicates the different values of the mean transition time τ_β in the left figure and τ_α in the right figure.

2.5.4 Model parameters

The dynamics of myosin motors generates piconewton forces on nanometer distances. Therefore, the natural choice for the force-, length- and time-scale to describe the model dynamics is given by (pN, nm, μs).

The thermal energy for $293K(20^oC)$ is approximately $k_BT = 4$ pNnm. The stiffness of the myosin neck domain is assumed to be $k_M = 0.5$ pN/nm; this value is chosen in agreement with indirect experimental measurements of the stiffness by single motor manipulation experiments [93]. The Stokes friction coefficient is given by $\gamma = 6\pi a\nu$, where a is the radius of the Brownian particle and ν is the viscosity of the solvent. In literature, the estimate of the friction coefficients was made using the viscosity of water. The particle radius obtained by studies on structures of the myosin head $r \simeq 10$ nm [94] leads to $\gamma_M = 0.1\frac{pg}{\mu s}$. The friction coefficient of actin is taken $\gamma_A = 5\frac{pg}{\mu s}$. This value corresponds to the friction experienced by a sphere of radius $0.5\,\mu$m. Polystyrene beads of this dimensions are used to realize experimental setup in laser trap assays.

In the next chapter, two experiments are described in detail that employs the laser trap technique (see section 3.1 and 3.4). In these experiments the laser trap stiffness is set in the range $[0.02; 0.08]$ pN/nm. In the examples discussed in

ΔW_1 (pNnm)	$W_1''(\xi_{\min})$ (pN/nm)	$L_{\text{potential hole}}$ (nm)	zone width (α, β) (nm)	zone distance (nm)
62	1.0	10.5	1.2	7.8

Table 2.2: Parameters determining the interaction potential and the transition zones. The interaction potential is characterized by the difference in potential energy of the potential hole and the extension of the hole; the part of the potential energy representing the *power stroke* is delimited by the transition zones. The characteristics of the transition zones are determined by the zone width which is the same for both zones (α and β) and the distance between the center of the two transition zones respectively (zone distance).

previously (Sections 2.5.1, 2.5.2 and 2.5.3), the stiffness of the harmonic bond on the actin filament is chosen within this range, $k_A = 0.02$ pN/nm.

The period of the interaction potential, W_1, represents the periodicity of the docking sites on the actin filament (Section 1.1). The docking sites are given by the actin units available to the myosin heads on the thick filament; the period of docking sites is equal to the period of the helix ($P_{W_1} \simeq 36$ nm). If the actin filament can rotate about its axis, more docking sites become available to the myosin heads and the distance between the sites shortens. The distance of two adjacent sites on the helical structure is 5 nm.The period of docking sites reduces to 5 nm when the myosin head can attache to every actin unit on the filament. In the model, the inferior limit of periodicity is given by the extension of the potential hole, $L_{\text{potential hole}} = 10.5$ nm.

Chapter 3

The model dynamics compared with experiment

3.1 The single–motor assay

The single motor assay realized by J.T. Finer, R.M. Simmons and J.A. Spudich [7] was the first experimental measure of the interaction between a single myosin domain and an actin filament.

<div align="center">Scheme of experiment</div>
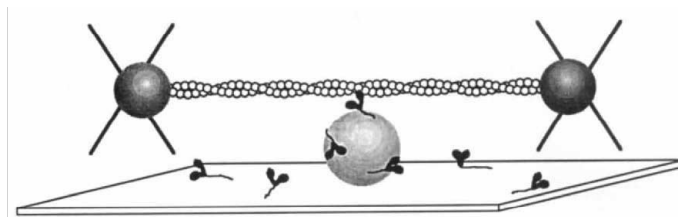
Figure 3.1: Both ends of an actin filament are attached to a polystyrene bead respectively. Each bead is trapped by an optical tweezer with regulable stiffness. A silica bead is fixed on the substrate. The tails of myosin domains are disposed to attach to the silica bead. The concentration of myosin domains in solution is low enough that only one of the attached myosin domains has a suitable position to allow for interaction with the actin filament. The position of the polystyrene beads are measured as a function of time. Reproduced from [7].

In the experimental setup, the actin filament is attached at both ends to a

polystyrene bead. The two polystyrene beads are trapped in an optical tweezer; the filament is then held in tension ($\sim$ 2 pN); the laser trap has a feedback system to guarantee that this tension stays constant during experiment.

A silica bead, fixed on a glassy surface, is immersed in a solution with myosin II double-head domains. The tails of myosin domains like to adhere to silica, but the concentration is low enough, that only few domains adhere to the bead. With high probability, only one of these attached domains has a suitable position to allow for interaction with the actin filament (see Fig. 3.1).

The actin filament is then brought close to the silica bead and its kinetic is observed. The laser trap stiffness is held as low as possible to allow for large displacements. The idea of the authors was to measure the displacement due to the swinging lever arm, i.e. the amplitude of the power stroke. They found evidence for net displacements with mean value of $\sim$ 11 nm. The same experimental setup can be used in isometric conditions when raising the laser stiffness so that the oscillations of actin are reduced significantly. Force transients were measured in isometric conditions obtaining a mean value $\sim$ 4 pN.

In Fig. 3.2 the dynamics of a single polystyrene bead is shown. The laser trap stiffness is low (each trap 0.02pN/nm), the system can move over large distances. The concentration of ATP varies: a (2 mM), b (10μM) and c (1 μM). The upper trace in each record shows the movement of the bead in the direction along the actin filament. The lower trace in each record shows the movement in the perpendicular direction.

In the perpendicular direction, stochastic oscillations about a constant mean position are observed. This dynamics is due to the Brownian motion of the bead under an external elastic bond. The movement in this direction is not affected by the interaction between actin and myosin. The upper trace shows intervals of stochastic oscillations about the zero mean position alternating with oscillations about a shifted mean position. The displacements occur in the positive direction. The amplitude of oscillation about the shifted mean position decreases with respect to the oscillations about the zero mean position.

Dynamics measured by experiment
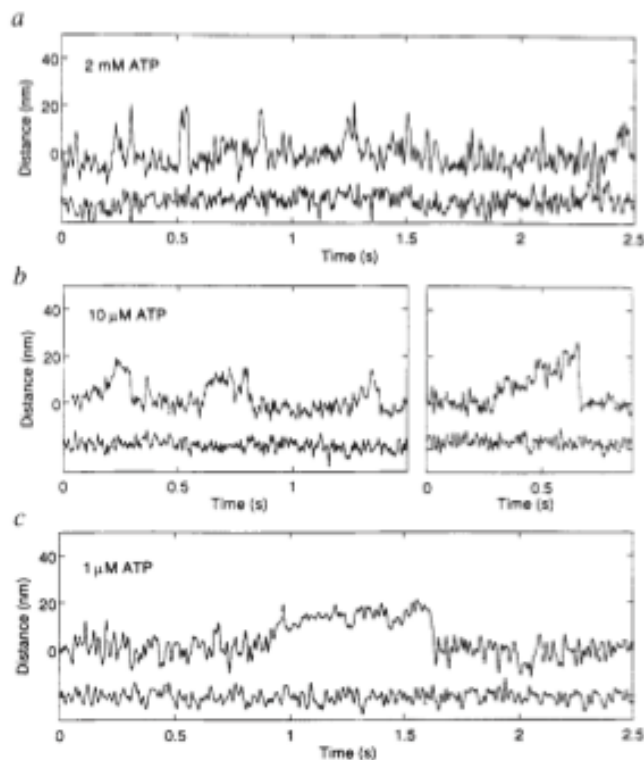
Figure 3.2: The displacement of the polystyrene bead is traced as a function of time measured by Finer, Simmons and Spudich. The experiment is repeated for different concentrations of ATP in the flow cell solution. Independently from the ATP concentration, there is an evidence of net displacements of up to 20 nm. The amplitude of oscillation decreases during displacement. The duration of the displacement increases with decreasing ATP concentration. From top to bottom: at [ATP] = 2 mM the displacement lasts for less that 0.1 s, at [ATP] = 10 μM the duration of displacement is of the order of 0.1 s, and at [ATP] = 1 μM it lasts even longer than 0.5 s. Reproduced from [7].

3.1.1 Interpretation of experimental data

In Figure 3.2, the duration of the displacements increases with decreasing concentration of ATP in the flow cell: in a the net displacement is given by a narrow peak (<0.1 s), in b the displacement persists for times of the order of 0.1 s and in c a single displacement in shown with the duration of more than 0.5 s.

This dynamics in the direction along the actin filament was explained by Finer et al. as follows: the polystyrene bead in solution undergoes Brownian motion; in the absence of interaction between actin and myosin stochastic oscillations about the zero mean position are observed. The displacements are supposed to be generated by the interaction of actin and myosin; when oscillations about the shifted mean position are observed, myosin is attached to the actin filament.

There is a good agreement between the experimental results and the crossbridge model: the less ATP is available, the more time myosin will stay attached to the actin filament. To break the bond between myosin and actin, ATP is required. In conclusion, the authors suggested that the measured displacements are generated by the actin–myosin interaction. The amplitude of displacement is associated with the power stroke. It is worth noting that net displacements were observable only if they were larger than the amplitude of oscillation in the free state.

One year later Molloy et al. [8] devised a method to overcome this limitation. The authors utilizes the following assumption: the actin-myosin interaction force furnishes an additional constraint on the polystyrene bead which leads to the decrease of the oscillation amplitude. The intervals in which myosin is attached to actin can therefore be identified with the intervals in which the motion has a small oscillation amplitude.

The measurements were analyzed with both methods: the authors found principally positive displacements and a moderate amount of negative displacements with displacements larger than 5 nm, when identifying the attachment of myosin to actin by measuring the net displacement (same technique used by Finer et al.). In this way, it is not possible to observe displacements due to the interaction minor then sim 5 nm, i.e. within the half amplitude of the residual Brownian noise. Consequently, the authors suggest that the histogram of the positions during at-

Histogram of F-actin position in the attached state
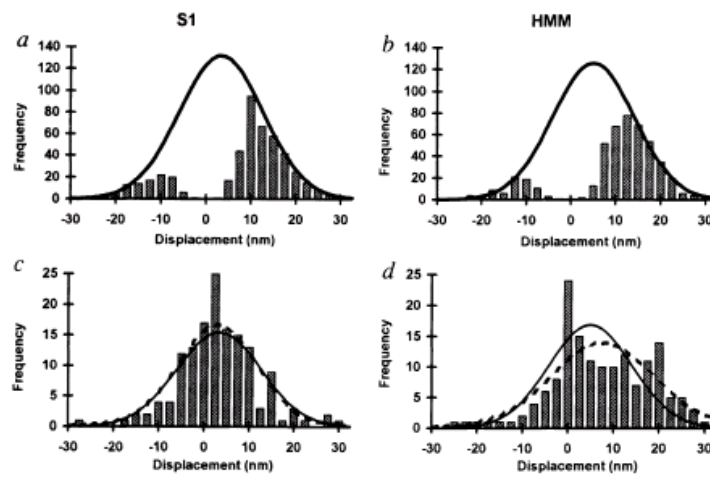
Figure 3.3: Two different measurement techniques are used. Top: the direct measure of displacement. Bottom: the identification of attached states via the amplitude of oscillation. These two techniques are respectively applied on a single myosin head S1 (on the left) and the HMM double-headed complex (on the right). The histograms are obtained using *a*) 39 traces from 18 filaments, *b*) 73 traces from 21 filaments, *c*) 9 traces from 5 filaments, and *d*) 5 traces from 2 filaments. The fits are Boltzman distributions, their mean value represent the displacement caused by the power stroke. There are no qualitative differences in the results of the two experimental setups. Reproduced from [8].

tachment measured with the previously described technique, reproduces the *true* histogram only a partially; during interaction, the bead can also be found in positions near zero. The *true* histogram can be measured by identifying the interaction dynamics with the observed reduction of the stochastic oscillation amplitude instead of net displacement (see Fig. 3.3).

technique of measurement	S1	HMM
net displacement	3.5 nm (39,18)	5.0 nm (73, 21)
oscillation amplitude	3.3 ± 0.73 nm (9, 4)	7.9 ± 0.91 nm (5,2)

Table 3.1: In the table are listed the mean position measured with the two different experimental techniques, i.e. using the direct measurement of displacement and using the measurement of the oscillation amplitude. In the parenthesis, are indicated respectively the number of traces and the number of filament used to obtain the data [8].

To investigate the difference between single myosin domains, S1, and double-headed domains, HMM, Molloy et al. realized the single motor assay for both complexes. Each experiment was repeated 10-20 times. The resulting histograms show the same qualitative behavior (see Fig. 3.3); they were fitted using the Boltzman equation $A \exp\left(-\frac{\kappa}{2}(x - x_0)^2/k_B T\right)$. The results of fits are listed in Tab. 3.1.

The ensuing picture can be described as follows: the F-actin attached to the polystyrene beads oscillates for thermal activation, the amplitude of the oscillation depends on the external constraint due to the laser trap through the ratio $k_B T/k_{LT}$ [67] (see Section 2.5.1). From time to time, the myosin domain fixed on the silica bead binds to an actin unit and the oscillation amplitude of actin becomes smaller;

in the attached state the effective stiffness on the F-actin increases because its interaction with the myosin head. An effective stiffness that constrains the F-actin in the attached state is called k_{AM}, with $k_{LT} < k_{AM}$. Hence, it is obtained $k_B T / k_{LT} > k_B T / k_M$, where k_{LT}.

When myosin attaches to actin, it exerts the power stroke. The position of actin is shifted about the displacement due to the power stroke independently from its starting position. Therefore, the mean value of the positions of the actin filament in the attached state can be interpreted as the displacement generated by the power stroke.

This experimental setup was used to measure the power stroke displacement [95]. An interesting extension of the experiment was realized controlling the aline-ment of the myosin motor with respect to the actin filament. When the motor is oriented parallel to the actin filament, i.e. its tail is parallel to the actin fila-ment, the mean value increases to ~ 15 nm which is three times the mean value of randomly oriented motors [96].

3.2   The model dynamics in the experimental setup

In this section, I discuss the implementation of the numerical integration of the model dynamics introduced in Sections 2.3 and 2.4. Suitable boundary conditions are introduced in order to reproduce the laser trap setup (see Fig. 2.4). Finally, numerical results are compared to experimental data.

In the laser trap setup [7, 8, 97], the myosin head is linked to a fixed point by the neck domain while each extreme of the actin filament is linked to a polystyrene bead. The polystyrene beads are controlled by an optical tweezer.

The link between silica bead and the myosin head is modeled by a harmonic bond:

$$V_M(x) = k_M \left(x - x_{eq} \right)^2, \tag{3.1}$$

where k_M represents an effective stiffness.

The dynamics of F-actin in the trap is modeled as follows. Polystyrene beads are modeled as point–like particles rigidly connected to each other by the actin

Histogram of F-actin position in the bound state
(single numerical experiment)
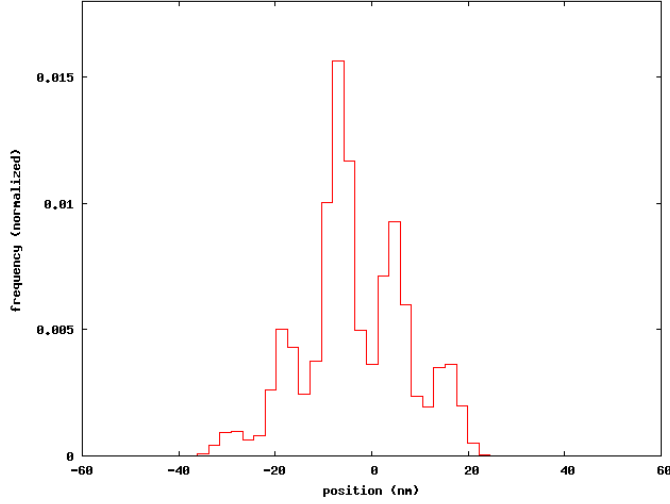
Figure 3.4: Histogram produced by a single numerical experiment with relative equilibrium position $\xi_{eq} = 0.3$ nm. The peaks correspond to the relative positions of the interaction potential minima.

filament, the mass of actin is neglected. The mass of polystyrene beads is several order of magnitude larger than the mass of myosin $(m_{PB}/m_M \simeq 10^7)$; consequently, inertial forces on the bead are taken into account. The laser trap bindings on each bead are described by an harmonic bond characterized by the laser trap stiffness, k_A. The motion of the actin–polystyrene complex is properly described by the underdamped Langevin equation with inertial force proportional to the mass of a polystyrene bead m_{PB}. The equations of motion are obtained by modifying Eq.(2.2) and Eq. (2.3) (see Section 2.3):

$$\gamma_M \, \dot{x} = -W_s'(\xi) - k_M(x - x_{eq}) + \eta_M \, , \tag{3.2}$$

$$2 \, m_{PB} \, \ddot{y} = -2 \, \gamma_{PB} \, \dot{y} + W_s'(\xi) - 2 \, k_A(y - y_{eq}) + \sqrt{2} \, \eta_{PB} \, , \tag{3.3}$$

where x and y are respectively the positions of myosin and the actin–polystyrene complex, $\xi = x - y$ is the relative position of the myosin domain with respect to the actin filament. W_s is the actin–myosin interaction potential. In the interactive state $s = 1$, W_s is the same introduced in the general model description in Section

67

2.3. Only the relative equilibrium position, $x_{eq} - y_{eq}$, is relevant to model dynamics. I fix $y_{eq} = 0$, and control x_{eq}. The noise term η_{PB} describes the thermal impulses on a single polystyrene bead:

$$\langle \eta_{PB}(t)\eta_{PB}(t+\tau)\rangle = 2\gamma_{PB}k_B T\,\delta(\tau).$$

Histogram of the F-actin position in the bound state
### (sum of 10 experiments with different x_{eq})
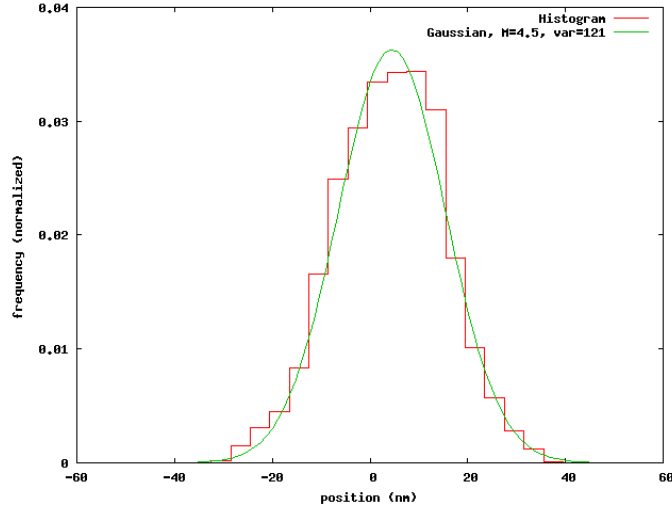
Figure 3.5: Histogram computed by summing the histograms of 10 numerical experiments with different equilibrium position (red line). The equilibrium positions are uniformly distributed within the interval of a period of the interaction potential (12 nm). The Gaussian fit is superposed to the histogram (green line); the mean value obtained by the fit is 4.5 nm.

In the laser trap assay, the equilibrium position of the myosin domain cannot be controlled. Further, the actin filament is allowed to rotate around its symmetry axis, i.e. the relative equilibrium position changes during the experiment. The helical structure of actin is responsible for the periodicity of docking sites available to the myosin head. When actin is allowed to rotate, it is reasonable to assume that nearly every actin unit is available to the myosin.

In the model, the periodic potential holes of the interaction potential W_1 represent the docking sites; the period corresponds to the distance between two adjacent
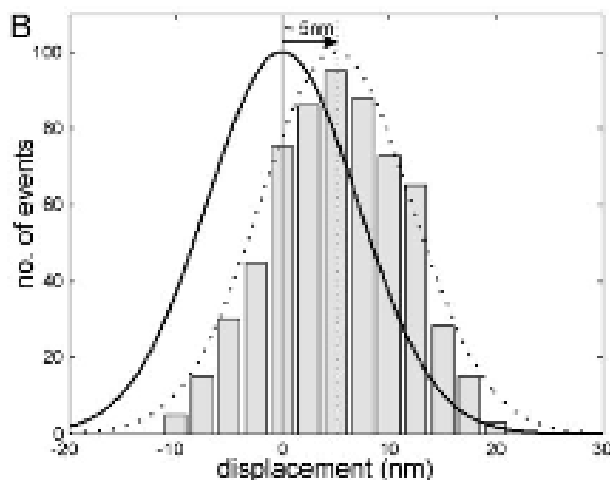
Figure 3.6: A typical histogram found with the single motor experiment. Reproduced from [95].

sites. I account for the changing relative equilibrium position realizing several numerical experiments with different myosin equilibrium positions.

The resulting F-actin dynamics in the bound state produces a histogram with several peaks which seem to be enveloped in a gaussian–like distribution function (see Fig. 3.4 and Fig. 3.5), with the maxima in correspondence to the local minima of the interaction potential energy. The sum of these histograms with different equilibrium positions reproduces the experimental histogram (see Fig. 3.5). The numerical result is in good agreement with experiment (see Fig. 3.3). The mean value of the numerical histogram is 4.5 nm, while the mean value of experimental histograms varies for different techniques and setups: $3.3 - 8$ nm (see Tab. 3.1). The distribution is roughly Gaussian. The shift of the histogram is related to the asymmetric nature of the interaction potential and the localized transition zones. The numerical integration of the single motor system is in agreement with experimental results. The parameters determining the potential energy function and the shape of transition zones are supposed to be reasonable at least in order of magnitude and are held fixed for all further integrations (see Tab. 2.2).

$k_{LT}(pN/nm)$	k_M (pN/nm)	$P_{W_1}(nm)$	τ_α (ns)	τ_β (ns)	$T_{tot}(s)$
0.02	0.5	12	120	90	5

Table 3.2: Parameters of the single motor setup. The experiment was repeated with different values of ξ_{eq}. The parameters of the thermal bath are listed in Tab. 2.1 and characteristics of the interaction potential and the localized transition zones are found in Tab. 2.2.

## 3.3 A myofilament pair as a multi–motor system

The single motor model is now extended to the dynamics of a couple of thin and thick filament. In striated muscles, the thick filament is made up of hundreds (~ 200 to 300) of myosin II motors, i.e. $\sim 100 - 150$ double headed motor domains, connected to the same backbone [28]. Inside the sarcomere, thick filaments have a symmetric structure with respect to the M-line. They have two distinct zones where myosin domains protrude from the filament (active zones), these zones are separated by a small bare zone in the middle of the filament. Two arrays of actin filaments are present, one on each side of the M-line. The F-actin array is fixed on the Z-disc and overlaps with the corresponding active zone of the myosin filament. The interaction between actin and myosin generates the sliding dynamics of the actin array towards the M-line (see Fig. 3.7). To model the dynamics of a single filament pair, a half thick filament is considered to interact with the thin filament. The number of double head domains involved reduces to $\sim 50 - 75$.

As of today, the role of the double head configuration is not well understood. The motor model introduced in Section 2.3 is employed to describe the action of a double head domain. This assumption find some justifications in the results of the single motor experiment, where the measured dynamics did not differ qualitatively when using the myosin double–head domain, HMM, or the single-head domain, S1 (see Section 3.1).

In the collective model, all the motor domains on the thick filament interact with the same actin filament. The actin filament is treated as a rigid massless support, endowed with a periodic interaction potential (see Section 2.3), harmonically

linked to a fixed point. Hence its dynamics admits stationary states. I suppose the backbone of the thick filament to be rigid, and the domains linked harmonically to it. These bindings are identical for all domains, they represent the neck domain. The inertia of myosin heads is neglected.

The equilibrium positions of the myosin motors are placed at equal distances on the thick filament. They are determined by the equilibrium position of the first motor, x_0^{eq} and the distance between two adjacent equilibrium positions, L: $x_i^{eq} = x_0^{eq} + i\,L$. The chemical transition of each head occurs under the same conditions as in the single–motor model (see Sections 2.4 and 2.5.3), independently of the state of other myosin domains. The interaction force between each active domain and the thin filament is completely determined by the chemical state of the domain and its relative position with respect to the thin filament. The myosin domains do not interact directly with each other, but their dynamics depend on the position of the same actin filament.

3.3.1   The unbounded filament

Model of a filament pair with unbounded F–actin
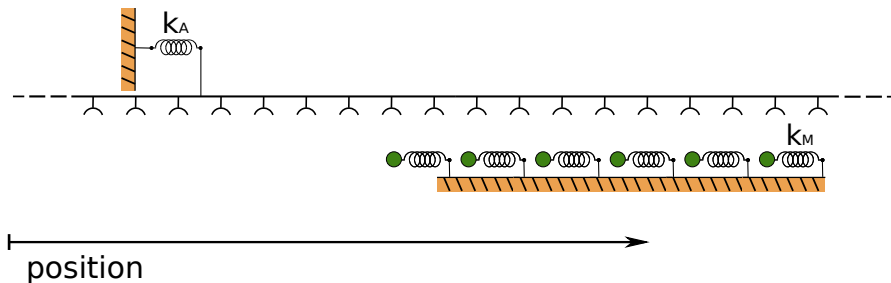
Figure 3.7: Schematic representation of a filament pair as a collective system of single motors. The myosin motors are represented by green circles, they are linked harmonically to a rigid backbone which is fixed in space. The stiffness of these links is given by k_M and the equilibrium positions of the motors are located at equal distances. All motors interact with the same actin filament: docking sites are located at equal distances on the rigid filament, the filament is harmonically linked a wall with stiffness k_A. The actin filament is unbounded, i.e. during the dynamics, the thick filament will always overlap entirely with the F-actin.

To study some elementary properties of the collective system we first consider

an unbounded actin filament. This guarantees that all myosin domains overlap with actin. The dynamics of the whole system is described by a finite number N of myosin domains and the actin filament:

$$\gamma_M \, \dot{x}_i = -k_M \left(x_i - x_i^{eq} \right) - W_s'(x_i - y) + \eta_i, \tag{3.4}$$

$$\gamma_A \, \dot{y} = -k_A \left(y - y^{eq} \right) + \sum_i^N W_s'(x_i - y) + \eta_A, \tag{3.5}$$

where γ is the Stokes' friction cefficient, k_M is the elastic stiffness of the neck domain and η represents the Gaussian white noise. W_s is the interaction potential relative to the chemical state $s = 1, 2$ of each myosin domain: interactive (1) and non-interactive (2) (see Section 2.3). The resulting force exerted by all the myosin heads on actin is the sum over the interaction with the single myosin heads, $\sum_i^N W_s'(x_i - y)$. Wether or not the interaction potential contributes to the dynamics depends on the chemical state of the myosin. This system is one–dimensional in space and has (N+1) degrees of freedom.

k_{LT} (pN/nm)	k_M (pN/nm)	L (nm)	P_{W_1} (nm)	N_M	τ_α (ns)	τ_β (ns)	T_{tot} (s)
0.1	0.5	14.3	12	50	30	10	5

Table 3.3: Parameters of the unbounded filament setup.The unbounded filament is taken under exam for different values of some of these parameters. The parameters which differ from the list above are specified in the text (parameters refer to Sections 3.3.1, 3.3.2 and 3.3.3).

I fix the parameters of the dynamics governed by the thermic bath, $k_B T = 4$ pNnm, $\gamma_M = 0.1$ pg μs^{-1} and $\gamma_A = 5$ pg μs^{-1}. Then, I set the stiffness of the external bond on the actin filament to be $k_A = 0.1$ pN/nm. This stiffness corresponds to the external stiffness of an experimental setup that will be introduced in the next section. The system is studied for different values of the following parameters: the transition times $(\tau_\alpha, \tau_\beta)$, the number of myosin domains (N_M) and their distance (L), and the period of actin docking sites (P_{W_1}).

3.3.2 Transition times

Mean force on F-actin as a function of the transition time τ_β
$(\tau_\alpha = 30$ ns$)$
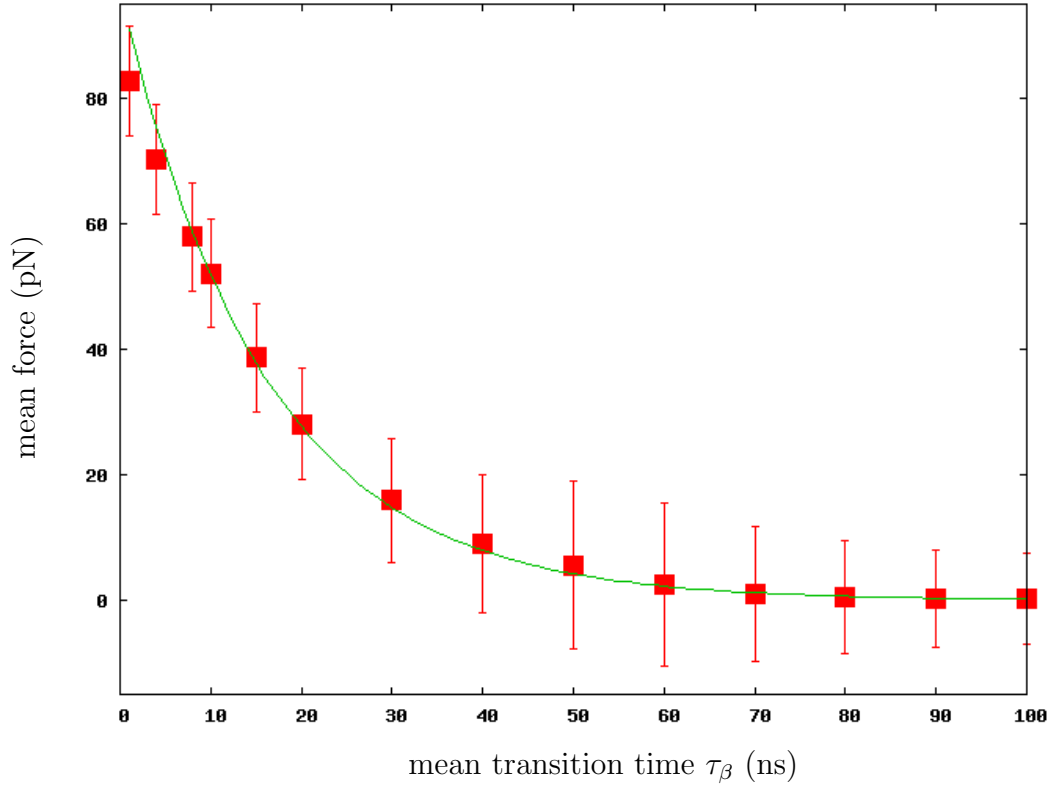
Figure 3.8: The mean force exerted by the thick filament on the F-actin is traced for different values of the transition time τ_β and fixed $\tau_\alpha = 30$ ns. The force is produced by 50 myosin heads which are linked to the thick filament and interact with the same thin filament (red squares). The behavior of the force as a function of transition time τ_β is fitted with an exponential function $\propto \exp(-\tau_\beta/\tau_0)$, where $\tau_0 = 16\,\mu$s is calculated by the fit of data (green line). For model parameters see Tab. 3.3.

To study the dependence of the chemical transition properties, the transition zones are kept fixed (see Tab. 2.2), while transition times are varied. The model dynamics is integrated for different values of mean transition times $\in [1, 100]$ ns, I varied separately τ_β for fixed τ_α (30 ns) and vice versa τ_α for fixed τ_β (10 ns). The mean displacement is proportional to the force exerted by the thick filament; the

Mean force on F-actin as a function of the transition time τ_α
$(\tau_\beta = 10$ ns$)$
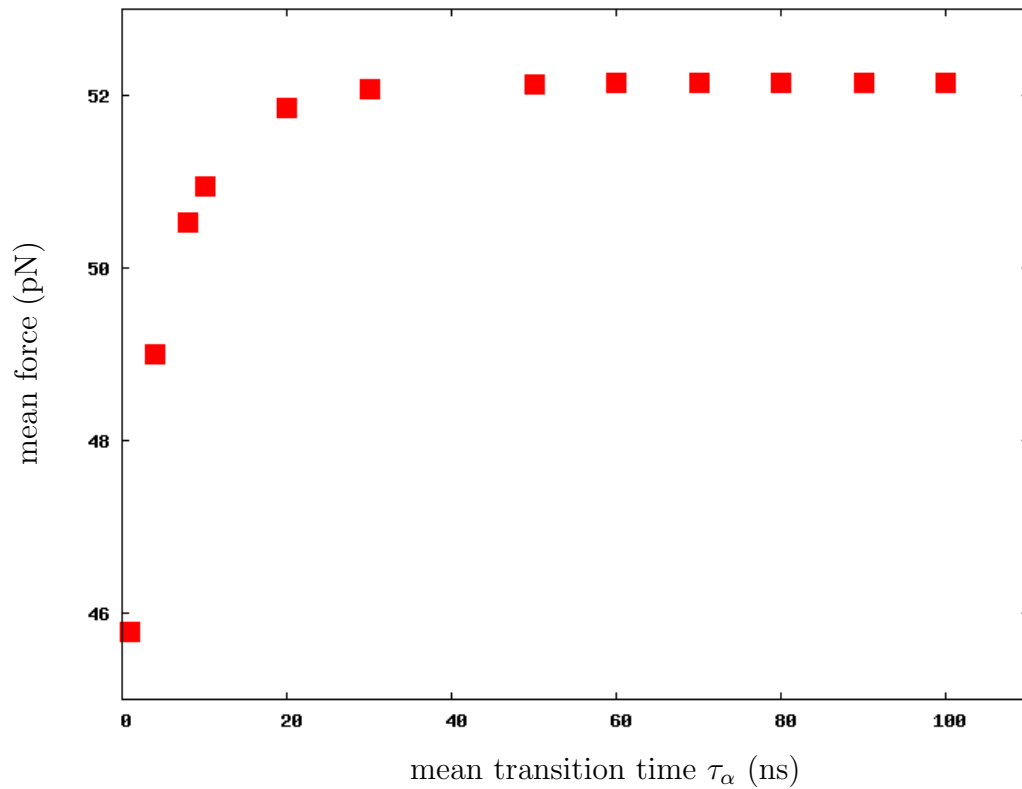
Figure 3.9: Mean force on the F-actin exerted by the thick filament as a function of the transition time τ_α. is measured for varying mean transition times τ_α. For increasing τ_α, the force approaches rapidly a constant maximum; at $\tau_\alpha = 30$ ns, the force reaches almost its maximum. Data are obtained for constant $\tau_\beta = 10$ ns. For the other model parameter see Tab. 3.3.

forces shown in the following figures are obtained from the mean displacement of the F-actin.

In Figure 3.8 it is shown that the mean force decreases exponentially with the transition time τ_β. This result is reasonable: with increasing τ_β, the transition rate $(2 \rightarrow 1)$ decreases and the dynamics spend more time in state 2, the non interacting state; ATP–cycling slows down and less force is generated.

Tension on the thick filament for different τ_β
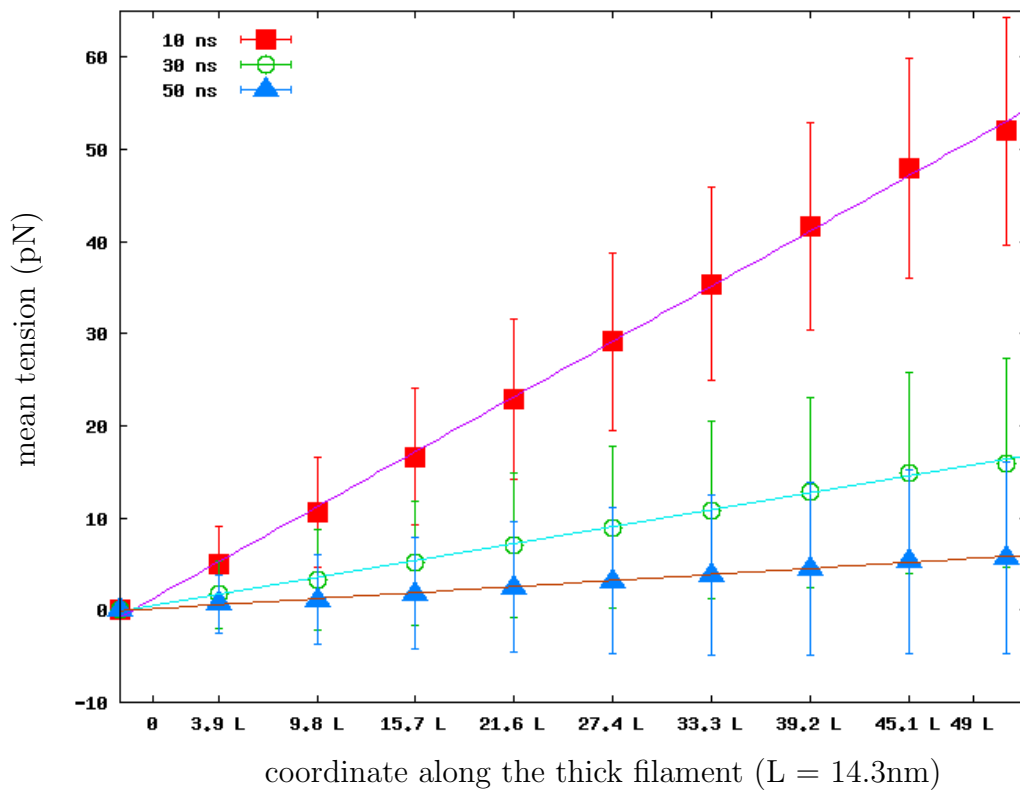
Figure 3.10: The mean tension increases along the thick filament, it is a linear function of the coordinate along the thick filament. The slope varies for different values of τ_β (see key in figure). 50 myosin heads are placed on the thick filament at equal distances L = 14.3 nm; the coordinate along the thick filament is given in units of L. The full lines are linear fits of the data, the resulting slope represents the tension per length unit (from top to bottom: 1.01 pN/L, 0.31 pN/L and 0.11 pN/L), while the force per myosin head is given by the slope times L, where L is the distance between adjacent heads. For model parameters see Tab. 3.3.

The mean force increases with increasing τ_α in an initial interval ($\tau_\alpha \leq 30$ ns)

and reaches rapidly a constant maximum (see Fig. 3.9). The total variation of force is very small. The characteristic value of oscillation of the myosin head in the potential minimum is estimated by $\gamma_M/(W_1''(\xi_{\min})+k_m) \sim 65$ ns; it is comparable in order of magnitude to the initial interval ($\tau_\alpha \leq 30$ ns) and I suggest that for small transition times τ_α, the dynamics in state 1 do not last long enough to allow for the myosin domain to reach the minimum in the potential hole. Hence, the force developed is smaller than for longer τ_{alpha}, when myosin reaches the minimum. I expect that for much longer permanences in state 1, i.e. much bigger τ_α, the displacement will decrease, because the long lasting bindings are expected to pull the dynamics up.

The mean tension increases linearly along the thick filament, this is shown in Fig. 3.11 for different values of τ_β. The myosin heads are distributed uniformly on the thick filament and hence, the mean tension depends linearly on the number of myosin heads N_M. The slope of the mean tension represents the mean tension per unit of the filament. The mean tension for single myosin head is given by slope times L, where L is the distance between adjacent heads. In the three cases in Figure 3.11, the mean tension for single motor are given by 1.01 pN, 0.31 pN and 0.11 pN respectively to the values of $\tau_\beta = 10$ ns, 30 ns and 50 ns.

The relative error of the mean tension is calculated for different values of τ_β (see Fig. 3.11). In general, the relative error of the sum of N independent stochastic variables is proportional to $N^{-\frac{1}{2}}$. The relative error of the mean tension is fitted with the function $x^{-\frac{1}{2}}$, where x is the position on the filament and is proportional to the number of contributing myosin heads. The fit well–describes the behavior for many motors.

In Fig. 3.12, the histogram of the F–actin position is shown for different values of τ_β. The histogram of the F–actin position is nearly Gaussian, i.e. the F–actin behaves like a harmonically constraint particle where the force exerted by the thick filament seems to be well described by an effective stiffness. With increasing mean position the width of the histogram decreases.

Relative error on mean tension along the thick filament for different
τ_β
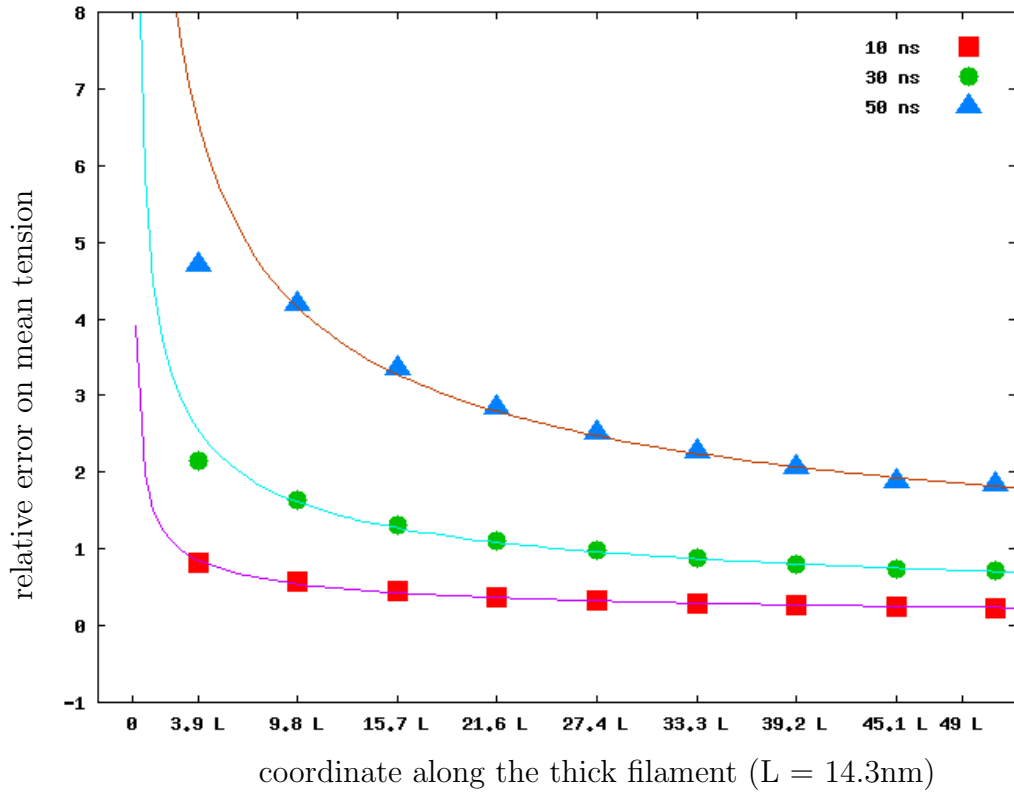
Figure 3.11: The relative error of mean tension decreases along the thick filament for different values of τ_β (see key in figure). The error is a function of the number of heads contributing to tension. The density of heads is uniform on the thick filament, hence the error can be expressed as a function of the coordinate along the thick filament x; it is expected to be proportional to $x^{-\frac{1}{2}}$, the full lines are fits of the data with this function. For model parameters see Tab. 3.3.

Histogram of the F-actin position for different values of τ_β
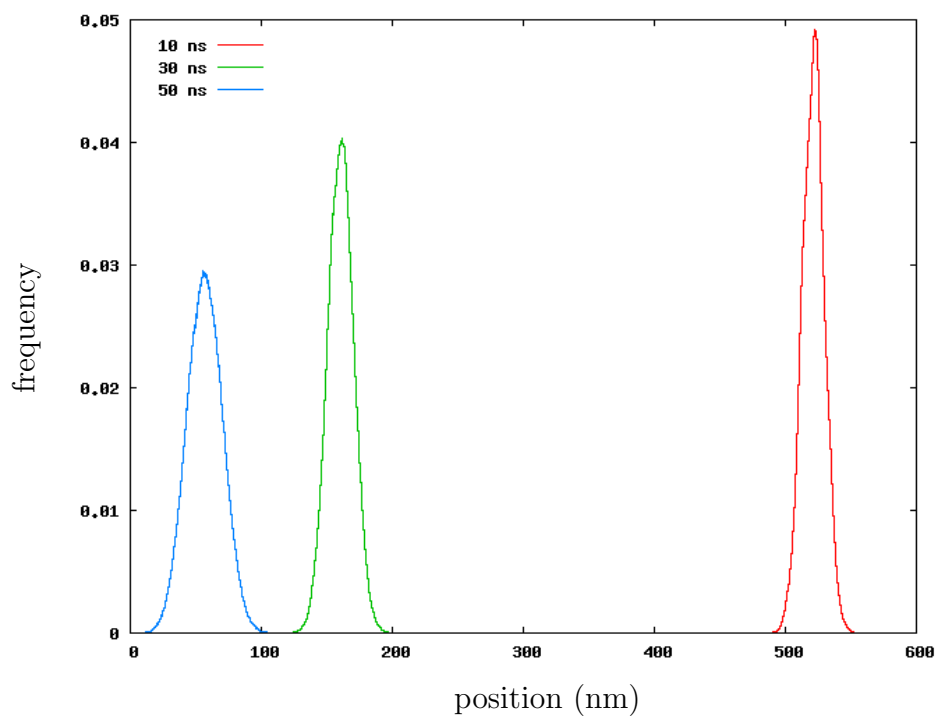
Figure 3.12: The histogram of the F-actin position is shown for constant $\tau_\alpha = 10$ ns and different values of $\tau_\beta \in [10, 50]$ ns. For decreasing τ_β the mean displacement of the F-actin and hence the force exerted by the myosin filament increases, the histogram is approaching a Gaussian function.

3.3.3 Structure of the thin and thick filaments

In the model, the intrinsic structure of the thin filament is determined by the period of the interaction potential W_1, while the thick filament structure is characterized by the distance between equilibrium position of the myosin heads.

Mean force on F–actin for different periods of the interaction potential W_1
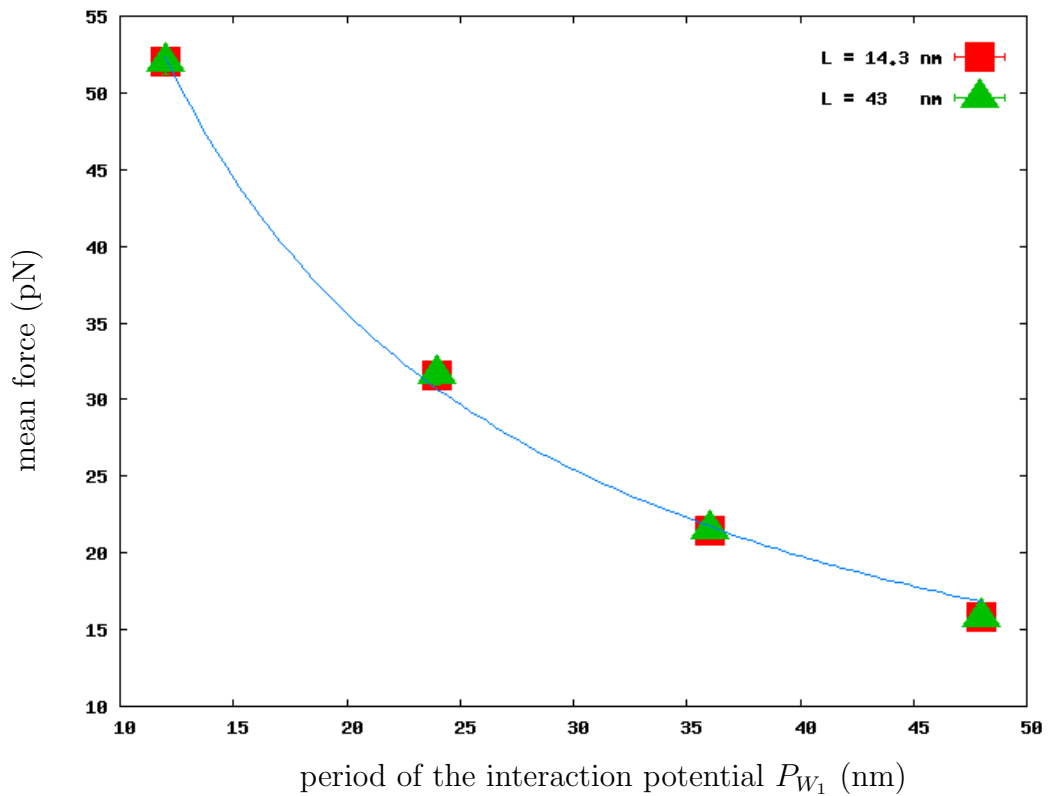
Figure 3.13: The mean force is shown as a function of the interaction potential period P_{W_1}. The force decreases with increasing P_{W_1}. Results are remarkably independent of the myosin domain spacing L (within the range explored). For model parameters see Tab 3.3.

In this paragraph, the mean force on actin and the tension in the myosin filament are computed for different periods of the interaction potential (P_{W_1}) and for different values for the myosin domain distance on the thick filament (L). The number of myosin domains for thick filament is constant; the length of each

filament is proportional to the distance between the domains: $L_{\text{thick filament}} = $ (number of domains) $\cdot L$.

The mean force is remarkably independent from the myosin domain spacing L (see Fig. 3.13). It is found that the mean force is proportional to $P_{W_1}^{-1}$. Since the period of docking sites is the inverse of docking site density ($P_{W_1}^{-1} \propto n_A$), the mean force is a linear function of the density of docking sites on the thin filament.

Histogram of F-actin position for different values of P_{W_1}
($L = 14.3$ nm)
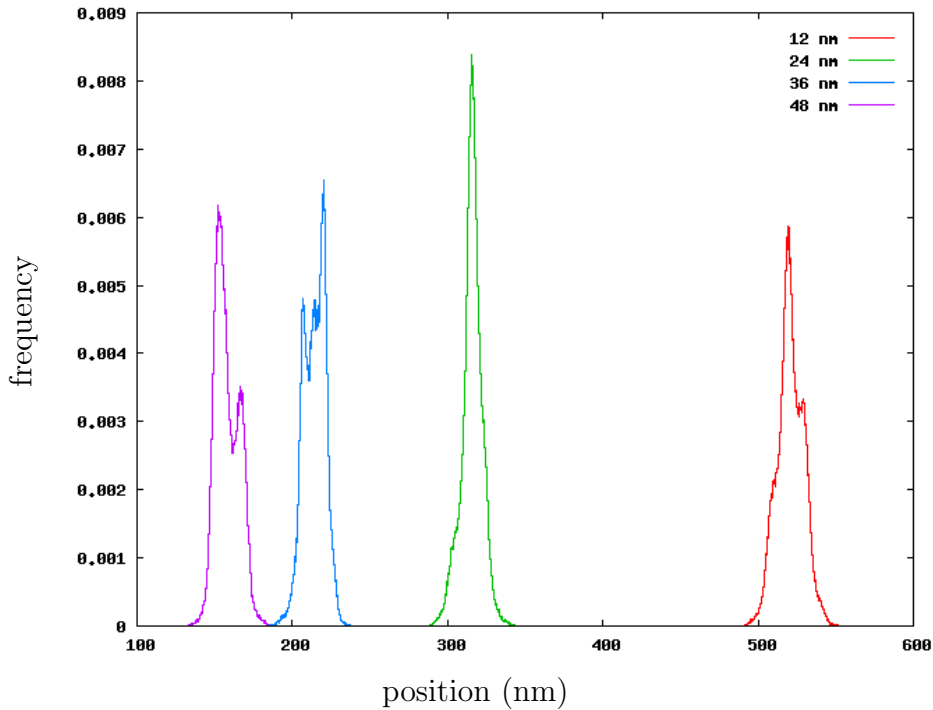
Figure 3.14: The histogram of the F-actin is traced for four different periods of P_{W_1}. In the case of $P_{W_1} = 12, 36, 48$ nm the histogram shows clearly multiple peaks, while for $P_{W_1} = 24$ nm the histogram has a single dominant peak, but is still asymmetric.

In Figure 3.14 and Figure 3.15 are shown the histograms of the F–actin position for different values of the interaction potential period P_{W_1} respectively for the model with myosin head distance equal to 14.3 nm and 43 nm. As it was shown in Figure 3.13, the mean values depend only on the period P_{W_1}. The qualitative dynamics behavior depends also on the distance between the myosin heads. For

Histogram of F-actin position for different values of P_{W_1}
($L = 43$ nm)
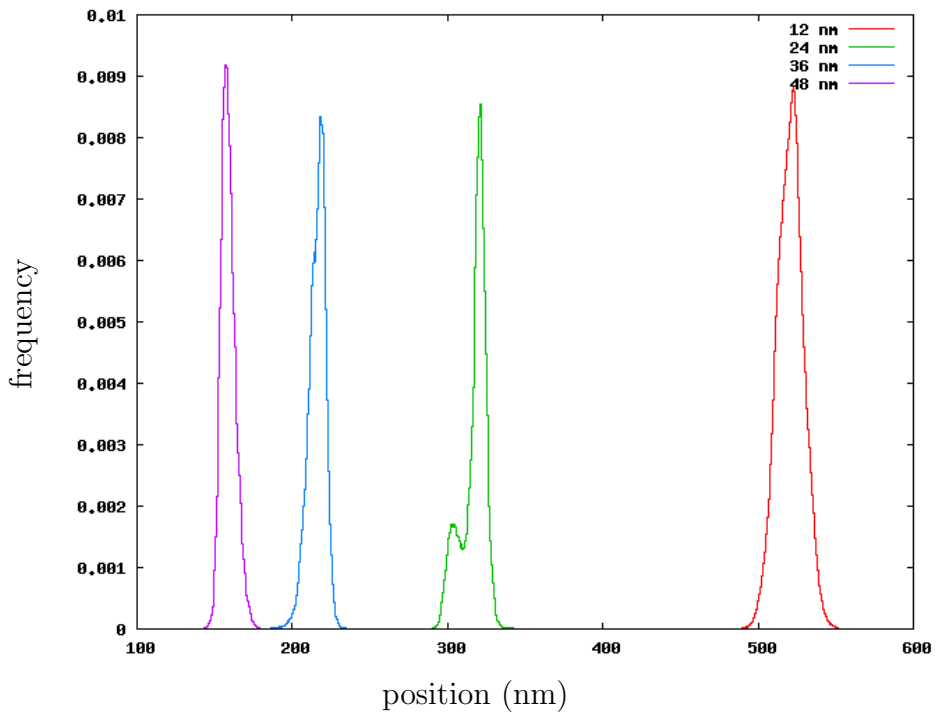
Figure 3.15: The histogram of the F-actin is traced for four different periods of P_{W_1}. Only in the case of $P_{W_1} = 24$ nm the histogram has two local maxima, while for the remaining periods P_{W_1} the shape approaches a symmetric distribution function.

$L = 14.3$ nm, the histogram shown multiple local maxima in the case of $P_{W_1} = 12, 24 and 48$ nm, while for $P_{W_1} = 24$ nm is observed a single peak, nevertheless, even in this case the histogram has a pronounced asymmetric shape (see Fig. 3.14). Contrary, for $L = 43$ nm, only in the case of $P_{W_1} = 24$ nm the histogram has two local maxima, otherwise the histograms have a single peak.

The interaction potential is invariant for net translations P_{W_1} of the relative position between the two filaments and it is nearly invariant for translations L. Indeed, when translating the thick filament about L with respect to the thin filament, the relative position of the heads at the border may give a different contribution to W_1. I suggest that for a certain configuration (L, P_{W_1}) exist a preferred relative position or metastable state. If there are suitable conditions of quasi invariance this state is replicated at the distance of invariance all along the filament. The external force does not allow to visit all this states and in the histogram the local maxima are observed consistent with the external constraints.

3.4 Model results vs. experiment

Scheme of experiment
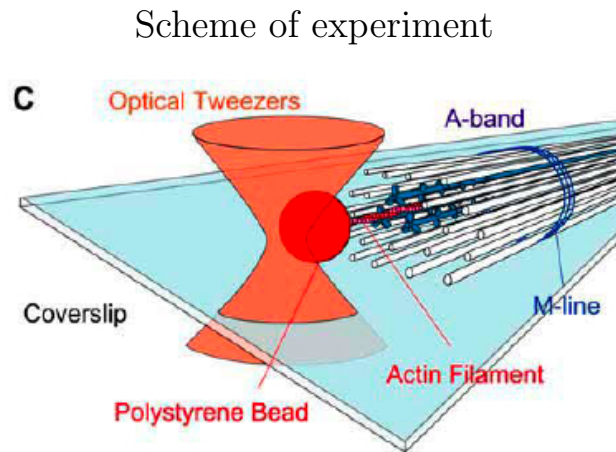
Figure 3.16: Schematic representation of the experimental setup. Reproduced from [98].

The experiment we refer to was realizeded by Suzuki and coworkers [98]; it was designed to fill the gap between single motor dynamics and sarcomere dynamics.

In this setup a bundle of thick filaments still attached to the M-disc is extracted from the sarcomere. This bundle is deposited onto a substrate (see Fig. 3.16). An actin filament is linked to a polystyrene bead at one end, and the bead is trapped in an optical tweezer. The optical tweezer can be moved, i.e. the position of the polystyrene bead is controlled. The actin filament is aligned with the bundle of thick filaments and its free end is brought into contact with the bundle of thick filaments (see Fig. 3.16). When the actin filament gets near to the bundle of thick filaments the actin–myosin interaction is enabled and the actin filament is pulled towards the M-disc. The actin filament reaches a stationary state in which the mean force exerted by the bundle is equal to the external mean force generated by the laser trap. Displacement and force on the actin filament are measured.

Suzuki et al. used two different techniques to measure the mean overlap – mean force relationship. In the first approach, they modify the stiffness of the laser trap several times during a single realization of experiment; different stationary states are obtained. The other approach consists in changing the equilibrium position of the laser trap during a single experiment in order to obtain several stationary states. Mean overlap and mean force are measured in each stationary state. The resulting mean overlap – mean force relationship obtained from a single realization of experiment is linear. The slope of the relationship differs with different realizations. The two approaches give the same result; it is not possible to distinguish them from the mean overlap – mean force relationship.

The experiment is realized using two different arrangements: in one case, the actin filament is pulled near the outer surface of the bundle, and in the second case, it is pulled near the center of the cross–section of the thick filament bundle (see Fig. 3.18). In the former experimental arrangement, a single class of overlap–force relationship is obtained (A and B in Fig. 3.17), while in the latter one, two different classes are found (C and D in Fig. 3.17): one with the slope comparable to the class found in the first case and one with a bigger slope (see Tab. 3.4).

The authors conjecture that the different behaviors are due to the number of thick filaments with which the actin filament interacts. The overlap–force relationship was found to have a bigger slope only in the former experimental arrangement, when pulled inside the bundle. In this case the F-actin interacts with one, two or three thick filaments, while it interacts with less than three thick filaments when
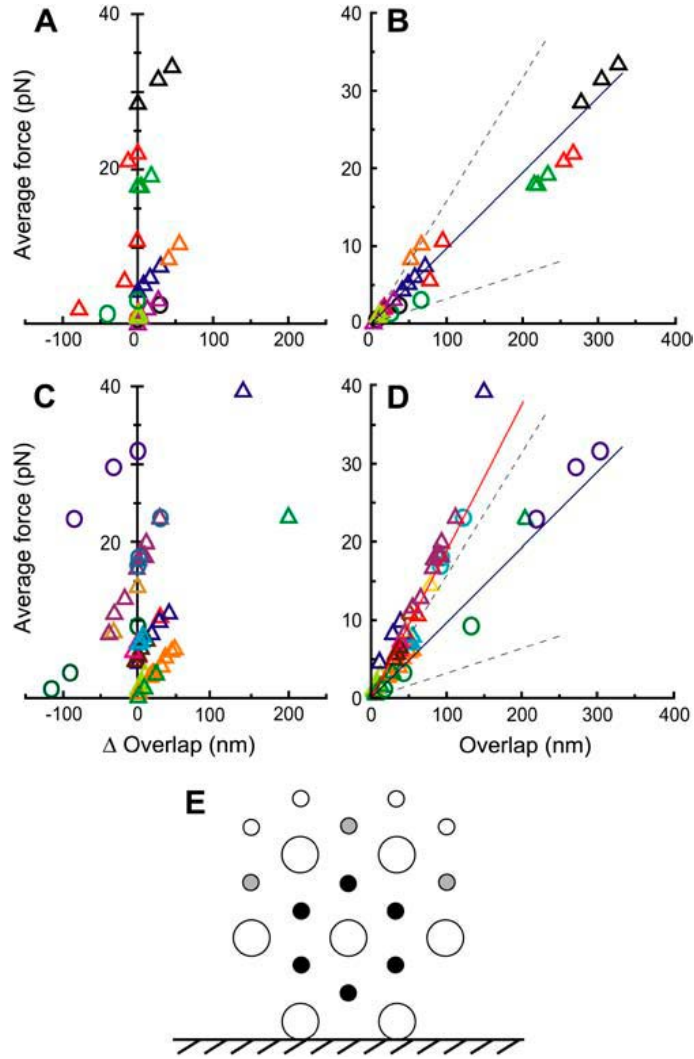
Figure 3.17: The four plots A to D show the force-overlap relationship obtained by varying the laser trap stiffness k_{load} or, equivalently, the equilibrium position of the laser trap y_{eq}. The two methods produce the same results. In E is shown a schematic cross-section of the filament lattice: the small circles represent the thin filaments, and the large circles represent the thick filaments. The experiment was repeated for the actin filament pulled near the outer surface of the bundle (small grey and white circles in E; corresponding plots: A and B) and near the center of the thick filament bundle cross-section (black circles in E; corresponding plots: C and D). Two different ranges of slope are found. Reproduced from [98].

	outside pN/nm	inside pN/nm
outer surface (see Fig. 3.20, left)	0.097 ± 0.032 (10)	—
central (see Fig. 3.20, right)	0.11 ± 0.028 (5)	0.19 ± 0.031 (8)

Table 3.4: The values are given as mean ± SE (standard error) with numbers of preparations, n, indicated in parentheses. Slopes were determined by the least–square method. The data were obtained by the interaction of an actin filament with the outer surface or the end–plane of the A–band, which was determined by microscopic observation during the experiments according to the geometry of the actin filament and the A–band. The data obtained for the end–plane of the A–band were classified into two types, i.e., outside or inside the thick filament lattice, according to the slope for the relationship of the average force versus overlap [98].

Schematic representation of the two different classes of experiment
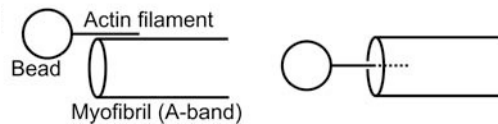

Figure 3.18: Schematic representation of the two classes of results; on the left F-actin is pulled inside the thick filament bundle and on the right F-actin is pulled by the thick filaments on the outer surface of the bundle.Reproduced from [98].

pulled on the outer surface, (see Fig. 3.17 E). Hence it is suggested that the interaction between the thin filament and three thick filaments produces a bigger slope in the force–overlap relationship than the interaction with less thick filaments.. The class of smaller slope, observed in both experimental arrangements, is thought to represent the average force per overlap for interaction of the actin filament with one and two thick filaments.

### Model of filament pair with bounded thin filament
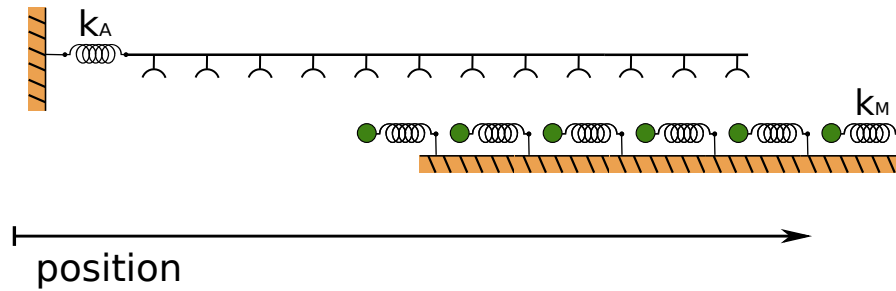
Figure 3.19: Many myosin heads are linked harmonically to a fixed rigid backbone with bond stiffness k_M. All myosin heads interact with the same actin filament. The actin filament is represented by a rigid massless support with docking sites at constant distance; it is linked to a wall by a harmonic bond (k_A).

To model the physiological system of filaments in a half-sarcomere, the finite length of F-actin should be considered. The actin-myosin interaction is allowed only in the overlap region. This implies an additional constraint on the interaction potential; the interaction exists only if the i-th myosin domain faces the actin filament, i.e. it lies within the overlap region of the two filaments.
To model the experimental setup exposed before in this section, the equations of motion of actin (3.4) and (3.5) are modified as follows:

$$\gamma_M \, \dot{x}_i = -k_M \left(x_i - x_i^{eq} \right) - W_s'(x_i - y) \Big|_{x_i \, \in \, overlap} + \eta_i, \tag{3.6}$$

$$\gamma_{PB} \, \dot{q} = -k_{LT} \left(y - y^{eq} \right) + \sum_i^N W_s'(x_i - y) \Big|_{x_i \, \in \, overlap} + \eta_{PB}, \tag{3.7}$$

The damping coefficient and the white Gaussian noise in (3.7) refers to the polystyrene bead and k_{LT} is the laser trap stiffness. Inertia forces can be neglected in compari-

son with the damping forces. This assumption differs from the one taken in Section 3.1: in fact, the mass of the polystyrene bead used in this experiment is several orders of magnitude smaller than those used in the single motor assay [8, 98].

k_M (pN/nm)	L (nm)	P_{W_1} (nm)	Δoverlap (nm)	N_M	N_A	τ_α (ns)	τ_β (ns)	T_{tot} (s)
0.5	14.3	12	50	60	126	10	10	5

Table 3.5: Parameters used to compute the filament pair with bounded thin filament. This model dynamics is employed to reproduce the experimental data of the filament assay [98]. Δoverlap indicates the overlap when myosin and actin are in their equilibrium positions with respect to the external bonds. The dynamics is computed for different values of the laser trap stiffness.

In the sarcomere, a single actin filament is able to interact with the myosin domains of three thick filaments. To model the effects of the three–dimensional arrangement of the filaments, I consider the number of docking sites and myosin head involved in the interaction between one thin filament with three thick filaments. The thick filaments are placed around the thin one with an angle of 120 degrees, the number of docking sites available to the myosin heads is three times that of the interaction with a single actin filament. I considered this by modifying the period of the interaction potential, $P_{W_1} = 12$ nm. The number of myosin heads has to be multiplied by three, consequently the distance between adjacent myosin heads reduces to $L = 14.3$ nm.

I simulate the first method, in which the trap stiffness is modified. The different stationary states are reproduced by computing several numerical experiments with different k_{LT}. The mean force – mean overlap relationship obtained in this manner is linear (see Fig.3.20) and for the model parameters listed in Tab. 3.5 the slope is equal to 0.07 pN/nm. This value is of the same order of magnitude but slightly smaller than that found experimentally (see Tab. 3.4)

The tension along the thick filament increases with the same rate in the different experiments (see Fig. 3.21), while the region of overlap in which the mean tension

Force overlap relationship
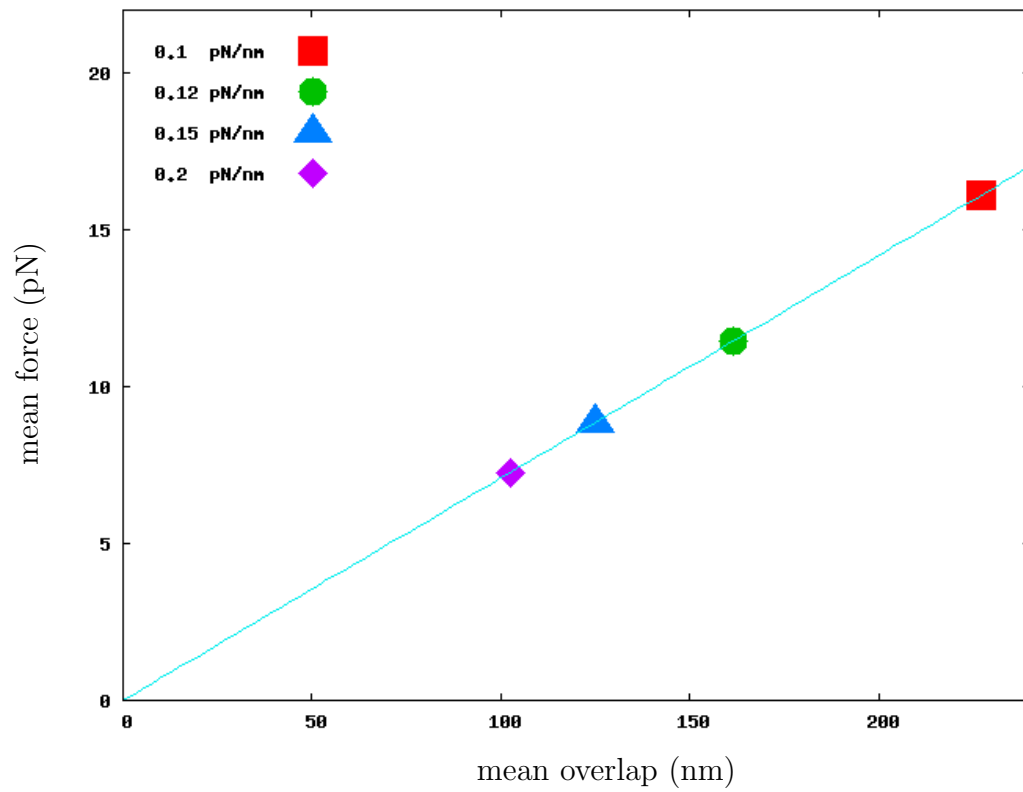
Figure 3.20: Mean force vs. mean overlap obtained by the finite-filament model. The relationship was obtained by repeating the numerical experiment for four different values of the laser trap stiffness k_{LT}. The slope of the fit is 0.07 pN/nm. For model parameters see Tab. 3.5.
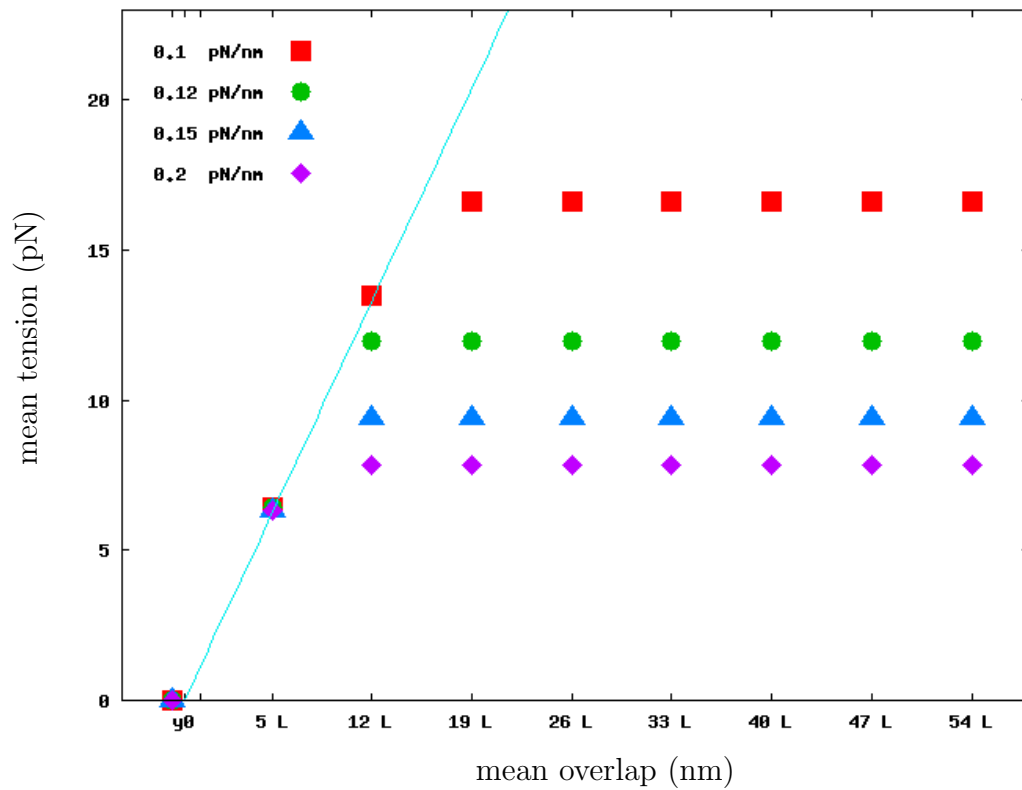
Figure 3.21: Mean tension along the myosin filament is represented. The tension increases linearly in the overlap region and is constant in the non-overlap regions. The full line represents the force–overlap relationship (cf. Fig. 3.20); for model parameters see Tab. 3.5.

increases varies for different values of k_{LT}. This rate is equal to the slope of the mean force – mean overlap relationship. Further, the tension in the bounded filament is generated in exactly the same way as the tension in the unbounded filament. Now, for a thick filament of constant length and constant number of myosin heads, the mean tension along the filament is determined by the total tension developed by the thick filament. Hence, the slope of the mean force – mean overlap relationship depends on the model parameters in the same way as the mean force discussed in the previous sections: it is a linear function of the density of docking sites and decreases exponentially with the increasing transition time τ_β (see Sections 3.3.2 and 3.3.3).

Chapter 4

Sarcomere dynamics

Up to now the attention was focused on the dynamics of single motors and collective systems in tetanus conditions, i.e. in condition of complete activation. This chapter has two aims: 1) to extend the two–state model to a time–varying stimulation and 2) to scale it up to the half sarcomere scale.

4.1   The extended filament model

Activation is a collective property of the system. Therefore, the filament level is the smallest level at which it makes sense to introduce the regulatory mechanism of muscle contraction. I introduce an extension of the dynamical model discussed in detail in Chapter 2 in the case of the collective collective system representing a pair of thin and thick filaments (see Section 3.3 Fig. 3.19).

Two hypotheses underly this model: 1) the acto–myosin interaction is possible only in correspondence to an activated actin site; 2) the number of activated sites varies in time, but is statistically uniform along the actin filament.
In the case of calcium activation these hypotheses correspond to the following assumptions on the molecular scale: 1) the docking site is available to the myosin head if the corresponding troponin bond binds calcium; 2) the concentration of calcium ions may vary in time, but is uniform along the actin filament.

Under tetanus conditions, the docking sites are spaced uniformly, the distance between docking sites correspond to the period of the interaction potential W_1.

To allow for a variable stimulus, two different local behaviors of W_1 are needed in order to represent the activated and the non-activated docking site respectively. An activated docking site is represented by the potential hole, while a non-activated docking site has a flat potential, i.e., there is no interaction corresponding to this site. Both elements have the length of a period.
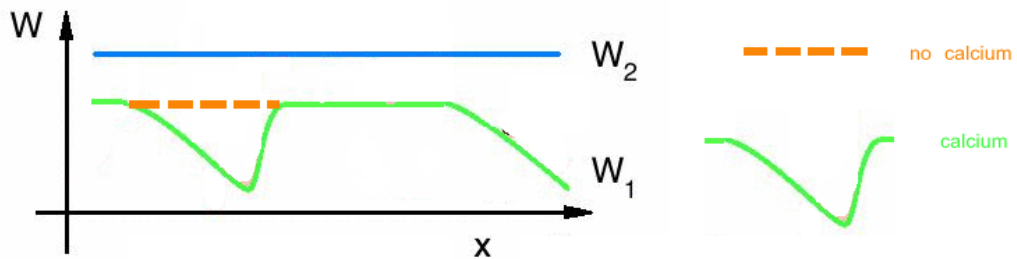

Figure 4.1: Schematic representation of the modified interaction potential. An activated docking site on the thin filament is represented by a potential hole in the interaction potential W_1, while a flat potential tract (plateau) corresponds to a non–activated site.

When including activation in the model, the interaction is governed by a modified potential $\widetilde{W}_1$. This interaction potential is made by a series of plateaus and holes that alternate randomly. Consequently, the potential energy is determined by extracting randomly a sequence of the two states: activated (1) and non-activated (0). The distribution of the sites along the thin filament has uniform probability. In the case of calcium-activation, the probability of extracting an activated binding site is assumed to be proportional to the calcium concentration in the sarcomere or in the *in vitro* environment of the system.

The system is described by (N+1) stochastic differential equations similar to the equations of motion in tetanized condition (see Section 3.4, Eq. (3.6) and Eq. (3.7)), where N is the number of myosin domains:

$$\gamma_M \, \dot{x}_i \;\; = \;\; -k_M \left(x_i - x_i^{eq} \right) - \left. \widetilde{W}_s'(x_i - y) \right|_{x_i \in overlap} + \eta_i,$$

$$\gamma_A \, \dot{y} \;\; = \;\; -k_A \left(y - y_{eq} \right) + \sum_i^N \left. \widetilde{W}_s'(x_i - y) \right|_{x_i \in overlap} + \eta_A \qquad (4.1)$$

$$\text{with} \qquad i = 1, .., N$$

The transition β, from state 1 to state 2, is inhibited for non-activated docking sites (plateau). This has no effect on the dynamics, in the plateau region both states do not produces force. Suppressing transitions avoids the system to cycle chemically without doing mechanical work.

No details on the molecular mechanism are specified leading to the activation or disactivation of docking sites. This implies that even if the model was designed with the calcium-induced regulation mechanism in mind, it may be easily extended to allow for ADP-regulation.

4.2 The partially activated filament

The dynamics of a partial activated filament pair is studied. In this case the activation rate is taken 0.5. The aim is to study the response of the dynamics with the modified interaction potential. In Equation 4.1 the dynamics depend on the modified interaction potential in the overlap zone, i.e. changes in the overlap zone are important for the dynamics. To uncouple the two phenomena, the activation and the overlap, I choose the thin filament to be much longer than the thick filament. This condition guarantees that the thick filament overlaps entirely with the thin filament during the dynamics.

Numerical experiments were realized with transition rates $\tau_\alpha = 30$ ns and $\tau_\beta = 10$ ns. The thick filament is composed of 60 active domains spaced by 14.3 nm, totalling 843.7 nm length. The period of docking sites on the thin filament is 12 nm. The thin filament is bounded to 500 docking sites, i.e. it is 6000 nm long, significantly longer than the thick filament. The thin filament has a harmonic bond to a fixed point, its equilibrium position y_{eq} is chosen so that the myosin filament

F-actin dynamics at 50% activation rate
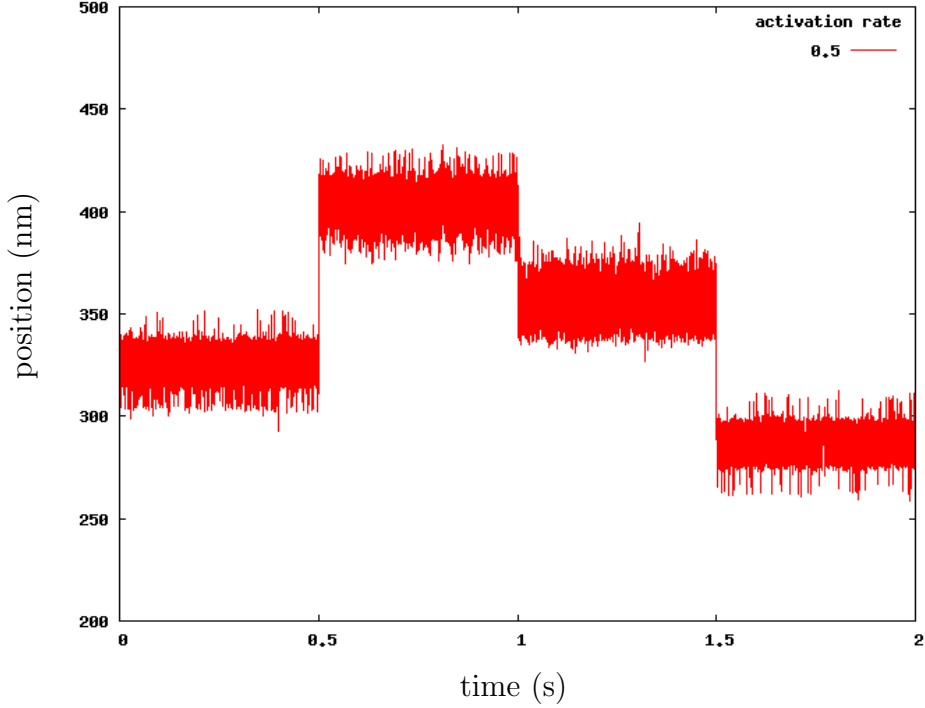
Figure 4.2: The dynamics is integrated for four different realizations of the activation sequence, i.e. for four different realizations of the interaction potential $\widetilde{W}_1$, each lasting for 0.5 s. The mean position of the F-actin differs for each realization. Stochastic oscillations about the mean position are observed for each segment. The mean position is proportional to the mean force applied externally and hence to the force produced by the motors.

is located at the middle of the actin filament $\xi_0^{eq} = x_0^{eq} - y_{eq} \simeq 3000$ nm. This condition guarantees complete overlap of the thick filament to the thin filament for the whole duration of dynamics, likewise the unbounded filament setup (see Section 3.3.1).

The activation sequence determines the interaction potential $\widetilde{W}_1$ in Eq. 4.1. It is generated by an extraction of 500 *on* and *off*–states with a certain fixed probability, where 500 is the number of total docking sites on the thin filament under exam. The response of the system to different activation sequences extracted with the same *a priori* probability is tested. The single experiment has a duration of 2 s, while the activation sequences are updated every 0.5 s. Each interval of 0.5

Total tension
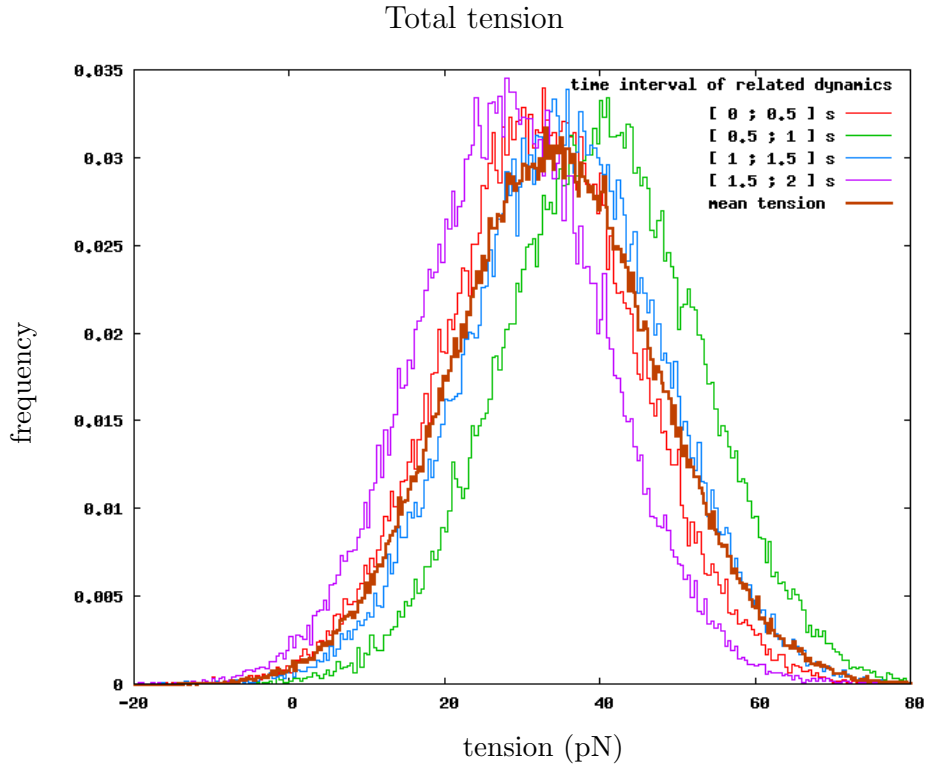
Figure 4.3: The histogram is shown of the tension measured on the right extreme, generated by all the myosin heads; the different histograms correspond to the four cases of the dynamics mentioned above; the large dark line (brown) shows the average tension of these four cases. The tension is sensible to the single realization of activation, it differs from segment to segment.

s with constant activation will be called a *segment*.

Within each segment, the F-actin reaches its stationary state quickly. In this state stochastic oscillations about a mean position are observed. The mean position varies significantly for different realizations of the activation sequences, it is proportional to the mean force applied externally on the thin filament. Hence the mean position is related to the force produced by the motors, .i.e. that the force developed by the actin–myosin interaction depends on the particular realization of the activation sequence.

In each segment, the total tension developed by the motors on the thick filament oscillates about a mean value. As expected from the kinetics (see Fig. 4.2), the mean value varies in the four different segments of the dynamics, it is comprised

in the interval [28 : 42] pN (see Fig. 4.3 and Fig. 4.4).

In Figures 4.3, the histogram of the total tension measured on the thick filament is shown for the four different segments. The histograms are shifted about the difference in mean value, while their shape does not vary significantly for different realizations of the activation sequences.

Mean tension along myosin filament

position on myosin filament (L = 14.3 nm)
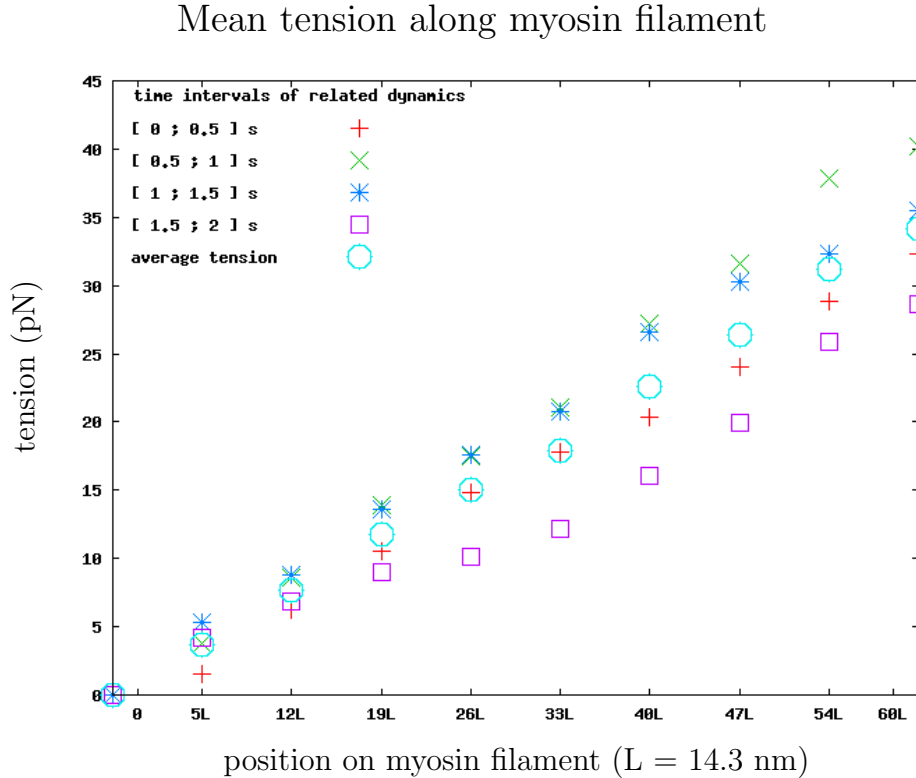
Figure 4.4: The average of the mean tension over the four realizations has a linear behavior along the myosin filament (azure circles). The mean tension corresponding to a single realization may not be linear, nonlinearities indicate variations in the density of activated docking sites on the facing thin–filament (e.g. purple squares).

The mean tension along the myosin filament does not have the linear behavior we found for the filament under tetanus conditions (see Section 3.3, Fig. 3.11). The nonlinearities are due to variations in the distribution of activated docking sites. In Figure 4.4, the tension corresponding to the segment [1.5; 2] s does not increase significantly between 19 L and 33 L on the thick filament. Within this interval $(x_i^{eq} \in [19\,L; 33\,L])$, the myosin heads do not contribute to the mean tension, i.e. they not produce mean force. I suggest that they face a portion of the thin filament

with very few active docking sites, i.e. with a big distance Δ between adjacent docking sites $\Delta >> P_{W_1}$. The average of the mean tension calculated over the four segments behaves roughly linear (circles in Fig. 4.4).

Histograms of the F-actin position
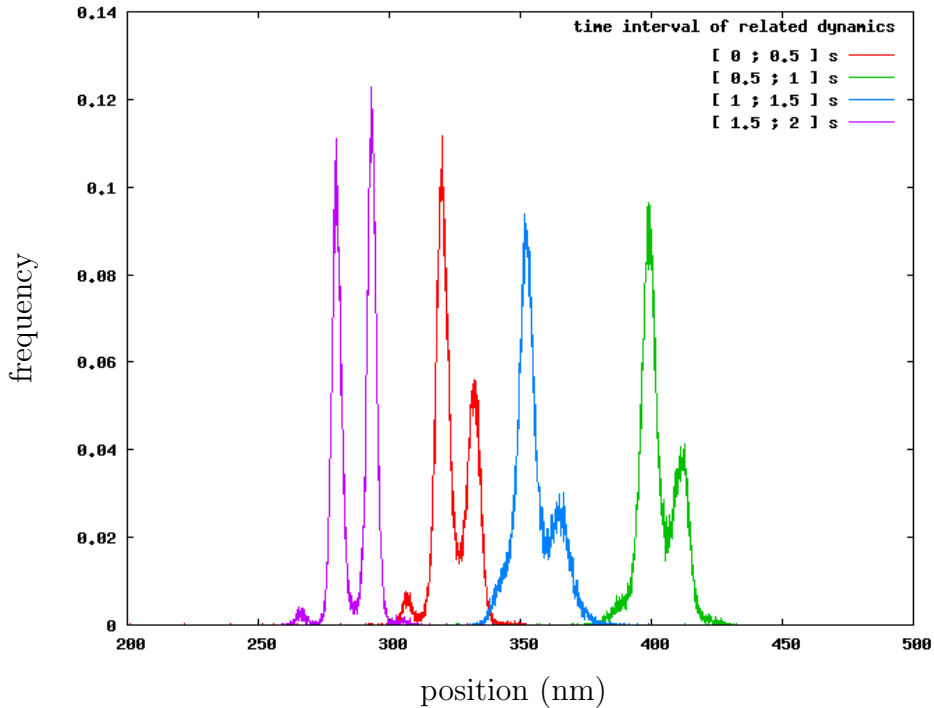
Figure 4.5: The four different histograms of the F-actin position are computed for the *segments* of the dynamics with different realization of the activation sequence (see key in figure).

Another aspect of the dynamics can be observed when looking at the histogram of the F-actin position. The histogram of each segment shows several peaks. The distance between the local maxima is of the same order in all four cases (~ 14 nm). These local maxima can be interpreted as a metastable states of the system. In this framework, the transition rate between the metastable states is a function of the difference in frequency between the maximum and the minimum of the histogram. When looking at the dynamics of the filament (see Fig. 4.2), these different states are observable only for the segment $[1.5; 2]s$, otherwise the transition between the two local maxima occurs too fast.

The local maxima were also observed for the tetanus (see Section 3.3.3, Fig. 3.14 and Fig. 3.15). It was shown that this multi–peak behavior arises for certain values of the distance between myosin heads on the thick filament L, and of the period P_{W_1}. In that case, peaks are less separated, i.e. the metastable states have smaller lifetimes than in the activated dynamics (see Fig. 4.5). In the tetanus, the interaction potential is invariant for the translation about multiples of L and of P_{W_1} respectively. The external constraint on the thin filament is modified by these translations, and it is expected that the multiple peaks are enveloped in by a single peak function due to the external elastic bond.

In the case of partial activation the interaction potential is not any more invariant for discrete tranlations. For translations about L there is a *quasi* invariance because the variation is limited to the interaction conditions at the border of the thick filament. In the case mentioned above the distance between local maxima is ~ 14 nm, while $L = 14.3$ nm.

I suggest that the metastable states are due to configurations of actin and myosin positions in which force production if favored. This advantageous configuration may for example consist of many motors which oscillates about the position of a docking site and hence are encouraged to undergo chemical transitions. Neglecting effects on the border of the thick filament, the advantageous configuration is invariant for translations about L, and consequently metastable states generated in this way are found at nearly constant distances ($\sim L$), the metastable states differ for the effect of external forces and the non invariant contribution to force generation at the border of thick filaments.

4.2.1 The activation sequence

To model the regulation mechanism of muscle contraction, I introduced in Section 4.1 a switch mechanism for the docking sites. The state (*on/off*) of each switch, i.e. each docking site, is extracted randomly with an *a priori* probability p. The extraction is repeated for every site with constant independent probability. The resulting series of events is called the activation sequence and determines the switch–states related to the docking sites on the thin filament and hence the interaction potential $\widetilde{W}_1$.

Binomial distribution function with n=70
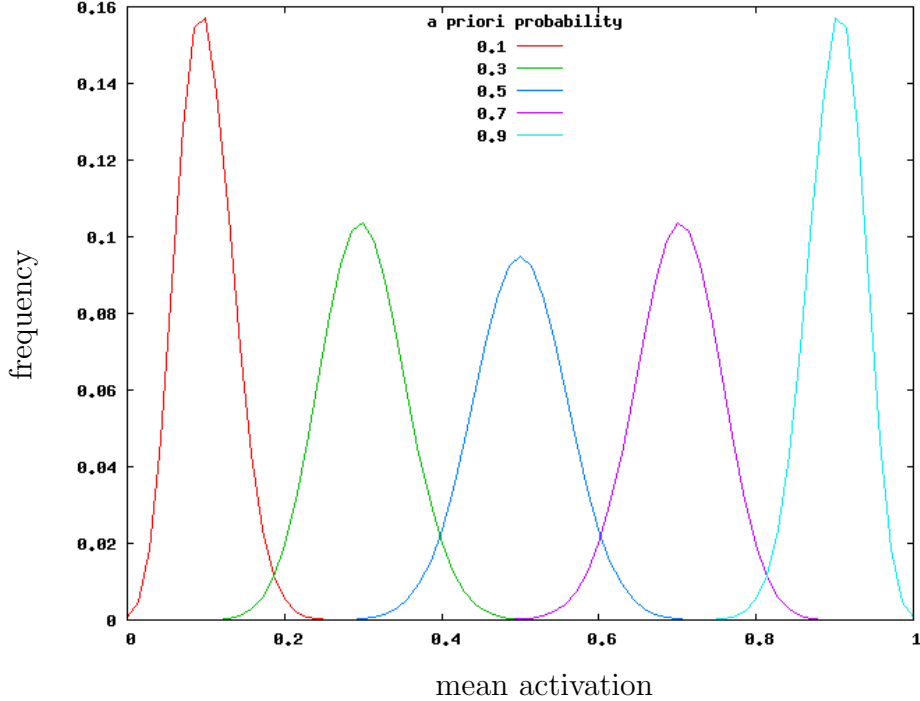
Figure 4.6: The function $P(n, k)$ (see Eq. (4.2)) is shown for n=70 and different values of the *a priori* activation probability p. Each distribution function is computed in 71 points, $k = 0, 1, .., 70$; the plot is obtained by connection these points with a line.

The activation sequence is a series of independent events with constant probability, the number of events is given by the total number of docking sites on the thin filament, while a successful event indicates an activated site. If p is the probability *a priori* to extract the *on*–state, then the probability to obtain an activation sequence of n total elements and k activated sites is given by the binomial distribution:

$$P(n, k) = \begin{pmatrix} n \\ k \end{pmatrix} p^k (1 - p)^{(n-k)}. \tag{4.2}$$

The distribution function of the mean activation is shown for different values of the *a priori* (or activation) probability p in the case of 70 docking sites (n=70; see Fig. 4.6). In the case discussed in Section 4.2, a thick filament with 60 myosin heads at equal distances of $L = 14.3$ nm faces to 70 docking sites on the thin filament

with distance between the docking sites equal to 12 nm. In the case of $p = 0.5$ the mean value of activated sites is 35 and the variance 17.5 (35 ± 4.2 activated sites). The different realizations vary in number of activated sites in the same zone of the thin filament. I suggest that this is the main reason which leads to a difference in the force developed by the filament pair (see Section 4.2, Fig. 4.4).

For a 70 site long thin filament with activation probability 0.5, the standard deviation of activated sites can be calculated ($2\sqrt{17.5} = 8.4$ nm).

In the next two sections, some properties of the resulting dynamics for different realizations of the activation sequences at different *a priori* probabilities are studied in detail.

k_A (pN/nm)	k_M (pN/nm)	L (nm)	P_{W_1} (nm)	τ_α (ns)	τ_β (ns)	T_{tot} (s)	t_{Ca} (s)
0.1	0.5	14.3	12	30	10	5	0.5

Table 4.1: Parameters used to integrate the filament model under conditions of partial constant activation with different values of activation probability.

4.2.2 Constant activation with different activation probability

A filament pair is studied under conditions of constant partial activation at different activation probabilities. For a fixed value of activation probability, a set of ten realizations of the activation sequence is considered. In particular, the systems is integrated with partial activation of 0.1, 0.2, 0.3, 0.4, ... 0.8 and 0.9 . Each experiment with fixed activation probability is integrated in a time interval of 5 s, the activation sequence is updated every 0.5 s. As in the previous section, the actin filament is taken much longer than the myosin filament. In this way, it is guaranteed that the thick filament overlaps entirely with the thin filament during the dynamics. The model parameters are listed in Table 4.1.

The set of experiments is repeated for two different filament pairs with different

## Histogram of the position of F-actin, sum of ten experiments ($N_M = 60$)
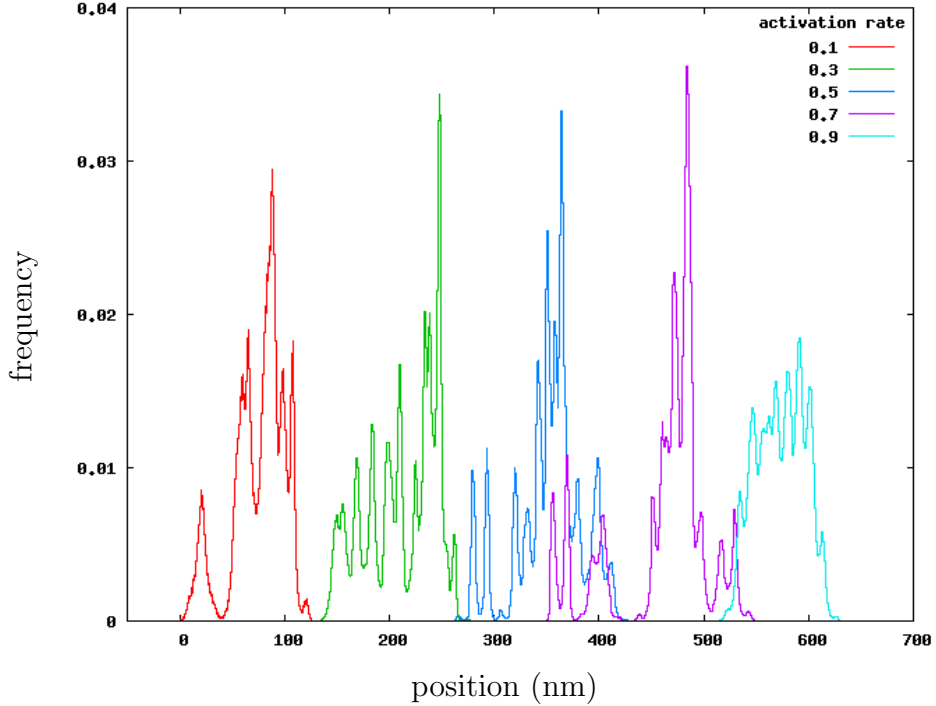
Figure 4.7: Histogram of the dynamics comprising 10 different realizations for the activation sequence in the case of activation rate (*a priori* probability) 0.1, 0.3, 0.5, 0.7 and 0.9. The thick filament is composed of 60 myosin head domains.

number of myosin heads (N_M) for thick filament: $N_M = 10$ and $N_M = 60$. The histograms produced by the entire dynamics (with duration 5 s) comprising the ten segments with different activation sequences, shows multiple peaks as in the case of a single dynamics (see Fig. 4.7 and Fig. 4.8).

The peaks are at nearly constant distances (~ 14 nm) in both cases (N_M). The variance of displacement produced by $N_M = 60$ is larger than that produced by $N_M = 10$, hence the number of local maxima observed in the histogram is bigger in the former case.

The mean displacement is proportional to the external force on the filament and therefore to the force developed by the thick filament. Hence the mean force developed by the myosin filament is computed by the displacement of the actin

Figure 4.8: The histogram of F-actin position is shown for three different activation rates: 0.1, 0.5 and 0.9 . During each dynamics the activation sequence is updated every 0.5 s, i.e. 10 different realizations are employed. The thick filament is composed of 10 myosin head domains.

filament times the stiffness ($k_A y$).

A theoretic estimation of the force produced by the myosin heads can be obtained. In Section 3.3.3, it was shown that the average force developed by a single myosin head depends linearly on the density of activated docking sites on the thin filament and on the number of myosin heads on the thick filament. The estimation is computed multiplying the number of myosin head per mean force developed by a single myosin head under tetanus conditions times the mean activation; the mean activation corresponds to the reduction of the docking site density in average.

The average of mean displacement over the ten different realizations of activation sequences is computed and the developed force is calculated. The numerical estimate is compared with the expected value of mean tension (see Fig. 4.9). In

Average mean displacement of the F-actin
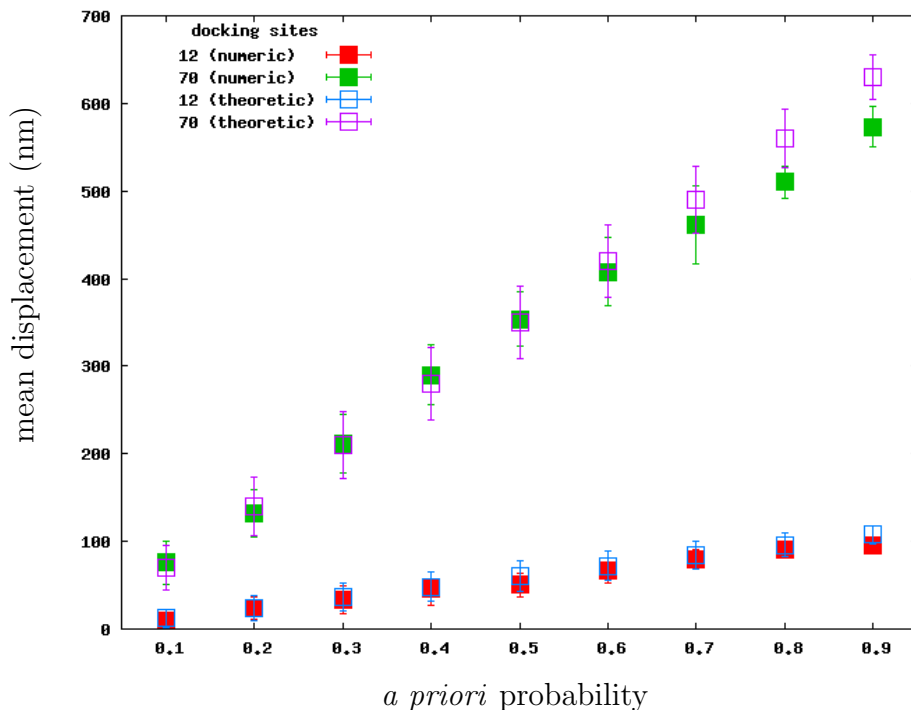
Figure 4.9: The average of mean displacement is calculated over ten different realizations of the activation sequence. The computation was repeated for different activation probabilities and for different number of heads, $N_M = 10, 60$. The numerical results (full marks) are compared to the result of the theoretic estimation (empty marks).

the case of 10 myosin heads, the mean displacement is a linear function of activation probability. This is in good agreement with the theoretic estimations (see Fig. 4.9). For 60 myosin heads the behavior is linear at low activation probabilities (up to 0.7), for high activation probabilities a decrease in efficiency is observed.

The average mean tension along the thick filament is shown in Fig. 4.10; it is a linear function of the position on the filament. The slope decreases with decreasing activation probability. The values of tension were computed by averaging over the ten dynamics realized with different activation sequences.
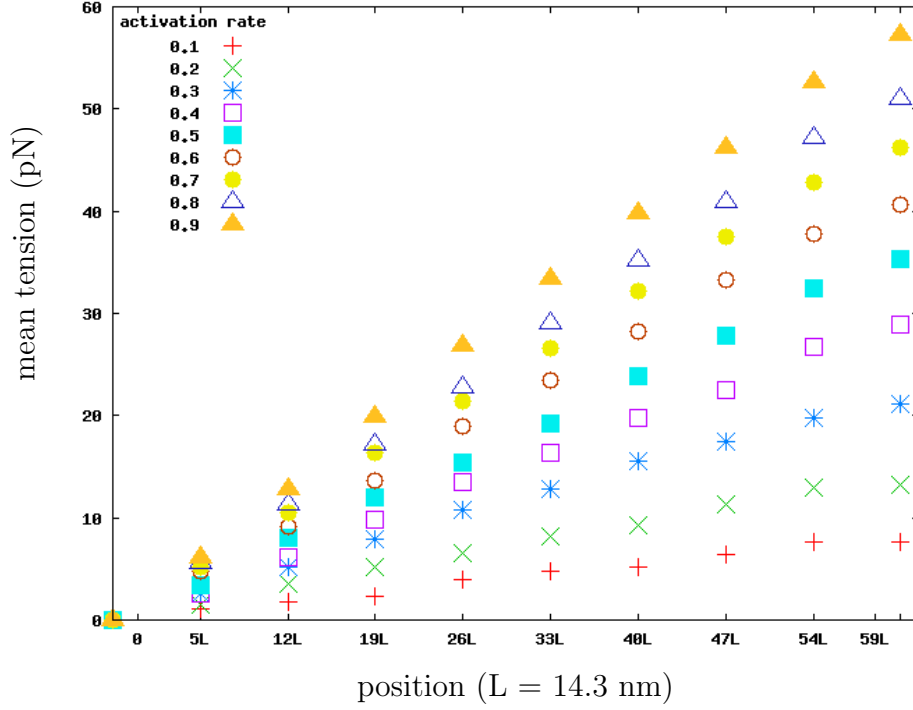
Figure 4.10: The average mean tension was calculated over ten experiments under the same conditions with different activation sequence. This calculation was repeated for different values of the activation probability (see key in figure). The average mean tension increases linearly along the thick filament. The results in the figure are obtained for $N_M = 60$.

4.3 The half–sarcomere setup

The sarcomere is a cylinder delimited by the Z-disks on both extremes; it is symmetric with respect to its section in the middle of the two Z-disks, the M-line (see Section 1.1). Inside the sarcomere thin and thick filaments are structured in arrays; the array of thick filaments is situated central and the filaments are connected to each other at the M-line. The thin filaments are placed on both sides of the thick array, they are linked directly to the Z-disks. The sliding of thin and thick filaments generates shortening of the sarcomere, this is the mechanism at the origin of muscle contraction. In the model I set forth, titin is not considered.

The half-sarcomere belongs from the middle line to the Z-disk and therefore

Schematic representation of the half–sarcomere setup
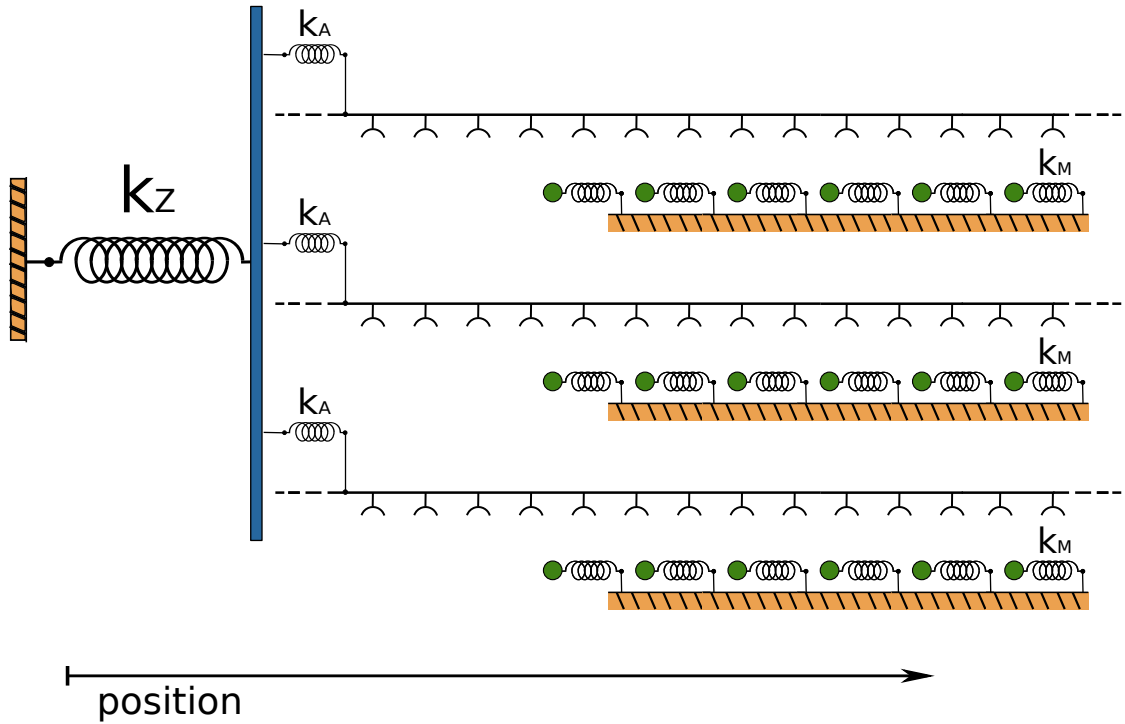
Figure 4.11: The myosin heads are represented by the green circles, they are harmonically linked to a rigid backbone which is thought to be fixed at the M-line, i.e. the rigid backbone is fixed in space. The position of a myosin head is given by $x_{i,k}$, where $i = 1, .. N_M$ numbers the myosin heads on a single filament, while $k = 1, ..., N_F$ numbers the filaments. The thin filament is described by a rigid rod, whose position is given by y_k. The docking sites are located on the thin filament, they are described by the interaction potential; each thin filament is characterized by its interaction potential energy $\widetilde{W}_1, k$. In the case of partial interaction an activation sequence has to be extracted for each filament. The thin filament is such as long that it can be considered unbounded. The filaments are linked harmonically to the Z-disk represented by the blue line. Further, the Z-disk has a harmonic bond to a fixed point, its position is determined by z.

involves a single array of thin and half of the thick filament array. In a recent work, Telley et al. [46] observed the independence of the dynamics of the two halves of the sarcomere. This leads them to propose the half sarcomere as the functional unit of muscle. In this section, the filament model is scaled up to up to the half sarcomere scale.

The half-sarcomere is modeled as an array of filament pairs. the single filament pair depends on the others via its boundary conditions: the half–sarcomere belongs from the Z-disk to the M-line, the actin filaments are bound to the Z-disk, while the myosin filaments are linked together on the M-line. I consider the thin filaments linked harmonically to the Z-disk and the thick filaments fixed rigidly in correspondence to the M-line.

Let N_F be the total number of filament pairs in the sarcomere, then each pair is identified by $k = 1, ..., N_F$. Further, each thick filament has N_M numbers of active domains, identified by $i = 1, ..., N_M$. The equation of motion for the k-th filament pair is given by:

$$\gamma_M \, \dot{x}_{i,k} = k_M \left(x_{i,k} - x_i^{eq} \right) - \widetilde{W}'_{s,k} (x_{i,k} - y_k) + \eta_{i,k}, \tag{4.3}$$

$$\gamma_A \, \dot{y}_k = -k_A \left(y_k - z \right) + \sum_{i=0}^{N_M} \widetilde{W}'_{s,k} (x_{i,k} - y_k) + \eta_k, \tag{4.4}$$

where $x_{i,k}$ is the i-th myosin domain in the k-th filament; the equilibrium positions are assumed to be the same for all the filaments. The interaction potential $\widetilde{W}'_{s,k}$ varies with k because the activation sequence of each thin filament is independent from the others; k_A is the stiffness of the bond linking actin to the Z-disk, y_k is the actin position of the k-th filament and z is the position of the Z-disk. This additional degree of freedom determines the boundary condition common to all thin filaments. The equation of motion of the Z-disk position z is given by:

$$\gamma_Z \dot{z} = -k_Z \left(z - z_{eq} \right) + \sum_{k=0}^{N_F} k_A \left(y_k - z \right), \tag{4.5}$$

where γ_Z is the friction coefficient of the Z-disk, k_Z is the stiffness of an elastic bond to an external fixed point and z_{eq} is the respective equilibrium position. The inertia of the Z-disk is neglected.

k_BT (pNnm)	γ_M (pg/μs)	γ_A (pg/μs)	γ_Z (pg/μs)
4.0	0.1	0.1	1.0

Table 4.2: Parameters characterizing the thermic bath and the Stokes' friction coefficient of myosin and actin used to integrate the sarcomere.

4.4 The half–sarcomere under conditions of constant activation

The half–sarcomere system is studied directly with the interaction potential modulated by activation $\widetilde{W}_1$ (see Section 4.1). The tetanus is a particular case of constant activation with activation probability $p = 1$. The variation of the half–sarcomere length is given by the displacement of the Z-disk (z). The program developed to integrate the dynamics of the myosin heads does not allow for the computation of the dynamics for a system of half–sarcomere with *realistic* dimensions. A half–sarcomere has about 1000 filaments of each type (actin and myosin) and each thick filament has about 60 myosin double head domains (see Section 1.1). To ensure the model behavior it may not be necessary to reach these numbers, but it should be taken into account a number of filaments of the order of several hundreds with 30 to 60 myosin head each thick filament. To integrate systems of this size a parallelization of the computing program is necessary.

The numerical integrations are realized for a decimated half–sarcomere system of 15 filament pairs each having 14 myosin heads on the thick filament. To integrate this system 210 myosin head equations have to be solved. This computation was realized with a serial code.

The model dynamics was integrated for different values of activation and different values of the stiffness k_A characterizing the link between the filaments and the Z–disk respectively. First, I compare the behavior of the Z–disk to the linked filaments at different values of activation and fixed k_A. Then, the response of the Z–disk is examined for different k_A at different activation rates.

4.4.1 Z–disk vs filament

In Figures 4.12, Fig. 4.13 and Fig. 4.14 the histogram of the Z–disk position is compared to the histograms of the F-actin position. Three different dynamics of F-actin linked to the Z–disk are chosen as examples. The different figures correspond to dynamics computed at different activation probabilities.

In general, F–actin and the Z–disk histograms show a multi–peak behavior similar to what was observed for the partially activated filament (see Section 4.2.2, Fig. 4.7 and Fig. 4.8). It was shown that the multi–peak behavior is related to the two lengths L and P_{W_1}. The distance between adjacent docking sites is modified by activation, hence I expect the multi–peak behavior to change with activation.

Position histograms of Z-disk and three actin filaments
(activation probability = 0.1)
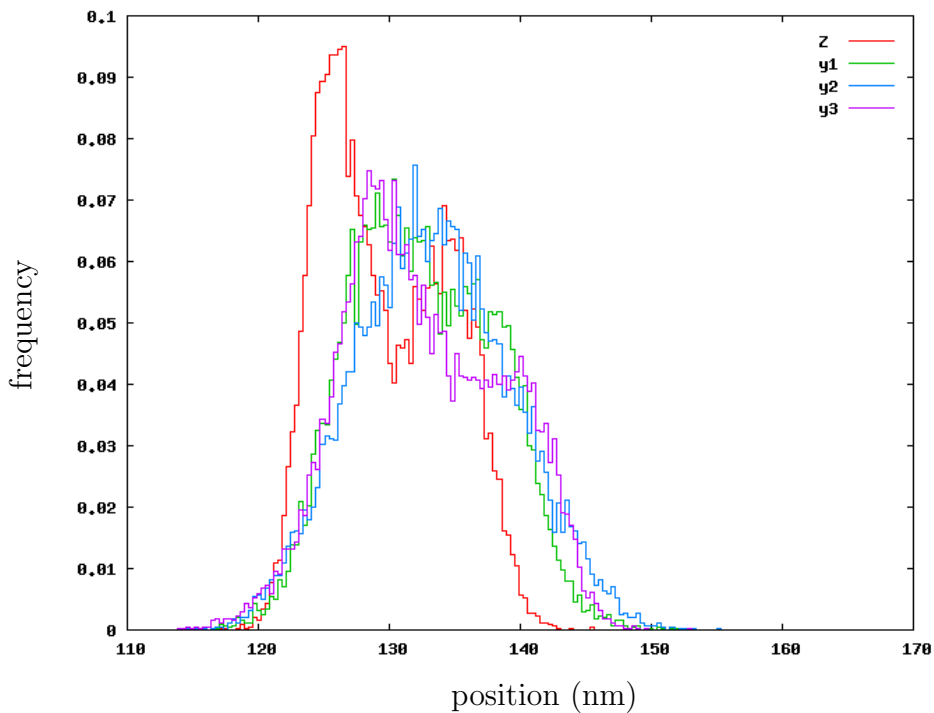
Figure 4.12: The histogram of z is compared with the histograms of three different filaments y_1, y_2, y_3 in the case of activation probability = 0.1.

The value of the stiffness characterizing the link between the Z–disk and the actin filaments is set $k_A = 0.5$ pN/nm. In Fig. 4.13, where the activation proba-

Position histograms of Z-disk and three actin filaments
(activation probability = 0.5)
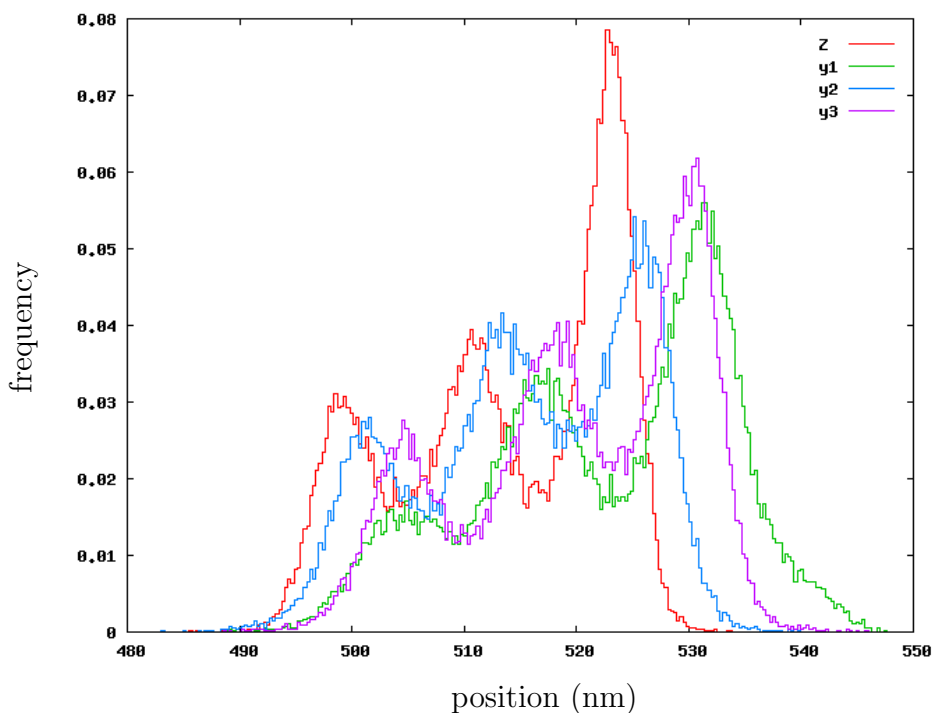
Figure 4.13: The histogram of z is compared with the histograms of three different filaments in the case of activation probability = 0.5.

bility is equal to 0.5, the histograms of the Z–disk and the actin filaments show the same qualitative shape of three local maxima. In the other two cases, for activation probability equal to 0.1 and 0.9, the shape of the histograms representing the F–actin position are qualitatively different for the three filaments. For 0.1 activation probability (see Fig. 4.12), the resulting Z–histogram has two local maxima, while for activation probability = 0.9 (see Fig. 4.14), the histogram of the Z–disk position has a single peak.

In conclusion, in the former case filaments behave similar and the same behavior is therefore found for the Z–disk, while when the filaments behave qualitatively different, the resulting dynamics of the Z–disk is not predictable as a consequence of the general filament behavior.

Position histograms of Z-disk and three actin filaments
(activation probability = 0.9)
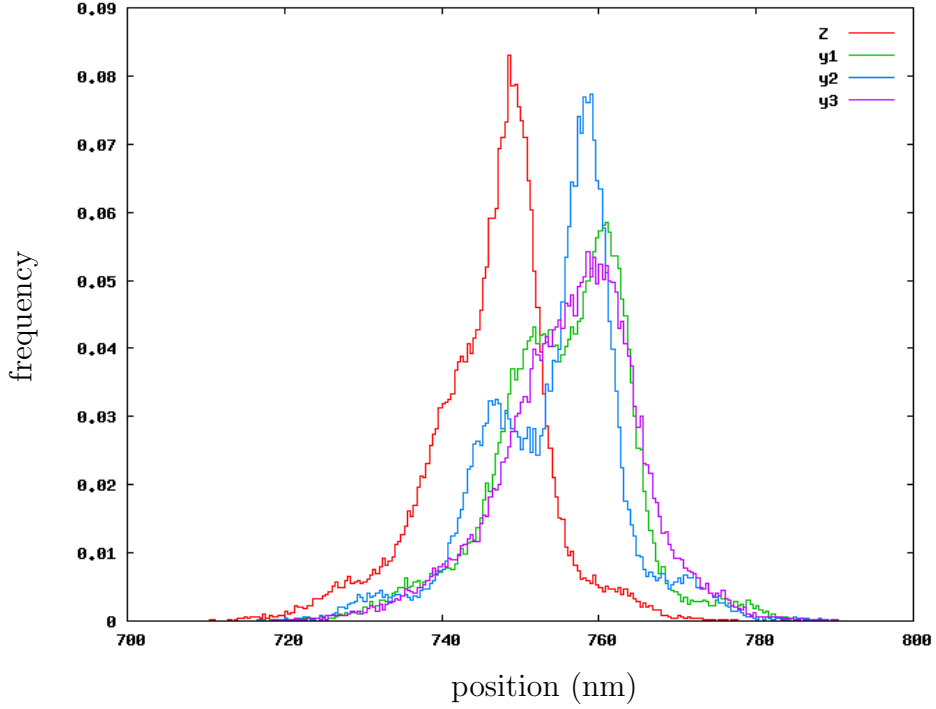
Figure 4.14: The histogram of z is compared with the histograms of three different filaments in the case of activation probability = 0.9. The multiple peaks of the F-actin histograms generate an asymmetric shape of the Z histogram. The Z histogram does not have multiple peaks.

4.4.2 Z–disk dynamics for different stiffness k_A

When comparing the dynamics for sarcomeres with different stiffness k_A of the bond between the F-actin and the Z-disk, it is observed that for $k_A = 0.1$ pN/nm, i.e. for $k_A/k_M \ll 1$, no multiple peak is observed (see Fig. 4.15, Fig. 4.16 and Fig. 4.17).

For $k_A = 0.5$ pN/nm ($k_A/k_M = 1$) the behavior is not uniform for different activation probabilities. Various local maxima are found in the histogram for low activation (activation probability 0.1 and 0.5; see Fig. 4.15 and Fig. 4.16), it was discussed before in the previous section that these behavior has different origin at the filament level. The peaks are of comparable size, i.e. the probability to

Histogram of Z-disk position for different values of k_A
(activation probability $= 0.1$)
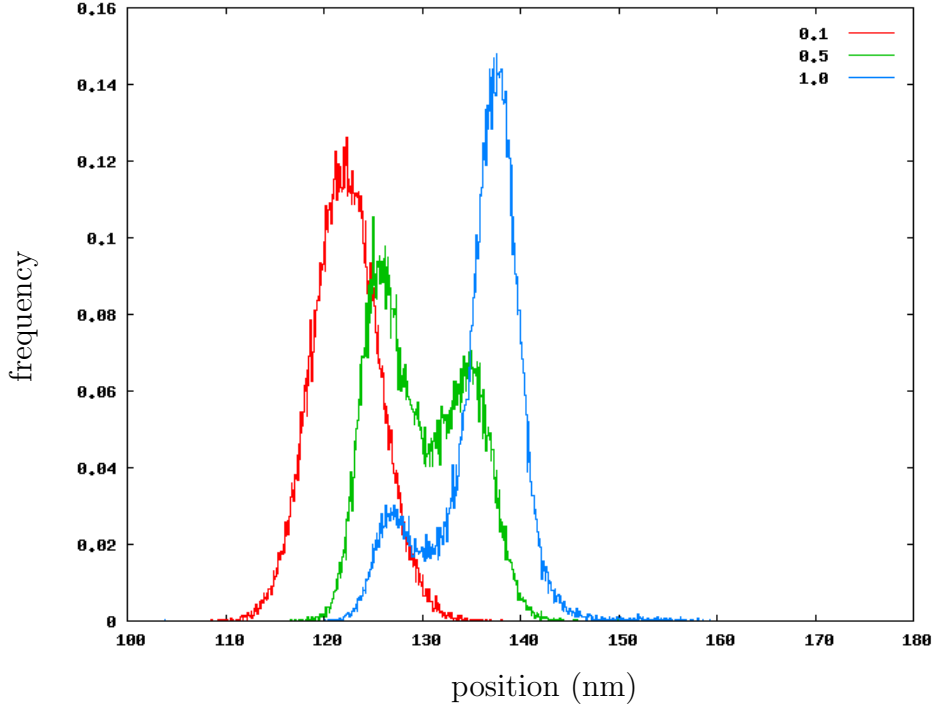
Figure 4.15: The histogram of different sarcomere dynamics are compared. The activation probability is the same in all three cases (0.1), while the value of the stiffness k_A, which characterizes the bond of the F-actin to the Z-disk, differs. From left to right, the plots correspond to the values $k_A = 0.1$ pN/nm, $k_A = 0.5$ pN/nm, $k_A = 1.0$ pN/nm.

find the system in one of its metastable state is the same in order of magnitude. This behavior changes for high activation probability (0.9, see Fig. 4.17). In this case, the histogram of the Z-disk position has a dominant peak, the distribution is asymmetric and has non Gaussian behavior for large variations.

For $k_A = 1.0$ pN/nm ($k_A/k_M \gg 1$) and low activation probability (0.1 and 0.5, see Fig. 4.15 and Fig. 4.16), the histogram of Z-disk position is characterized by a dominant peak, while for activation probability 0.9 a multi–peak shape is observed with envelope in a symmetric distribution function (see Fig. 4.17).

The boundary condition of the filaments characterized by k_A influences qualittively the dynamcis of the Z–disk which differ in fact from the average dynamics

Histogram of Z-disk position for different values of k_A, activation probability 0.5
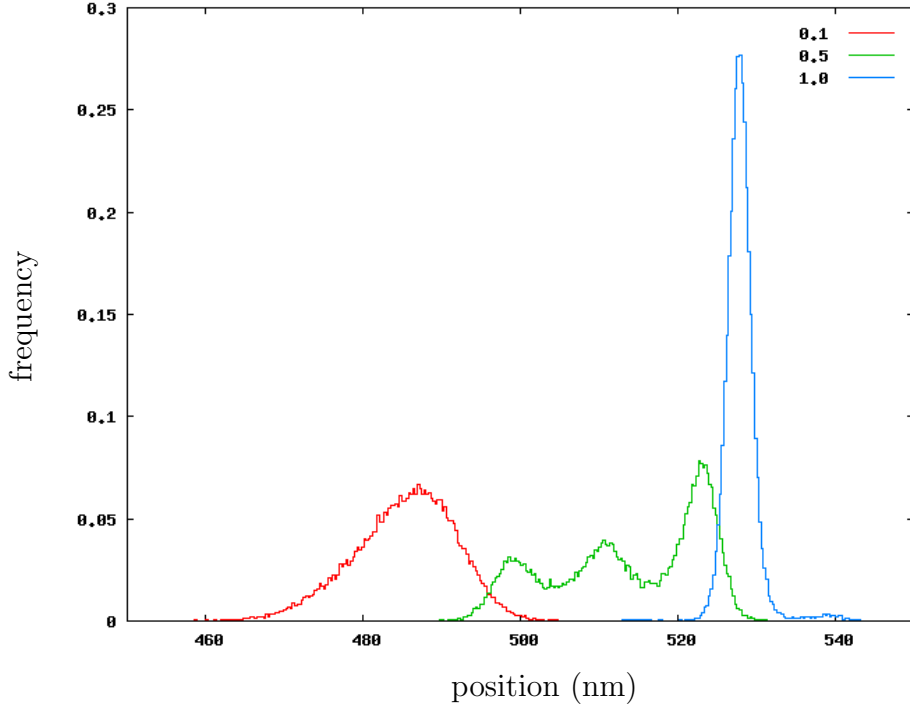
Figure 4.16: The histogram of different sarcomere dynamics are compared. The activation probability is the same in all three cases (0.5), while the value of the stiffness k_A, which characterizes the bond of the F-actin to the Z-disk, differs. From left to right, the plots correspond to the values $k_A = 0.1$ pN/nm, $k_A = 0.5$ pN/nm, $k_A = 1.0$ pN/nm.

of independent filaments: For example, the histogram of the average filament dynamics for $N_M = 10$ and activation probability $= 0.1$, does not show local maxima (see Fig. 4.8), while they were observed in the sarcomere at the same activation probability.

4.4.3 Mean forces as a function of activation probability

In Figure 4.18, the mean displacement of the Z-disk is shown; at each activation probability, 10 different values of the mean displacement are plotted by empty triangles, while the average of the ten experiments with different activation sequence

Histogram of Z-disk position for different values of k_A, activation probability 0.9
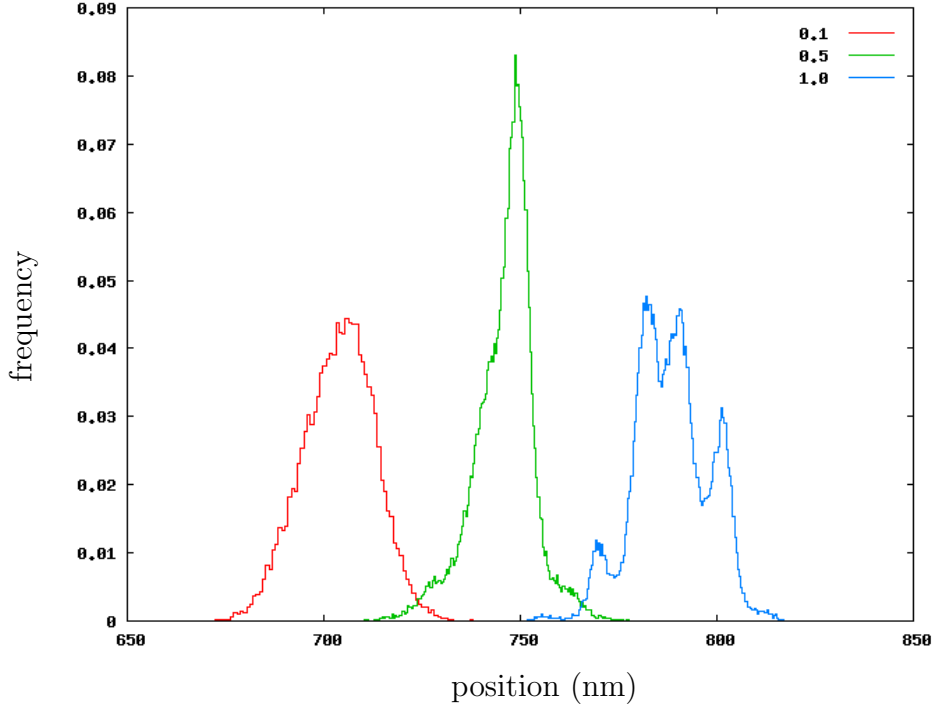

Figure 4.17: The histogram of different sarcomere dynamics are compared. The activation probability is the same in all three cases (0.9), while the value of the stiffness k_A, which characterizes the bond of the F-actin to the Z-disk, differs. From left to right, the plots correspond to the values $k_A = 0.1$ pN/nm, $k_A = 0.5$ pN/nm, $k_A = 1.0$ pN/nm.

is plotted by the full circles. The mean displacement depends linearly on the activation rate up to the activation probability 0.7, and the slope decreases for higher values of the activation probability. The plot in Fig. 4.18 was realized for $k_A = 0.5$ pN/nm; the model parameters are listed in Tab. 4.3. An analogous behavior is found for the different values of k_A (see Fig. 4.19). A qualitative similar behavior was observed also in the case of the filament dynamics (see Section 4.2.2, Fig 4.9).

The amplitude of oscillation in the stationary state of a single experiment is smaller than the variations of mean displacements obtained for different realizations of the activation sequence. The amplitude of oscillation increases with increasing activation, and hence with increasing mean displacement, while the

Mean force as a function of activation
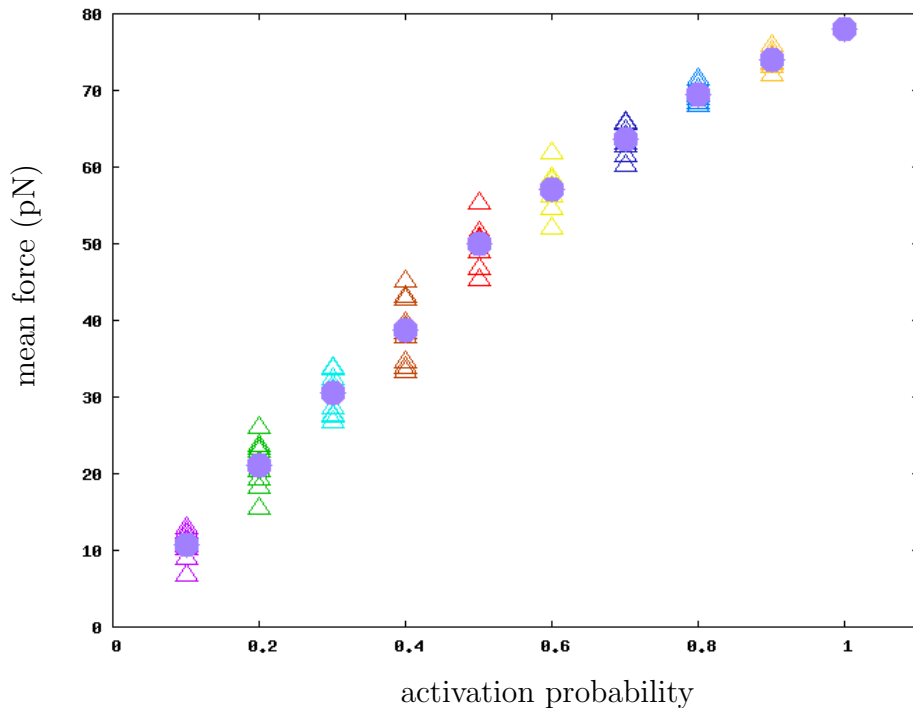
Figure 4.18: The mean force was calculated as a function of the activation probability. The full circles represent the average over 10 different realizations of activation sequences, while the empty triangles at each activation probability represent the 10 different mean values computed for a single realization of activation.

variance of mean displacement for different realizations of activation decreases for very high and very low activation probability (see Fig. 4.18).

The variation due to the stochastic oscillation is expected to increase with the number of motors contributing to the force production; the variation of a sum of independent stochastic increases is given by the sum of variations. In contrast, the latter mentioned variation is related to the variance of the mean activation which has a binomial distribution determined by the activation probability. The binomial distribution has large variance for probability 0.5, while the variance becomes smaller symmetrically for higher an lower probabilities (see Section 4.2.1, Fig. 4.6).

Mean force as a function of activation for different values of k_A
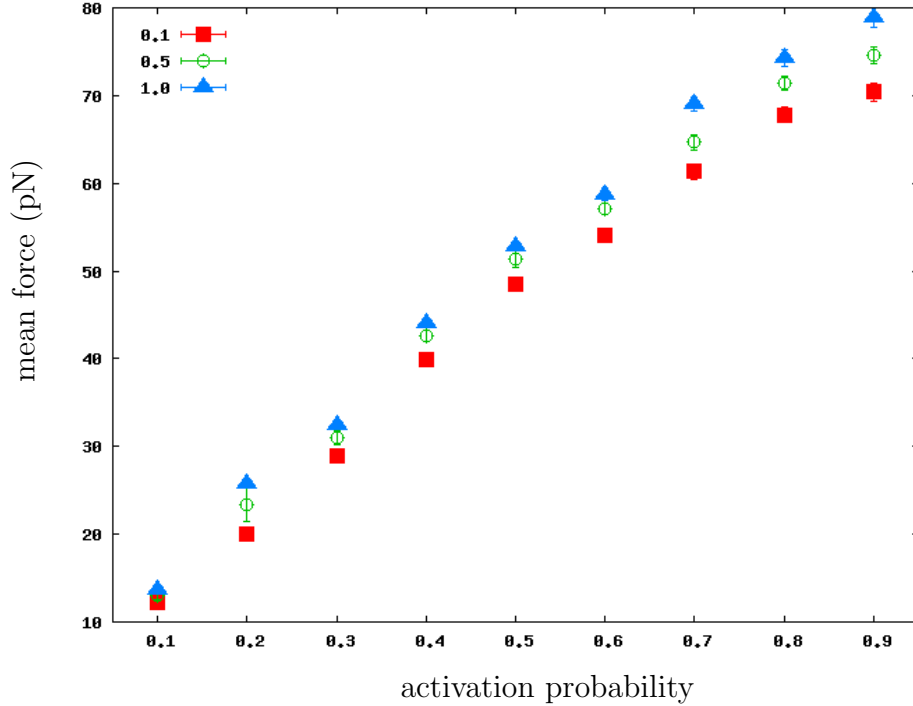
Figure 4.19: The mean force computed from the measure of mean displacment of the Z-disk is plotted for different values of the stiffness $k_A = 0.1, 0.5, 0.9$ pN/nm. The data refer to single experiments with constant fixed activation probability.

4.5   Modeling a single twitch

I simulated a single twitch of activation using linear activation and exponential relaxation (see Fig. 4.20). The behavior of the twitch is inspired by measurements of the concentration of $[Ca^{2+}]$ in a ventricular myocyte in a rabbit [99]. The activation probability in the model is controlled by the functions describing the twitch; in the initial transient until full activation is obtained, the activation probability is given by the linear function of time:

$$\frac{100}{9}\, t, \tag{4.6}$$

where t is the time in seconds. At $t = 0.1$ s the full activation is reached, i.e. activation probability equal to 1 and the activation probability becomes an exponential

k_Z (pN/nm)	k_M (pN/nm)	L (nm)	P_{W_1} (nm)	N_M	N_F	τ_α (ns)	τ_β (ns)	T_{tot} (s)	t_{Ca} (s)
0.1	0.5	14.3	12	14	15	30	10	0.5	0.5

Table 4.3: Parameters of the half–sarcomere collective system under conditions of partial constant activation with different values of activation probability. The dynamics is taken under exam for different values of the stiffness $k_A = 0.1, 0.5, 1.0$ pN/nm.

function of time:

$$\exp\left(\frac{5}{2}(t - 0.095)\right). \tag{4.7}$$

The activation probability is updated every 10 ms and a new activation sequence is extracted with the updated activation probability. The experiment was repeated for two different systems; first the sarcomere with unbounded actin filaments and second the filament with bounded F-actin and 60 myosin heads.

In the first experiment the Z-disk dynamics follows the shape of the stimulation, i.e. it contracts linearly and relaxes exponentially (see Fig. 4.21 red line). The noise is nearly constant during the relaxation dynamics while it is not significant during the linear activation. The model parameters of this experiment are listed in Tab. 4.4 and4.5.

The second experiment is realized for a filament model (see Fig. 4.21 green line). In this setup the actin filament is bounded and the overlap is a function of time. The model parameters of the filament are listed in Tab. 4.6. The dynamics follows also in this case the shape of the stimulation. The noise of the F-actin position has a maximum in the relaxation limb. I suggest that within this zone the overlap region can vary significantly for different realizations of the activation sequence and that this mechanism leads to alterations in the force production.

In this example, the activation sequences are extracted completely independently from each other, i.e. the new state of activation is not influenced by the current one. In the resulting dynamics, the system reaches a stationary state in

Time–varying rate of activation representing a single twitch
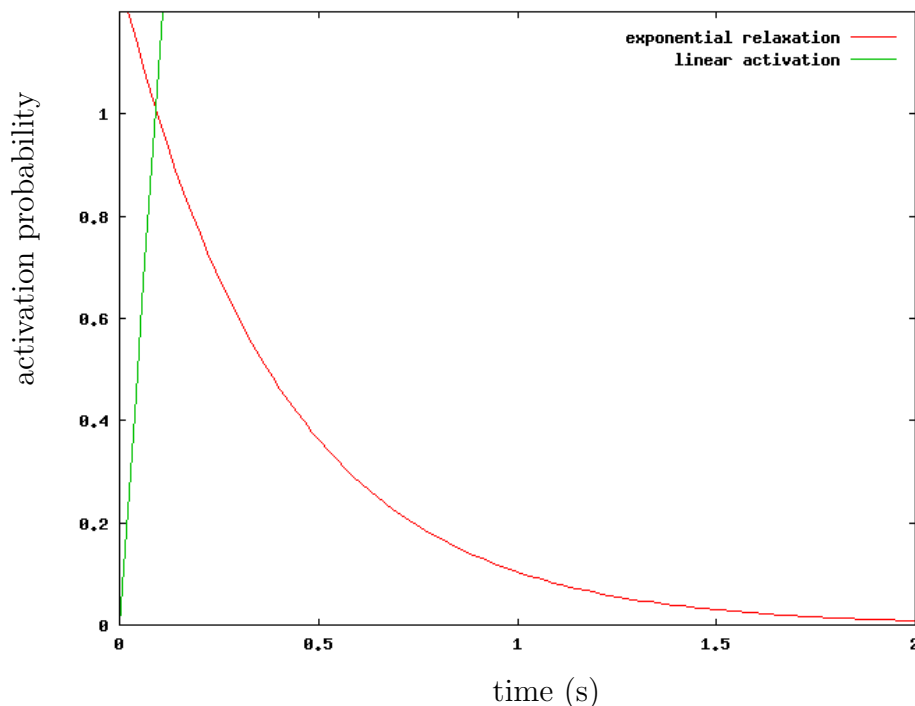
Figure 4.20: Activation profile used to simulate a twitch. The activation rate is linear, while the relaxation decays exponentially. This behavior is inspired by measures of calcium concentration during the activation through a single twitch [99]

each interval of constant activation. This is found to be verified for the filament and the sarcomere dynamics (see Fig. 4.21).

An interesting extension of this study consists in implementing different rules of activation. For example a finite memory (one step) in the extraction of activation sequences can be introduced; the new activation sequence is then extracted under certain constraints imposed by the current activation.

The history dependence of contraction and activation is in fact one open question which is investigated by the experiments on force depression and force enhancement [50–52] (see Section 1.6.2).

Further, an interesting challenge is the response of the system to activation sequences which are correlated along the thin filament. This issue is studied recently by de Tombe et al. [58] and the mechanism underlying the activation and

Response of a filament and a sarcomere to the twitch–stimulation
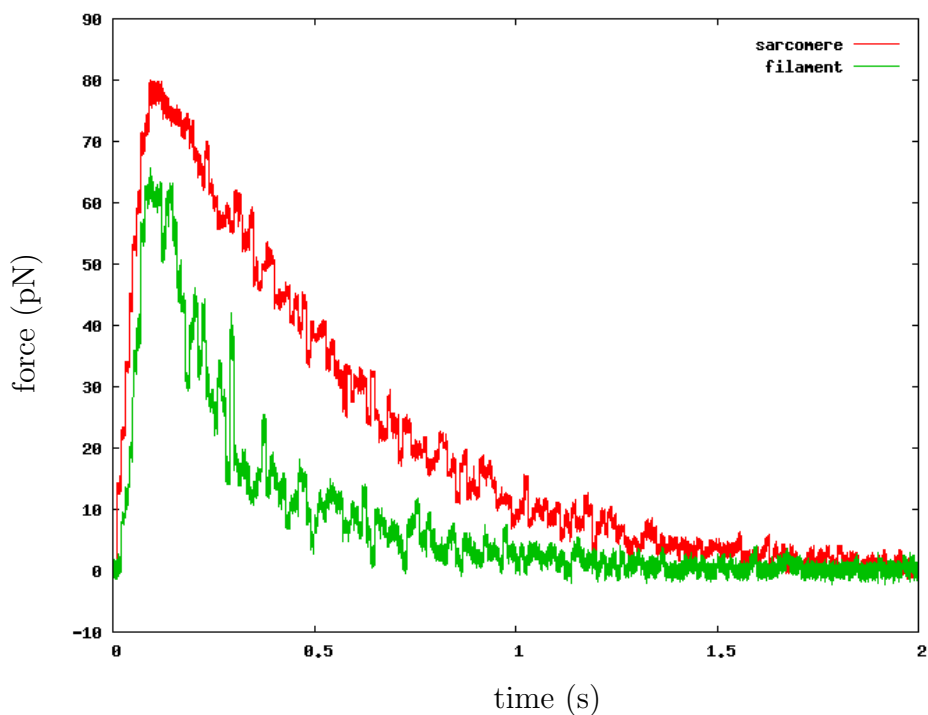
Figure 4.21: The response of a filament is compared to the sarcomere for the activation via a twitch (see Fig. 4.20). for the activation and relaxation induced by the twitch profile shown above (Fig. 4.20). The activation dynamics is identical in the two cases.

contraction measured in the experiments is not yet fully understood.

In conclusion, this simple model can be extended in numerous ways to test hypothesis on the molecular mechanims put forward to explain experimental data.

τ_α (ns)	τ_β (ns)	T_{tot} (s)	t_{Ca} (s)
30	10	2	0.01

Table 4.4: Parameters of transition times, the time of integration and the time determining the updating of the activation sequence and activation probability. These parameters are used to in the computation of the sarcomere system and the filament system.

k_Z (pN/nm)	k_A (pN/nm)	k_M (pN/nm)	L (nm)	P_{W_1} (nm)	N_M	N_F
0.1	0.5	0.5	14.3	12	14	15

Table 4.5: Parameters of the half–sarcomere system integrated for time–varying activation.

k_A (pN/nm)	k_M (pN/nm)	L (nm)	P_{W_1} (nm)	Δoverlap (nm)	N_M
0.1	0.5	14.3	12	250	60

Table 4.6: Parameters of the filament integrated for time–varying activation. $\Delta overlap$ is the overlap of the thin and thick filament at equilibrium position of actin. The thick filament is thought to start at the equilibrium position of the first myosin head on the left (see Fig. 3.19).

Conclusion

Modelling muscle tissue is a multidisciplinary challenge. In this thesis, I have developed a computational method suited to simulate and support advanced experimental studies. To this end, I adapted a 1D two-state stochastic model to describe the dynamics of myosin II motors in a sarcomere. Each state evolves according to a Langevin stochastic equation. The transition from one state to the other is modelled using Kramers' idea of first–passage time between two metastable states. Building on knowledge gained from studies in physiology, chemistry, and physics, I have scaled the model up to a half–sarcomere and also introduced a switch-like mechanism to mimic partial and time-varying activation of myosin II motors.

I implemented my model in C–language to compute its evolution in time. The numerical integration of three different setups was realized: i) a single–motor system, ii) a collective system of motors in series representing a pair of actin and myosin filaments, and iii) a collective system of filaments representing a (decimated) half–sarcomere.

System i) has been compared to the pioneering single motor assay (see Section 3.1). In this assay, the actin filament, directly controlled by an optical tweezer, is brought near to a single myosin motor fixed onto a support and the mechanical response to interaction is measured. The numerical results obtained are found to be in good agreement with the experimental data.

System ii) consists of a filament pair (see Section 3.3.1), where the actin filament is linked harmonically to a fixed point. It is found that the mean restraint force on the F-actin depends linearly on the number of myosin heads and on the density of docking sites on the actin filament Moreover, the mean force decreases exponentially for an increasing transition time from the non-interactive to the interactive state. The value of the inverse–transition time, on the contrary, does not

affect significantly the mean force.

To test whether the collective motor system affords an appropriate description of the interaction between actin and myosin filaments, the model dynamics had to be compared with experimental data (see Section 3.4). To this end, I opted for an experimental setup where the actin filament is trapped by an optical tweezer and interacts with a bundle of myosin filaments. This setup preserves the 3D arrangement realized within a sarcomere, where an F-actin can interact with up to three myosin filaments. Also in this case, my numerical results are in good agreement with the experimental data.

After ensuring that my model gives reasonable results under tetanized conditions, partial activation was introduced and results analized for the filament setup and the half–sarcomere setup (see Chapter 4). The partial activation mechanism is studied in the case of complete overlap, when the thick filament is superposed entirely to the thin filament. In this way, the effects of partial activation are studied independently of the change in the number of myosin heads in the overlap region. The mean force, computed as a funtion of the activation level, exhibits the same qualitative behaviour for the filament pair and the half–sarcomere. Finally, I implemented a time-varying stimulus and computed accordingly the response of a filament pair and of a half–sarcomere.

All the numerical results presented in this thesis were obtained with a serial homemade code. The required computer time seriously limits its application: a real–life half–sarcomere contains about ten thousand myosin motors, and a satisfactory model of it would likely require at least a few thousands of myosin heads. To compare, consider that my serial code allows for computation of collective systems comprising at most a few hundreds of myosin heads. This limitation may hopefully be overcome by implementing an efficient parallel version of the code.

Once computer time is abated, it will become possible to simulate the experimental setups of sarcomere assays used for studying the intriguing effects denominated force depression and force enhancement [50–52]. Another promising line of research that would profit from this simulation device could be the one intended to shed light on the details of the activation mechanism as a function of calcium concentration [58]. In this case, different hypothetical activation mechanisms may be implemented in silico, and a careful comparative study of the numerical re-

sults and of the available experimental data may help verifying or falsifying the hypotheses under exam.

Appendix A

Implementation of the computation

A.1   1D two–state model: functions of integration

Scheme of the single–motor model
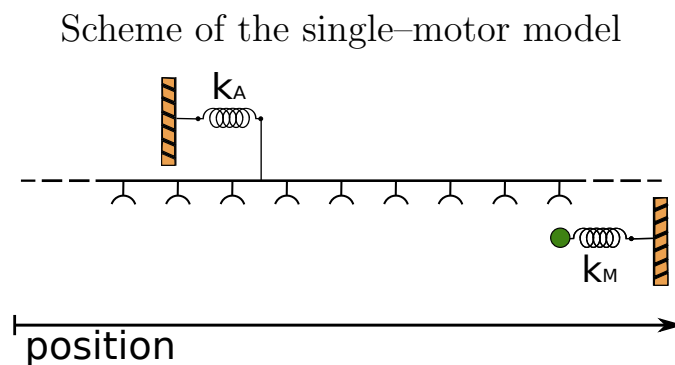
Figure A.1: The myosin head is represented by a bead (in green), it is linked harmonically to a wall with stiffness k_M. The actin filament is represented as an unbounded rigid rod with docking sites at equal distances. The F-actin has an external harmonic bond with stiffness k_A.

The system has two degrees of freedom, the position of the myosin head x_M and the position of the actin filament y_A. Each position evolves according to the Langevin

126

equation (see Section 2.5 Eq. (2.13)):

$$\gamma_M \, \dot{x} = -W_s'(\xi) - k_M(x - x_{eq}) + \eta_M \, ,$$

$$\gamma_A \, \dot{y} = +W_s'(\xi) - k_A \, y + \eta_A \qquad \text{with} \quad \xi = x - y,$$

(A.1)

where x is the position of the myosin head and y the position of the actin filament. γ is the Stokes friction coefficient. The term η represents the gaussian white noise, η is delta-correlated and satisfies the flucutation-dissipation theorem (Eq. (2.4)). The two different states of the model $s = 1, 2$ are characterized by the actin–myosin interaction potential W_s, the shape of the potential energy in each state is shown in Figure A.2.
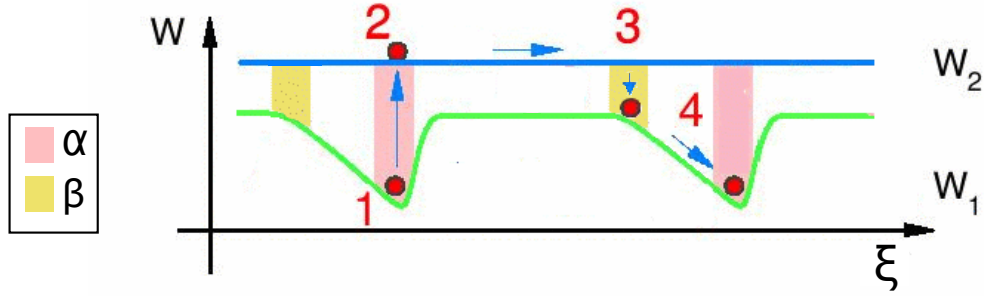
Figure A.2: The two states of the model are distinguished by the interaction potential. The constant potential function W_2 represents the non-interactive state when myosin is in its excited state, while the sawtooth potential W_1 characterizes the actin-myosin interaction in myosin's ground state. The model dynamics for one hydrolysis cycle is traced in 4 steps (adapted from [1]).

The system is described by 2 Langevin equations in each state $s = 1, 2$. Hence, there are four different equations of integration. The integration is of the dynamics is computed with a stochastic Runge–Kutta algorithm for white noise [91]; 4 functions of integration are implemented:

$$\begin{cases} SRK_{M,W_1}(x, y, s = 1) \\ \\ SRK_{M,W_2}(x, y, s = 2), \end{cases} \quad \begin{cases} SRK_{A,W_1}(x, y, s = 1) \\ \\ SRK_{A,W_2}(x, y, s = 2). \end{cases}$$

(A.2)

The two functions labeled M refer to the **S**tochastic **R**unge–**K**utta (SRK) integration function of second order for the myosin head in each state $s = 1, 2$, while the label A indicates the integration functions of the F-actin position.

A.2   Implementation of the chemical transitions

Now, the chemical transition has to be introduced. The system is characterized by two different transition zones α (transition $1 \rightarrow 2$) and β (transition $2 \rightarrow 1$). The interaction potential and the transition zones depends on the relative position $\xi = x - y$. The two variables $\{i, \xi\}$ determine the state and the position on the potential energy function of the system. 4 different cases are distinguished:

$$s = 1, \xi \notin \alpha, \quad s = 1, \xi \in \alpha, \quad s = 2, \xi \notin \beta, \quad s = 2, \xi \in \beta.$$

As mentioned before, the state $s = 1, 2$ determines which integration function has to be chosen, while ξ gives information about the *state of transition*. When ξ is found within one of the transition zones ($\xi \in \alpha, \beta$), the transition dynamics is induced:

Each transition zone is characterized by a transition time t_α and t_β respectively. These times are first initialized at the start of the computation. They are extracted via a Poisson distribution whose mean time is a parameter of the model, τ_α and τ_{beta} respectively. When ξ enters in the transition zone a counter n is initialized to measure the permanence of ξ in the zone. Transition to the other state will occur when the counter equals the extracted transition time, i.e. the value of s will change.

Within this framework, if the system is in one of the transition zones ($\xi \in \alpha, \beta$) an additional parameter, the transition time $t_{\alpha,\beta}$, characterizes the state of the system in relation to the transition dynamics. The two cases to be considered are analogous in the two transition zones:

$$\xi \in \alpha, t_\alpha \leq ndt, \quad \xi \in \alpha, t_\alpha = \text{ndt} \quad (\xi \in \beta, t_\beta \leq ndt, \quad \xi \in \beta, t_\beta = \text{ndt}),$$

where dt is the elementary time–step of integration and ndt is the current time of permanence in the transition zone. In the second case, when $\xi \in \alpha, t_\alpha = $ ndt ($\xi \in \beta, t_\beta = $ ndt) the transition to state 2 (state 1) occurs. Once transition took place, the transition time t_α (t_β) is updated by a new extraction. In conclusion, 6 different cases are distinguished to integrate the system:

$$s = 1, \xi \notin \alpha, \quad s = 1, \xi \in \alpha, t_\alpha \leq \text{ndt}, \quad s = 1, \xi \in \alpha, t_\alpha = \text{ndt},$$

$$s = 2, \xi \notin \beta, \quad s = 2, \xi \in \beta, t_\beta \leq \text{ndt}, \quad s = 2, \xi \in \beta, t_\beta = \text{ndt}.$$

The system can be part of only one of these 6 cases and before integrating the equations of motion the current case has to be evaluated. Consequently, the appropriate integration functions can be chosen (Eq. (A.2)), and the evolution of the dynamical state is determined. The integration can be traced in two fundamental steps, the evaluation and the integration itself.

input	evaluation	integration	output
$x(t)$			$x(t+dt)$
$y(t)$		$\text{SRK}_{M,s}$	$y(t+dt)$
$s(t)$	$\rightarrow \quad \{W_s, \alpha, t_\alpha, \beta, t_\beta\}(\xi, s, n) \quad \rightarrow$	$\rightarrow$	$s(t+dt)$
		$\text{SRK}_{A,s}$	
$n(t)$			$n(t+dt)$

Bibliography

[1] F. Jülicher, A. Ajdari, and J. Prost, "Modeling molecular motors," *Rev. Mod. Phys.*, vol. 69, pp. 1269–1282, Oct 1997.

[2] A. E. Fick, "Mechanische arbeit und wärmeentwicklung," *Leipzig*, 1882.

[3] Heidenhain, "Mechanische leistung wärmeentwicklung und stoffumsatz bei der muskeltaetigkeit.," *Leipzig*, 1864.

[4] A. V. Hill, "The heat of shortening and the dynamic constants of muscle," *Proc. R. Soc. London, Series B, Biological Sciences*, vol. 126, pp. 136–195, October 1938.

[5] W. O. Fenn, "A quantitative comparison between the enegy liberated and the work performed by the isolated sartorius muscle of the frog.," *Journal of Physiology*, vol. 12, pp. 175–203, 1923.

[6] A. F. Huxley, "Muscle structrures and the theories of contraction," *Progr. Biophys. Biophys. Chem.*, vol. 7, pp. 255–318, 1957.

[7] J. T. Finer, R. M. Simmons, and J. A. Spudich, "Single myosin molecule mechanics: piconewton forces and nanometre steps," *Nature*, vol. 368, pp. 113–9, Mar 1994.

[8] J. E. Molloy, J. E. Burns, J. Kendrick-Jones, R. T. Tregear, and D. C. White, "Movement and force produced by a single myosin head," *Nature*, vol. 378, pp. 209–12, Nov 1995.

[9] A. Ishijima, H. Kojima, H. Higuchi, Y. Harada, T. Funatsu, and T. Yanagida, "Multiple- and single-molecule analysis of the actomyosin motor by nanometer-piconewton manipulation with a microneedle: unitary steps and forces," *Biophys J*, vol. 70, pp. 383–400, Jan 1996.

[10] D. Boal, *Mechanics of the Cell*. Cambridge University Press, 2002.

[11] J. Howard, *Mechanics of Motor Proteins and the Cytoskeleton*. Sinauer Associates, 2001.

[12] H. v. Helmholtz, "Über die wärmeentwicklung bei der muskelaction," *Archiv für Anatomie, Physiologie und wissenschaftliche Medicin*, pp. 144–164, 1848.

[13] J. A. Rall, "Sense and nonsense about the Fenn effect," *Am J Physiol Heart Circ Physiol*, vol. 242, no. 1, pp. H1–6, 1982.

[14] Y.-c. Fung, *Biomechanics: mechanical properties of living tissues*. Springer, 2nd ed., 1993.

[15] S. Givli and K. Bhattacharya, "A coarse-grained model of the myofibril: Overall dynamics and the evolution of sarcomere non-uniformities," *Journal of the Mechanics and Physics of Solids*, vol. 57, no. 2, pp. 221 – 243, 2009.

[16] T. Sulman, L. B. Katsnelson, O. Solovyova, and V. S. Markhasin, "Mathematical modeling of mechanically modulated rhythm disturbances in homogeneous and heterogeneous myocardium with attenuated activity of na+ -k+ pump," *Bull Math Biol*, vol. 70, pp. 910–49, Apr 2008.

[17] H. Huxley and J. Hanson, "Changes in the cross-striations of muscles during contraction and stretch and their structural interpretation," *Nature*, vol. 173, pp. 973–976, May 1954.

[18] A. Huxley and R. Niedergerke, "Structural changes in muscle during contraction: Interference microscopy of living muscle fibres," *Nature*, vol. 173, no. 4412, pp. 971–973, 1954.

[19] A. M. Gordon, A. F. Huxley, and F. J. Julian, "The variation in isometric tension with sarcomere length in vertebrate muscle fibres," *J Physiol*, vol. 184, pp. 170–92, May 1966.

[20] F. J. Julian, "Activation in a skeletal muscle contraction model with a modification for insect fibrillar muscle," *Biophys J*, vol. 9, pp. 547–70, Apr 1969.

[21] B. R. Jewell and D. R. Wilkie, "An analysis of the mechanical components in frog's striated muscle," *Journal of Physiology*, vol. 143, pp. 515–540, May 1958.

[22] H. E. Huxley, "The mechanism of muscular contraction," *Science*, vol. 164, pp. 1356–1366, 06 1969.

[23] K. Kitamura, M. Tokunaga, A. H. Iwane, and T. Yanagida, "A single myosin head moves along an actin filament with regular steps of 5.3 nanometres," *Nature*, vol. 397, pp. 129–34, Jan 1999.

[24] A. Periasamy, D. H. Burns, D. N. Holdren, G. H. Pollack, and K. Trombitás, "A-band shortening in single fibers of frog skeletal muscle," *Biophys J*, vol. 57, pp. 815–28, Apr 1990.

[25] J. Hajdu, "Single-molecule x-ray diffraction," *Current Opinion in Structural Biology*, vol. 10, pp. 569–573, 10 2000.

[26] W. Lehman, M. Rosol, L. S. Tobacman, and R. Craig, "Troponin organization on relaxed and activated thin filaments revealed by electron microscopy and three-dimensional reconstruction," *J Mol Biol*, vol. 307, pp. 739–44, Mar 2001.

[27] H. N. Chapman, A. Barty, M. J. Bogan, S. Boutet, M. Frank, S. P. Hau-Riege, S. Marchesini, B. W. Woods, S. Bajt, W. H. Benner, R. A. London, E. Plonjes, M. Kuhlmann, R. Treusch, S. Dusterer, T. Tschentscher, J. R. Schneider, E. Spiller, T. Moller, C. Bostedt, M. Hoener, D. A. Shapiro, K. O. Hodgson, D. van der Spoel, F. Burmeister, M. Bergh, C. Caleman, G. Huldt, M. M. Seibert, F. R. N. C. Maia, R. W. Lee, A. Szoke, N. Timneanu, and J. Hajdu, "Femtosecond diffractive imaging with a soft-x-ray free-electron laser," *Nat Phys*, vol. 2, pp. 839–843, 12 2006.

[28] G. Piazzesi, M. Reconditi, M. Linari, L. Lucii, Y.-B. Sun, T. Narayanan, P. Boesecke, V. Lombardi, and M. Irving, "Mechanism of force generation by myosin heads in skeletal muscle," *Nature*, vol. 415, pp. 659–662, 02 2002.

[29] G. Piazzesi, M. Reconditi, M. Linari, L. Lucii, P. Bianco, E. Brunello, V. Decostre, A. Stewart, D. B. Gore, T. C. Irving, M. Irving, and V. Lombardi, "Skeletal muscle performance determined by modulation of number of myosin motors rather than motor force or stroke size," *Cell*, vol. 131, pp. 784–795, 11 2007.

[30] Y. Goldman and C. Veigel, "Drunk or sober? myosin v walks the (quantum) dotted line in cells.," *Biophysical Journal*, vol. 97, no. 2, pp. 399–400, 2009.

[31] C. Ruff, M. Furch, B. Brenner, D. J. Manstein, and E. Meyhöfer, "Single-molecule tracking of myosin with genetically engineered amplifier domains," *Nature structural biology*, vol. 8, no. 3, pp. 226–229, 2001.

[32] K. Saito, T. Aoki, and T. Yanagida, "Movement of single myosin filaments and myosin step size on an actin filament suspended in solution by a laser trap.," *Biophysical journal*, vol. 66, 03 1994.

[33] S. J. Kron and J. A. Spudich, "Fluorescent actin filaments move on myosin fixed to a glass surface," *Proc Natl Acad Sci U S A*, vol. 83, pp. 6272–6, Sep 1986.

[34] L. S. Tobacman, "Thin filament-mediated regulation of cardiac contraction," *Annu Rev Physiol*, vol. 58, pp. 447–481, 1996.

[35] T. Kobayashi, L. Jin, and P. P. de Tombe, "Cardiac thin filament regulation," *Pflügers Archiv*, vol. 457, pp. 37–46, 2008. 10.1007/s00424-008-0511-8.

[36] N. M. Kad, S. Kim, D. M. Warshaw, P. VanBuren, and J. E. Baker, "Single-myosin crossbridge interactions with actin filaments regulated by troponin-tropomyosin," *Proceedings of the National Academy of Sciences of the United States of America*, vol. 102, no. 47, pp. 16990–16995, 2005.

[37] J. E. Mittenthal and F. D. Carlson, "Transient phases of the isometric tetanus in frog's striated muscle," *J Gen Physiol*, vol. 58, pp. 20–35, Jul 1971.

[38] L. Macpherson and D. R. Wilkie, "The duration of the active state in a muscle twitch," *J Physiol*, vol. 124, pp. 292–9, May 1954.

[39] P. W. Gage and R. S. Eisenberg, "Action potentials, afterpotentials, and excitation-contraction coupling in frog sartorius fibers without transverse tubules," *J Gen Physiol*, vol. 53, pp. 298–310, Mar 1969.

[40] F. J. Julian and R. L. Moss, "Sarcomere length-tension relations of frog skinned muscle fibres at lengths above the optimum," *J Physiol*, vol. 304, pp. 529–39, Jul 1980.

[41] V. J. Schouten, "Interval dependence of force and twitch duration in rat heart explained by ca^{2+} pump inactivation in sarcoplasmic reticulum," *Journal of Physiology*, vol. 431, pp. 427–444, January 1990.

[42] V. Lombardi and G. Piazzesi, "The contractile response during steady lengthening of stimulated frog muscle fibres," *J Physiol*, vol. 431, pp. 141–71, Dec 1990.

[43] E. Homsher, D. M. Lee, C. Morris, D. Pavlov, and L. S. Tobacman, "Regulation of force and unloaded sliding speed in single thin filaments: effects of regulatory proteins and calcium," *J Physiol*, vol. 524 Pt 1, pp. 233–43, Apr 2000.

[44] D. E. Rassier, B. R. MacIntosh, and W. Herzog, "Length dependence of active force production in skeletal muscle," *J Appl Physiol*, vol. 86, pp. 1445–57, May 1999.

[45] Y. Shimamoto, M. Suzuki, and S. Ishiwata, "Length-dependent activation and auto-oscillation in skeletal myofibrils at partial activation by ca2+," *Biochemical and Biophysical Research Communications*, vol. 366, no. 1, pp. 233 – 238, 2008.

[46] I. A. Telley, J. Denoth, E. Stüssi, G. Pfitzer, and R. Stehle, "Half-sarcomere dynamics in myofibrils during activation and relaxation studied by tracking fluorescent markers," *Biophysical Journal*, vol. 90, pp. 514–530, 1 2006.

[47] B. C. Abbott and X. M. Aubert, "The force exerted by active striated muscle during and after change of length," *J Physiol*, vol. 117, pp. 77–86, May 1952.

[48] G. Maréchal and L. Plaghki, "The deficit of the isometric tetanic tension re-developed after a release of frog muscle at a constant velocity," *J Gen Physiol*, vol. 73, pp. 453–67, Apr 1979.

[49] W. Herzog and T. R. Leonard, "Residual force depression is not abolished following a quick shortening step," *Journal of biomechanics*, vol. 40, pp. 2806–2810, 01 2007.

[50] V. Joumaa and W. Herzog, "Force depression in single myofibrils," *J Appl Physiol*, vol. 108, no. 2, pp. 356–362, 2010.

[51] H.-D. Lee and W. Herzog, "Force depression following muscle shortening of voluntarily activated and electrically stimulated human adductor pollicis," *J Physiol*, vol. 551, pp. 993–1003, Sep 2003.

[52] V. Joumaa, T. R. Leonard, and W. Herzog, "Residual force enhancement in myofibrils and sarcomeres," *Proc Biol Sci*, vol. 275, pp. 1411–9, Jun 2008.

[53] D. E. Rassier and W. Herzog, "Considerations on the history dependence of muscle contraction," *J Appl Physiol*, vol. 96, pp. 419–27, Feb 2004.

[54] H. ter Keurs, W. Rijnsburger, R. van Heuningen, and M. Nagelsmit, "Tension development and sarcomere length in rat cardiac trabeculae. evidence of length-dependent activation," *Circulation Research*, vol. 46, pp. 703–714, 1980.

[55] L. Smith, C. Tainter, M. Regnier, and D. A. Martyn, "Cooperative cross-bridge activation of thin filaments contributes to the frank-starling mechanism in cardiac muscle," *Biophys J*, vol. 96, pp. 3692–702, May 2009.

[56] R. E. Godt and D. W. Maughan, "Influence of osmotic compression on calcium activation and tension in skinned muscle fibers of the rabbit," *Pflügers Archiv European Journal of Physiology*, vol. 391, pp. 334–337, 1981. 10.1007/BF00581519.

[57] K. S. McDonald and R. L. Moss, "Osmotic compression of single cardiac myocytes eliminates the reduction in ca2+ sensitivity of tension at short sarcomere length," *Circ Res*, vol. 77, pp. 199–205, Jul 1995.

[58] P. P. de Tombe, R. D. Mateja, K. Tachampa, Y. A. Mou, G. P. Farman, and T. C. Irving, "Myofilament length dependent activation," *Journal of Molecular and Cellular Cardiology*, vol. 48, no. 5, pp. 851 – 858, 2010. Special Issue: Cardiac Sarcomeres and the Integrated Biology of Excitation Contraction Coupling.

[59] J. Konhilas, T. Irving, and P. P. de Tombe, "Frank-starling law of the heart and the cellular mechanisms of length-dependent activation," *Pflügers Archiv European Journal of Physiology*, vol. 445, pp. 305–310, 2002. 10.1007/s00424-002-0902-1.

[60] T. Anazawa, K. Yasuda, and S. Ishiwata, "Spontaneous oscillation of tension and sarcomere length in skeletal myofibrils. microscopic measurement and analysis," *Biophys J*, vol. 61, pp. 1099–108, May 1992.

[61] H. Shimizu, T. Fujita, and S. Ishiwata, "Regulation of tension development by mgadp and pi without ca2+. role in spontaneous tension oscillation of skeletal muscle," *Biophys J*, vol. 61, pp. 1087–98, May 1992.

[62] D. A. Smith and D. G. Stephenson, "The mechanism of spontaneous oscillatory contractions in skeletal muscle," *Biophys J*, vol. 96, pp. 3682–91, May 2009.

[63] A. Fabiato and F. Fabiato, "Myofilament-generated tension oscillations during partial calcium activation and activation dependence of the sarcomere length-tension relation of skinned cardiac cells," *J Gen Physiol*, vol. 72, pp. 667–99, Nov 1978.

[64] S. Leibler and D. A. Huse, "Porters versus rowers: a unified stochastic model of motor proteins," *J Cell Biol*, vol. 121, pp. 1357–68, Jun 1993.

[65] A. Einstein, "Über die von der molekularkinetischen theorie der wärme geforderte bewegung von in ruhenden flüssigkeiten suspendierten teilchen," *Annalen der Physik*, vol. 322, no. 8, pp. 549–560, 1905.

[66] P. Langevin, "Sur la theorie du mouvement brownien," *C. R. Acad. Sci. (Paris)*, vol. 146, pp. 530–533, 1908.

[67] G. Uhlenbeck and L. Ornstein, "On the theory of the brownian motion," *Physical Review*, vol. 36, no. 5, p. 823, 1930.

[68] S. Chandrasekhar, "Stochastic problems in physics and astronomy," *Rev. Mod. Phys.; Reviews of Modern Physics*, vol. 15, no. 1, pp. 1–89, 1943.

[69] T. A. Duke, "Molecular model of muscle contraction," *Proc Natl Acad Sci U S A*, vol. 96, pp. 2770–5, Mar 1999.

[70] A. B. Kolomeisky and M. E. Fisher, "Molecular motors: a theorist's perspective," *Annu Rev Phys Chem*, vol. 58, pp. 675–95, 2007.

[71] R. Cooke, "The sliding filament model: 1972-2004," *J Gen Physiol*, vol. 123, pp. 643–56, Jun 2004.

[72] R. P. Feynman, R. B. Leighton, M. Sands, and R. B. Lindsay, "The feynman lectures on physics, vol. 3: Quantum mechanics," *Physics Today*, vol. 19, no. 11, pp. 80–83, 1966.

[73] M. O. Magnasco, "Forced thermal ratchets," *Phys. Rev. Lett.*, vol. 71, pp. 1477–1481, Sep 1993.

[74] R. D. Astumian and M. Bier, "Fluctuation driven ratchets: Molecular motors," *Phys. Rev. Lett.*, vol. 72, pp. 1766–1769, Mar 1994.

[75] R. D. Astumian, "Thermodynamics and Kinetics of a Brownian Motor," *Science*, vol. 276, no. 5314, pp. 917–922, 1997.

[76] A. Ajdari and J. Prost, "Mouvement induit par un potentiel périodique de basse symétrie : diélectrophorèse pulsée," 1992.

[77] J. W. Sanger and J. M. Sanger, "Fishing out proteins that bind to titin," *The Journal of Cell Biology*, vol. 154, no. 1, pp. 21–24, 2001.

[78] P. Hänggi and F. Marchesoni, "Artificial brownian motors: Controlling transport on the nanoscale," *Rev. Mod. Phys.*, vol. 81, pp. 387–442, Mar 2009.

[79] T. Shimokawa, S. Sato, A. Buonocore, and L. M. Ricciardi, "A chemically driven fluctuating ratchet model for actomyosin interaction," *Biosystems*, vol. 71, no. 1-2, pp. 179 – 187, 2003. Selection of Papers from Topics in Biomathematics and Related Computational Problems at the Beginning of the Third Millennium.

[80] B. Gaveau, "Microscopic model of the actin-myosin interaction in muscular contractions"," *Phys. Rev. E; Physical Review E*, vol. 69, no. 1, 2004.

[81] K. Kruse and F. Jülicher, "Dynamics and mechanics of motor-filament systems," *Eur Phys J E Soft Matter*, vol. 20, pp. 459–65, Aug 2006.

[82] M. Badoual, F. Jülicher, and J. Prost, "Bidirectional cooperative motion of molecular motors," *Proc Natl Acad Sci U S A*, vol. 99, pp. 6696–701, May 2002.

[83] M. Takano, T. P. Terada, and M. Sasai, "Unidirectional brownian motion observed in an in silico single molecule experiment of an actomyosin motor," *Proc Natl Acad Sci U S A*, vol. 107, pp. 7769–74, Apr 2010.

[84] D. Parker, Z. Bryant, and S. L. Delp, "Coarse-grained structural modeling of molecular motors using multibody dynamics," *Cell Mol Bioeng*, vol. 2, pp. 366–374, Sep 2009.

[85] I. Aprodu, M. Soncini, and A. Redaelli, "Mechanical characterization of motor proteins: A molecular dynamics approach," *Macromolecular Theory and Simulations*, vol. 17, no. 7-8, pp. 376–384, 2008.

[86] D. Smith and J. Sleep, "Strain-dependent kinetics of the myosin working stroke, and how they could be probed with optical-trap experiments," *Biophys J*, vol. 91, pp. 3359–69, Nov 2006.

[87] D. A. Smith, M. A. Geeves, J. Sleep, and S. M. Mijailovich, "Towards a unified theory of muscle contraction. i: foundations," *Ann Biomed Eng*, vol. 36, pp. 1624–40, Oct 2008.

[88] D. A. Smith and S. M. Mijailovich, "Toward a unified theory of muscle contraction. ii: predictions with the mean-field approximation," *Ann Biomed Eng*, vol. 36, pp. 1353–71, Aug 2008.

[89] H. A. Kramers, "Brownian motion in a field of force and the diffusion model of chemical reactions," *Physica*, vol. 7, no. 4, pp. 284 – 304, 1940.

[90] P. Hänggi, P. Talkner, and M. Borkovec, "Reaction-rate theory: fifty years after kramers," *Rev. Mod. Phys.*, vol. 62, pp. 251–341, Apr 1990.

[91] R. Honeycutt, "Stochastic runge-kutta algorithms. i. white noise," *Phys Rev A*, vol. 45, pp. 600–603, Jan 1992.

[92] R. Honeycutt, "Stochastic runge-kutta algorithms. ii. colored noise," *Phys Rev A*, vol. 45, pp. 604–610, Jan 1992.

[93] A. Lewalle, W. Steffen, O. Stevenson, Z. Ouyang, and J. Sleep, "Single-molecule measurement of the stiffness of the rigor myosin head," *Biophysical Journal*, vol. 94, no. 6, pp. 2160 – 2169, 2008.

[94] I. Rayment, W. R. Rypniewski, K. Schmidt-Bäse, R. Smith, M. M. Benning, D. A. Winkelmann, G. Wesenberg, and H. M. Holden, "Three-dimensional structure of myosin subfragment-1: a molecular motor.," *Science*, vol. 261, pp. 50–58, July 1993.

[95] J. Sleep, A. Lewalle, and D. Smith, "Reconciling the working strokes of a single head of skeletal muscle myosin estimated from laser-trap experiments and crystal structures," *Proc Natl Acad Sci U S A*, vol. 103, pp. 1278–82, Jan 2006.

[96] H. Tanaka, A. Ishijima, M. Honda, K. Saito, and T. Yanagida, "Orientation dependence of displacements by a single one-headed myosin relative to the actin filament," *Biophysical journal*, vol. 75, pp. 1886–1894, 10 1998.

[97] A. Ishijima and T. Yanagida, "Single molecule nanobioscience," *Trends Biochem Sci*, vol. 26, pp. 438–44, Jul 2001.

[98] M. Suzuki, H. Fujita, and S. Ishiwata, "A new muscle contractile system composed of a thick filament lattice and a single actin filament," *Biophysical Journal*, vol. 89, no. 1, pp. 321 – 328, 2005.

[99] D. M. Bers, "Cardiac excitation-contraction coupling," *Nature*, vol. 415, pp. 198–205, 01 2002.